

UNCLASSIFIED

AD NUMBER

AD906967

LIMITATION CHANGES

TO:

Approved for public release; distribution is unlimited.

FROM:

Distribution authorized to U.S. Gov't. agencies only; Test and Evaluation; 30 NOV 1972. Other requests shall be referred to Air Force Cambridge Research Laboratory, LZP, Hanscom AFB, MA 01730.

AUTHORITY

AFCRL Itr, 16 Sep 1975

THIS PAGE IS UNCLASSIFIED

THIS REPORT HAS BEEN DELIMITED
AND CLEARED FOR PUBLIC RELEASE
UNDER DOD DIRECTIVE 5200.20 AND
NO RESTRICTIONS ARE IMPOSED UPON
ITS USE AND DISCLOSURE.

DISTRIBUTION STATEMENT A

APPROVED FOR PUBLIC RELEASE;
DISTRIBUTION UNLIMITED.

AD906967

INSTRUMENTATION AND FLIGHT RESULTS OF REENTRY PLASMA DIAGNOSTIC AND ALLEVIATION EXPERIMENTS ON TRAILBLAZER II ROCKETS

J. Spencer Rochefort
Raimundas Sukys
Ronald Symmes



NORTHEASTERN UNIVERSITY
Boston, Massachusetts 02115

Contract No. F 19628-69-C-0150

Project No. 4642

Task No. 464201

Work Unit No. 46420101

FINAL REPORT

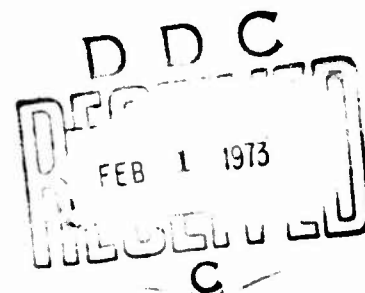
1 March 1965 through 31 August 1972
31 October 1972

Contract Monitor: Joseph L. Poirier
Microwave Physics Laboratory

Distribution limited to U.S. Government agencies only;
Test and Evaluation, 30 November 1972. Other requests for
this document must be referred to AFCRL (LZP), L. G.
Hanscom Field, Bedford, Massachusetts 01730.

Prepared for

AIR FORCE CAMBRIDGE RESEARCH LABORATORIES
AIR FORCE SYSTEMS COMMAND
UNITED STATES AIR FORCE
BEDFORD, MASSACHUSETTS 01730



Qualified requestors may obtain additional copies from
the Defense Documentation Center.

AFCRL-72-0695

INSTRUMENTATION AND FLIGHT RESULTS OF REENTRY PLASMA DIAGNOSTIC
AND ALLEVIATION EXPERIMENTS ON TRAILBLAZER II ROCKETS

J. Spencer Rochefort
Raimundas Sukys
Ronald Symmes

NORTHEASTERN UNIVERSITY
Boston, Massachusetts 02115

Contract No. F19628-69-C-0150
Project No. 4642
Task No. 464201
Work Unit No. 46420101

FINAL REPORT
1 March 1965 through 31 August 1972
31 October 1972

Contract Monitor: Joseph L. Poirier
Microwave Physics Laboratory

Distribution limited to U.S. Government agencies only:
Test and Evaluation, 30 November 1972. Other requests for
this document must be referred to AFCRL (LZP), L. G.
Hanscom Field, Bedford, Massachusetts 01730.

Prepared for

AIR FORCE CAMBRIDGE RESEARCH LABORATORIES
AIR FORCE SYSTEMS COMMAND
UNITED STATES AIR FORCE
BEDFORD, MASSACHUSETTS 01730

ABSTRACT

Two Trailblazer II rockets were launched on 24 November 1970 and 28 July 1972 from NASA rocket test facility at Wallops Island, Virginia, to study the properties of the shock-ionized flow field and its effects on microwave radiation. Description of the apparatus carried by the two vehicles is presented in this report. The instrumentation to measure the flow field during reentry included such diagnostic sensors as electrostatic probes, strip-line probe and a conductivity probe. S-band microwave systems were employed to determine plasma effects on antennas. The measurements included phase and magnitude of the reflection coefficient, variations in mutual coupling between two on board antennas and transmitted signal attenuation. A pulsed liquid injection apparatus was used to perform a plasma alleviation experiment. Performance of the instrumentation and general results obtained from unprocessed data are discussed.

TABLE OF CONTENTS

	Page No.
TITLE PAGE.....	i
ABSTRACT.....	iii
TABLE OF CONTENTS.....	v
LIST OF ILLUSTRATIONS.....	vi
LIST OF TABLES.....	viii
INTRODUCTION.....	1
CHAPTER I. TRAILBLAZER II INSTRUMENTATION.....	2
A. Vehicle and Nose Cone.....	2
B. AD21.862 Payload.....	3
C. A21.011-1 Payload.....	4
CHAPTER II. S-BAND MEASUREMENTS.....	6
A. Reflectometer.....	6
B. Multiprobe Fieldmeter.....	7
C. Mutual Coupling.....	10
CHAPTER III. PROBES.....	12
A. Fixed Bias Electrostatic Probes.....	12
B. Variable Bias Electrostatic Probes.....	13
C. Stripline Probe.....	16
CHAPTER IV. INJECTION SYSTEM.....	18
CHAPTER V. TELEMETRY SYSTEM.....	23
CHAPTER VI. PERFORMANCE AND DATA.....	25
A. AD21.862.....	25
B. A21.011-1.....	28
ACKNOWLEDGEMENTS.....	30
BIBLIOGRAPHY.....	31
PERSONNEL.....	34
RELATED CONTRACTS AND PUBLICATIONS.....	34

LIST OF ILLUSTRATIONS

	Page No.
Fig. 1 Trailblazer II Rocket	40
Fig. 2 Trajectory and Staging	41
Fig. 3 Reentry Velocity	41
Fig. 4 Nose Cone A21.011-1	42
Fig. 5 Nose Cone Configuration	42
Fig. 6 Forward Section of A21.011-1 Payload	43
Fig. 7 Tapered Boxes	43
Fig. 8 Test Antenna	44
Fig. 9 Block Diagram of AD21.862 Instrumentation	45
Fig. 10 Block Diagram of A21.011-1 Instrumentation	46
Fig. 11 S-Band Experiment Block Diagram	47
Fig. 12 Error in Measured Reflection Coefficient	47
Fig. 13 Four Probe Field Meter	48
Fig. 14 Probe Signal Amplifier	48
Fig. 15 Error in Measured Phase Angle	49
Fig. 16 Error in Measured Magnitude of Reflection Coefficient	49
Fig. 17 Coupled Signal Amplifier	50
Fig. 18 Flushmounted Electrostatic Probe Configuration	50
Fig. 19 Dual Electrostatic Probe Electronics	51
Fig. 20 Fixed Bias Electrostatic Probe	51
Fig. 21 Log Amplifier	52
Fig. 22 Typical Log Amplifier Characteristic	52
Fig. 23 Variable Bias Electrostatic Probe	53
Fig. 24 Steady State Restoration Circuit	54
Fig. 25 Switchable Positive Voltage Regulator	54
Fig. 26 Switchable Negative Voltage Regulator	55
Fig. 27 Common Mode Rejection Circuit	56

Fig. 28	Logic Clock	56
Fig. 29	Simulated Commutator Diagram	57
Fig. 30	Simulated Commutator Waveforms	58
Fig. 31	Stripline Probe	59
Fig. 32	Stripline Block Diagram	60
Fig. 33	Stripline Signal Amplifier	60
Fig. 34	Chemical Injection Deck	61
Fig. 35	Injection Control General Diagram	62
Fig. 36	Valve Control Circuit	63
Fig. 37	Monitor and Fault Detector	63
Fig. 38	Timing and S1 Control Circuit	64
Fig. 39	Explosive Valve Trigger Circuit	64
Fig. 40	Telemetry Antenna Patterns	65
Fig. 41	TM Reflectometer Data. AD21.862	66
Fig. 42	Test Signal Data. AD21.862	67
Fig. 43	Stripline Data	68
Fig. 44	Electrostatic Probe Data S/R = 0. AD21.862	69
Fig. 45	Electrostatic Probe Data S/R = 2.58, $\theta = 57.0^\circ$. AD21.862	69
Fig. 46	Electrostatic Probe Data S/R = 2.58, $\theta = 48.0^\circ$. AD21.862	70
Fig. 47	Electrostatic Probe Data S/R = .475, $\theta = 52.5^\circ$. AD21.862	70
Fig. 48	Injection Pressure and Piston Motion	71
Fig. 49	Test and TM Signal Data. A21.011-1	72
Fig. 50	Four Probe Field Meter Data	73
Fig. 51	Electrostatic Probes - Fixed Bias Data. A21.011-1	74
Fig. 52	Electrostatic Probe Data S/R = 2.4, $\theta = 48.0^\circ$. A21.011-1	75
Fig. 53	Electrostatic Probe Data S/R = 2.4, $\theta = 57.0^\circ$. A21.011-1	76

LIST OF TABLES

	Page No.
Table I Antenna and Probe Locations AD21.862	35
Table II Antenna and Probe Locations A21.011-1	36
Table III Telemetry Channel Assignment AD21.862	37
Table IV Telemetry Channel Assignment A21.011-1	38
Table V Reentry Parameters	39

INTRODUCTION

During hypervelocity flight through the earth's atmosphere any aerospace vehicle is enveloped by a shock-ionized flow field. This so called plasma sheath plays an important role in determining the quality of communications between the vehicle and a ground station.¹⁻⁷ Typically a complete blackout of communications occurs when the electron concentration in the plasma sheath near an antenna reaches or exceeds a certain critical number which is proportional to the square of the radio frequency used. Based on this criterion two obvious means may be employed to penetrate the plasma sheath around the vehicle. One possible way is to operate the communication link at frequencies which exceed the plasma frequency. The other possibility is to lower the plasma electron concentration through various plasma modification techniques. Before these or any other possible plasma alleviation techniques can be successfully applied an accurate definition of the expected plasma electron concentrations and their effects on the vehicle antennas must be known.

For this reason a series of experiments were instrumented and flown on Trailblazer II reentry vehicles. The objectives of the experiments were to perform direct measurements of the electron concentration in the plasma, to determine its effects upon the operation of the antennas, to compare the existing flow field models with actual flight results, and to test new plasma diagnostic devices and alleviation techniques. This report describes the instrumentation of two Trailblazer II rockets AD21.862 and A21.011-1 launched from NASA Wallops Island rocket test facility on 24 November 1970 and 28 July 1972 respectively.

The instrumentations included S-band systems to measure the reflection coefficients of antennas, to determine the phase of the reflected waves and to measure the mutual coupling between two on board antennas. Flush mounted electrostatic probes with fixed and variable bias voltages measured the electron density at various positions along the nose cone. Other diagnostic devices flown included a stripline probe, a conductivity probe and a liquid injection system to perform a plasma alleviation experiment. Both flights were equipped with PAM/FM/FM S-band telemetry systems.

Numbered superscripts refer to the references in the Bibliography.

CHAPTER 1

TRAILBLAZER II INSTRUMENTATION

A. VEHICLE AND NOSE CONE

The instrumentation was carried aboard a Trailblazer II vehicle similar to that shown in Fig. 1. This vehicle consists of four solid-propellant rockets and is capable of high reentry velocities. The first two stages of the Trailblazer are used to achieve an apogee of about 200 miles. During the ascending phase of the flight the third stage motor and the nose cone which contains not only the instrumentation but also the fourth stage of the rocket are enclosed in a protective structural shell and are facing down. This whole subassembly of the vehicle represents the so called "velocity package". Rexolite windows are provided in the protective shell to allow for a continuous monitoring of the telemetry and the test signals during ascent. The windows are located opposite all five transmitting antennas of the nose cone.

Shortly after lift-off the canted fins of the second stage motor induce a spin to stabilize the vehicle at an approximate angle of 68 degrees for the entire flight. At an altitude of 255,000 ft. the velocity package separates from the burnt-out second stage motor and continues to coast up. After the apogee, when the velocity package begins its descent, the third stage motor ignites and propels the nose cone out of the open end of the protective shell. The final thrust is provided by the fourth stage spherical motor. The nose cone containing the instrumentation and the spent fourth stage motor reenters the earth's atmosphere at a velocity of 17,500 ft. per second, while spinning at 12 revolutions per second. Nominal trajectory, staging and reentry velocity characteristics for a Trailblazer II rocket carrying a 70 pound nose cone are shown in Fig. 's 2 and 3.

The reentry vehicle is a blunt cone consisting of a 6.33 in. radius hemispherical nose cap and a nine degree half angle conical afterbody. The overall length of the nose cone measured along the center line is 26.47 in. and the diameter of the base is 19.17 in. The skin of the vehicle is fabricated entirely of aluminum and no ablative materials are used. Also to minimize the contamination of the plasma by foreign matter, the nose cone is cleaned with alcohol just before it is inserted into the velocity package. A photograph of the AD21.862 reentry vehicle is shown in Fig. 4. Antenna and probe locations for the AD21.862 and the A21.011-1 vehicles are tabulated in Tables I and II respectively. They are expressed as ratios of the

distance S from the nose cap center point, measured along the surface of the vehicle, and the radius R of the nose cap. The angles are referenced to an arbitrary zero at the top dead center (TDC) of the rocket and are measured counter-clockwise looking into the tip of the nose cone. A general layout of the equipment and the fourth stage spherical motor housed within the reentry vehicle is shown in Fig. 5.

Part of the instrumentation was mounted on two plates in the forward section of the vehicle. Other equipment was installed in a number of tapered boxes on the inner surface of the nose cone (Fig.'s 6 and 7). It should be noted that the mechanical design and the required machine work was supplied by AFCRL.

Some of the instruments carried on the two flights were either alike or differed only slightly from each other. Therefore after a brief general outline of the instrumentation used in each flight, a more detailed description, without flight designation, will be given to each instrument.

B. AD21,862 PAYLOAD

Each payload could be considered to consist of two major instrumentation systems. One system included the plasma test and diagnostic apparatus, while the other consisted of the telemetry link, body motion and temperature sensors. Both systems were controlled and operated as completely separate entities with their own power sources. Each power source was a 27 volt, one ampere-hour battery able to supply one system for approximately 30 minutes. External power was used during countdown.

The instrumentation of the AD21,862 rocket included two S-band reflectometers. One measured the reflection coefficient of the test antenna while the other monitored the behavior of one of the four telemetry antennas. The test and the telemetry antennas were of the same basic design. They were boron-nitride filed, cavity-backed, slot antennas differing only in the dimensions necessary to accommodate the test frequency of 2290.5 MHz and the telemetry frequency of 2220.5 MHz. Figure 8 shows the main components and the dimensions of the test antenna.

In addition, a measurement of mutual coupling between two on board antennas was made. The two antennas were the test transmitting antenna and the receiving antenna located at $S/R = 1.84$ and $S/R = 2.30$ respectively. The free space coupling between these two antennas was approximately -14.6 dB.

Four flush mounted electrostatic probes were flown. Two of the

probes had a fixed bias voltage. One of these was located at the center of the nose cap ($S/R = 0$) and was biased at -15 volts to collect the positive ion saturation current. The other probe biased at +15 volts was located at $S/R = 2.58$ for a direct measurement of electron density in the plasma. The two variable bias probes located at $S/R = .475$ and $S/R = 2.58$ were sequentially stepped from -5 to -15 to -30 volts at a rate of 300 times per second.

One stripline probe and a conductivity probe were also included in the diagnostic instrumentation of the AD21.862 vehicle. The conductivity probe and four of the temperature sensors described in a latter part of this section were produced, installed, and serviced exclusively by another contractor. Only the power for the system and the required telemetry channels were provided by Northeastern University. Also, except for a brief examination of the telemetry "quick-look" data, no effort was expended by this laboratory to extract the probable very low level signal, if any, from the telemetry records. Therefore no further discussion of the experiment will be presented in this report. Description of the system and the flight results may be found in references 8 and 9.

To monitor the flight events two accelerometers were installed into the payload. A ± 50 G accelerometer monitored the rocket motor firing times and performance, while a ± 5 G accelerometer recorded the payload deceleration history at the beginning of the reentry period. This information was necessary for the plasma alleviation experiment in A21.011-1 flight. Also included were six temperature sensors. Two of the sensors were intended to monitor the instrumentation temperature during countdown as well as during the flight. One monitored the temperature of the base plate on which the transmitters were mounted, while the other measured the temperature of the inner surface of the nose cap. Four other thermocouples were flown as part of the conductivity experiment. These measured the temperature of the conductivity probe, the skin temperature at the conductivity probe ($S/R = 1.84$), the skin temperature of the nose cap ($S/R = .475$) and the temperature of an inactive electrostatic probe in the nose cap ($S/R = .475$).

The gathered data was transmitted through a standard PAM/FM/FM S-band telemetry system. Four telemetry antennas were located at $S/R = 4.35$ equally spaced around the reentry vehicle. The block diagram of the instrumentation is given in Fig. 9.

C. A21.011-1 PAYLOAD

In addition to the reflectometers and the antenna coupling measuring

apparatus carried by the AD 21.862 vehicle, the A21.011-1 instrumentation included a four probe electric field sampling unit to measure the phase variation of the reflected wave. The test transmitting and receiving antennas were located at $S/R = 2.09$ and $S/R = 2.71$ respectively and had a free space coupling of 15.5 dB.

A liquid injection system to perform a plasma alleviation experiment was also included in the payload. The fluid Freon 114B2 was injected through flush mounted nozzles located just above the transmitting test antenna at $S/R = 1.77$. Six electrostatic probes measured the changes in electron density and the positive ion saturation current. Two variable bias probes, one with a positive bias voltage and one with a negative bias voltage were located between the transmitting and the receiving test antennas at $S/R = 2.4$. The bias levels were switched from 5 to 15 to 30 volts at the rate of 300 times per second. Two other electrostatic probes with a +15 volt bias were located near the telemetry antennas ($S/R = 4.41$). One was placed in a direct line with the injection nozzles ($\theta = 52.5^\circ$) and the other probe was displaced by 90° ($\theta = 142.5^\circ$) in the direction of the spin of the nose cone during reentry. The remaining two fixed bias probes which measured the electron density and the positive ion saturation current were located at $S/R = 2.4$, $\theta = 7.5^\circ$ and $S/R = 1.77$, $\theta = 322.5^\circ$ respectively.

To obtain motor firing times and vehicle acceleration during the thrusting periods one +50G accelerometer was included in the payload. Since past experience had shown that the payload temperature did not change significantly during the flight the temperature of the instrumentation was monitored only during the countdown. A S-band PAM/FM/FM telemetry system was used for data transmission. A block diagram of the instrumentation is shown in Fig. 10.

CHAPTER II

S-BAND MEASUREMENTS

A. REFLECTOMETER

The block diagram in Fig. 11 describes the S-band experiment. The test transmitter operated at 2290.5 MHz producing approximately 3.5 watts at its output terminal. Insertion losses of other microwave components and of the semirigid 0.141 in. cable connecting the transmitter to the antenna reduced the radiated power to slightly below 2.5 watts. The use of this relatively high power transmitter, instead of just a low power oscillator to perform reflectometer measurements, allowed the ground receiving stations to obtain additional information about the signal attenuation and the antenna pattern distortion.

The combination of a directional coupler and a circulator, instead of the usual dual directional coupler configuration, was used to perform the reflectometer measurements. This configuration provided isolation for the transmitter, reduced the size of the system and reduced the required sampling rate of the incident power monitor. The components of the reflectometer were standard subminiature state of the art devices. Some of the operating characteristics of these devices were far from ideal for this application, but a compromise in the choice had to be made between performance and the size of the component. The nominal directivity of the directional coupler was 20 dB. This figure was enhanced by an additional 20 dB isolation provided by the circulator. Therefore the output of the directional coupler was largely independent of the reflected signal. The circulator provided approximately 23 dB isolation between the input terminal and the third terminal at which the reflected power detector was located. This output port was terminated by a 20 dB attenuator with an input VSWR of 1.1 followed by an untuned miniature detector mount. All detector crystals used in the S-band experiment were operated at power levels well above their square law region. Therefore each detector was calibrated as an integral part of the operational system over the expected power range.

The maximum error in the measurement of the voltage reflection coefficient due to the limited isolation is shown in Fig. 12. This error may be introduced by the variation of the detected signal levels resulting from the in-phase and out-of-phase conditions of the incident and the reflected signal components appearing at the third port of the circulator.¹⁰ The two extremes of

the output voltage at that port may be represented by

$$V_o = \Gamma_v V_I \pm V_I 10^{-D/20}$$

where V_I is the incident signal, Γ_v the reflection coefficient at the circulator output terminal (port 2) and D is the effective isolation expressed in dB between ports 1 and 3. Therefore the first term in the equation represents the desired reflected signal and the second term represents the unwanted portion of the incident signal which appears because of the finite isolation provided by the circulator. The measured voltage reflection coefficient Γ'_v may be expressed as

$$\Gamma'_v = \frac{V_o}{V_I} = \Gamma_v \pm 10^{-D/20}$$

and the magnitude of the percent error is given by

$$\epsilon_{\Gamma_v} = 10^{-D/20} \cdot \frac{1}{\Gamma_v} \cdot 100$$

The error in the measured power reflection coefficient may be expressed as

$$\epsilon_{\Gamma_p} = \frac{10^{-D/10} + 2 \cdot 10^{-D/20} / \Gamma_p}{\Gamma_p} \cdot 100$$

where Γ_p represents the actual power reflection coefficient at the output terminal of the circulator. The error becomes quite large as the reflection coefficient decreases. Therefore at low reflected power levels it is advantageous to obtain the reflection coefficient through the four-probe field meter technique described in the following section of this report.

A similar reflectometer arrangement was used to measure the reflection coefficient of one of the telemetry antennas. A more detailed description of the reflectometer may be found in the section describing the telemetry systems.

B. MULTIPROBE FIELD METER

A multiprobe stripline field meter was used to measure the test antenna impedance during the flight and reentry periods. The requirements of being small, very rugged, and easy to manufacture led to the selection of a

stripline device. Fast response time was also a necessity because of the rapid impedance changes caused by reentry plasma fluctuations.

The device was manufactured from two sheets of double copper clad teflon filled stripline board that were etched to form a 50 ohm transmission line and four equally spaced probes (Fig. 13). The probes were loosely coupled (23 dB) to the transmission line in a manner similar to that of a slotted line.¹¹ Since only a single frequency (2290.5 MHz) was used the probe spacing was chosen to be one eighth of a wavelength to obtain maximum sensitivity.¹² The boards were designed with quarter wave shorting stubs and provisions for Schottky barrier detector diodes. These stubs provided the dc return path for the detector diodes while presenting an open circuit to the signal. Each detector output was followed by a signal conditioning circuit (Fig. 14) that interfaced the signal with the telemetry system input. The probes were calibrated by sequentially locating the peak of a standing wave at each probe with a sliding short and then varying the incident power with a variable attenuator.

Only three probes are necessary to obtain the information for impedance calculations. The fourth probe was introduced to give redundancy in the information and to act as a spare in case one probe or its associated electronics should fail. Also, having four probes allows impedance measurements to be made four different ways by using three probe outputs at a time.

As a matter of convenience a reference point was chosen at which the impedance would be measured. The point chosen was the end of the stripline where the antenna cable was connected. The free-space impedance of the antenna was measured from this reference point, with the flight cable connected to the antenna. Choosing this reference point eliminated the need to know the exact length of the antenna cable and its associated connectors.

The impedance at the reference point can be calculated several ways,¹³ two of which will be discussed here. The first three probe outputs will be considered initially, resulting in equations that are applicable to the remaining three sets of probes. Let V_I be the incident voltage on the transmission line and V_n the standing wave voltage at the n th probe. If ρ and ϕ are the magnitude and angle of the reflection coefficient Γ of the antenna as seen from the reference point, then

$$(1) \quad \Gamma = \rho e^{j\phi}$$

and

$$(2) \quad V_n = V_I (1 + \rho e^{j(\phi - 2\pi z_n)})$$

where φ_n is the phase shift corresponding to the distance from nth probe to the reference point. Since the probe has a peak detector and it is calibrated in terms of transmission line power, equation (2) may be written as

$$(3) \quad P_n = V_n^2 = 1 + \rho^2 + 2\rho \cos(\theta - 2\varphi_n)$$

where P_n is the standing wave effective power at the nth port. Equation (3) written for probes $n=1, 2, 3$ will result in three simultaneous equations containing three unknowns. Of the three unknowns, θ , ρ , and V_I , the two that are of interest for impedance measurements are θ and ρ . Solving the equations results in the following:

$$(4) \quad \theta = \arctan - \frac{P_1 C_{32} + P_2 C_{13} + P_3 C_{21}}{P_1 S_{32} + P_2 S_{13} + P_3 S_{21}}$$

where

$$C_{32} = \cos 2\varphi_3 - \cos 2\varphi_2$$

$$C_{13} = \cos 2\varphi_1 - \cos 2\varphi_3$$

$$C_{21} = \cos 2\varphi_2 - \cos 2\varphi_1$$

$$S_{32} = \sin 2\varphi_3 - \sin 2\varphi_2$$

$$S_{13} = \sin 2\varphi_1 - \sin 2\varphi_3$$

$$S_{21} = \sin 2\varphi_2 - \sin 2\varphi_1$$

and

$$(5) \quad \rho = \frac{1}{4P_I} (P_1 C_{32} + P_2 C_{13} + P_3 C_{21})^2 + (P_1 S_{32} + P_2 S_{13} + P_3 S_{21})^2)^{1/2}$$

P_I is the incident power in the transmission line and is a known constant. It should be pointed out that P_I could be determined from the probe outputs by solving equations (3) for V_I^2 but since P_I is already known, this would simply lead to another source of error.

Equations (4) and (5) are cumbersome for hand calculations but are well suited for computer reduction of the impedance information. A second method of deriving equations for ρ and θ results in much simpler equations that are suitable for hand reduction of information. The derivation starts in a manner similar to the one previously described. Trigonometrically manipulating the three simultaneous equations for the three probes that are spaced one eighth of a wavelength apart results in equation (6).

$$(6) \quad \theta = \arctan \frac{-P_1 + P_3}{P_1 + P_3 - 2P_2} + \varphi_R$$

The arctan function gives the phase angle at the center probe being considered and φ_R refers this angle to the reference point previously established. Since the arctan is a discontinuous function, φ_R must compensate at the discontinuities to result in a continuous θ function. A simplified equation for ρ will result if simultaneous equations are written for all four probes.

$$(7) \quad \rho = \frac{1}{4P_I} (P_1 - P_3)^2 + (P_2 - P_4)^2)^{1/2}$$

With this equation all four probes are required but the position of the probes with respect to the load is not needed. The disadvantages of these simpler equations are that the θ calculation must have a correction factor φ_R and the ρ calculation requires all four probes, eliminating the benefit of redundancy.

The quantities ρ and θ can now be calculated three more times, thus using all four probe outputs three at a time. If the resulting four θ 's and four ρ 's agree within acceptable limits, the measurements may be assumed to be reasonably accurate. If it is desired, the four respective calculations may be averaged for greater accuracy.

The system accuracy was determined in the laboratory by terminating the reflectometer with several known loads connected through a line stretcher. The line stretcher was moved by equal increments corresponding to equal changes in phase. The measured θ and ρ were then calculated and compared with the known shifts in phase and the magnitudes of the different reflection coefficients of the known loads. The resulting errors in θ and ρ are plotted versus ρ of the known load in Figures 15 and 16. As can be seen, the error in θ increases as the known ρ decreases while the measured error in ρ increases as the known ρ increases.

C. MUTUAL COUPLING

The mutual coupling between the two test antennas was measured simply by detecting the received signal. The measured result included the signal strength variations due to reflections taking place at the transmitting antenna as well as the signal variations due to changes in mutual coupling. The separation of the two effects had to be accomplished during the data reduction process on the ground.

At first it was assumed that the coupled power would not change by

more than 25 dB during the experiment. Therefore, in order to observe the variations in mutual coupling with a reasonable degree of resolution, the total expected signal range was divided and transmitted over two separate telemetry channels. The detected signal was processed by two cascaded operational amplifiers. The output of the first amplifier supplied the data during the reentry interval when the strength of the coupled signal was relatively large. At that time the second amplifier was saturated and its output was clipped at five volts. When the coupled signal decreased to a low level the output of the second amplifier provided the data. The results of the AD21.862 flight showed that the dynamic range of the signal amplifiers was insufficient. Eventually during the reentry the coupled signal decreased to such low levels that any meaningful recovery of the data, even from the high gain amplifier was impossible. Since good data were obtained at the beginning of the reentry period, when the coupled signal was relatively large, it was decided to increase the dynamic range of the signal conditioning circuits and to emphasize the data resolution only at the lower signal levels. The dynamic range of the signal amplifier for the A21.011-1 flight was set at 35 dB and only one telemetry channel was used for data transmission. The signal conditioning circuit is shown in Fig. 17. In this configuration the detected microwave signal (current) was passed through a silicon signal diode for which an operational amplifier provided a low impedance return. The dc circuit was completed through the impedance of the 6 dB microwave attenuator used to reduce the coupled power into the crystal detector to a safe operating level. The unity gain follower with the forward biased diode at its non-inverting input provided the temperature compensation. Signal amplification as well as offset control was obtained from the output stage.

CHAPTER III

PROBES

A. FIXED BIAS ELECTROSTATIC PROBES

Flush mounted electrostatic probes were flown on the Trailblazer's reentry nose cone to obtain plasma density information.¹⁴ Each probe consisted of a 0.25 inch diameter gold-plated copper electrode insulated from the vehicle by a cylindrical lava dielectric (Fig. 18). The probes were provided with either positive or negative voltage bias. The positive bias probes collected electrons and the negative bias probes collected positively charged ions. Some probes had a fixed bias (+15V or -15V) while others had a switchable bias (5, 15, 30V or -5, -15, -30V) which was stepped sequentially through the voltage levels to provide probe saturation current information at different flow field depths. The bias levels were switched 300 times per second, providing 10 samples at each bias level for every revolution of the vehicle about its center axis. This sampling rate was more than adequate to reconstruct the signal and was compatible with the standard IRIG 10 x 50 commutator format which will be discussed later in the report. Figure 19 shows a flight package using cordwood construction containing the electronics for both a fixed and a variable bias electrostatic probe.

The fixed bias electrostatic probes are much simpler in design than those of variable bias. A block diagram of an electron collecting fixed bias probe is shown in Fig. 20. Each probe contains a single transformer dc-dc converter with a nominal 27 Vdc input. Two output windings supply power to a ± 15 V voltage regulator which is used to run the circuitry. A 15V floating regulator is powered by a third isolated winding. The floating regulator is used to provide the probe bias and is current limited to three times the maximum expected probe current.

The expected probe currents vary over many decades during the time of reentry, making a linear measuring system unfeasible. The probe currents are therefore measured by logarithmic amplifiers to provide good low level sensitivity and a wide dynamic range. A log amplifier circuit for an electron collecting probe is shown in Fig. 21. A common signal diode acts as the necessary logarithmic element, producing a voltage proportional to the log of the current passing through it. The diode is followed by an operational amplifier provided with temperature compensation circuitry. The input diode logarithmic characteristic for any particular current is temperature dependent both in magnitude and slope. To compensate for the magnitude

shift another diode similar to that of the input is biased with a constant current followed by an isolation operational amplifier with near unity gain. To compensate for change in slope of the diode characteristic, a thermistor-resistor series-shunt combination is introduced into the feedback circuit. The result of temperature compensation and the logarithmic nature of the amplifier can be seen in Fig. 22 which shows a typical calibration curve which is valid over the range of 70°F to 150°F. As can be seen, four decades of input current can easily be achieved.

The log amplifier is followed by an output amplifier that provides the necessary gain and dc offset to meet the telemetry system input requirements. A calibration circuit is introduced to calibrate and confirm operation of the probes during payload testing and prior to the launch. The calibrator is a transistor which when remotely activated places a resistor across the probe, causing a predetermined current to flow.

A coaxial cable is used to connect the probe in the skin to the probe electronics inside the payload. The center conductor of the coaxial cable is connected directly to the input diode and the shield is grounded at the diode with the other end left open. This shielding is especially important at low current levels when the input diode impedance is very high. The coaxial cable increases the effective shunt capacitance of the diode and thereby reduces the low end frequency response of the system. Nevertheless, with the fixed bias probes the transient and frequency response of the system are found to be more than adequate.

The positive ion probes differ from the electron collecting probes in several ways. The bias supply polarity is reversed and the diodes of the log amplifier are inverted. The calibrator transistor is replaced with a complementary transistor to accommodate the change in bias polarity. Also, a non-inverting output amplifier must be used.

B. VARIABLE BIAS ELECTROSTATIC PROBES

The variable bias electrostatic probes are considerably more complex than those having fixed bias. A block diagram of a positive ion collecting variable bias probe is shown in Fig. 23. Each switchable probe contains a two transformer dc-dc converter with a nominal 27 Vdc input. Four of the output windings power two ± 15 voltage regulators that run the floating and non-floating circuitry. A fifth and sixth windings supply power to the switchable bias and logic regulators. The switchable bias regulator is current limited to three times the maximum expected probe current.

The probe currents are measured by logarithmic amplifiers similar to

those used in the fixed bias probes. The probes that are expected to measure very low currents (below 10^{-6} A) require FET input operational amplifiers having very low bias currents. In contrast to the fixed bias probes the variable bias probes float the log amplifier upon the switchable probe bias supply. If this were not done the rather large capacitance between the switchable supply transformer windings and the other windings would allow switching transients to dominate the input diode at low current levels. By floating the log amplifier the switching transients are minimized. Furthermore, at very low current levels the input diode becomes reversed biased from transition of the switchable voltage regulator from the 30V to the 5V level. Under this condition the diode impedance is very high and recovery of the diode to steady state is slow. To speed up recovery a steady state restoration circuit (Fig. 24) is introduced. This circuit contains a pulse transformer whose primary winding is connected across the switchable bias supply. During the 30V to 5V bias transition the transformer pulses on a p-channel enhancement MOSFET and places a resistor across the probe. The diode recovers quickly when shunted with this low impedance and upon removing the resistor the log amplifier is ready for current measurement. The same transistor and resistor are also used to calibrate the probe.

To minimize noise pickup coaxial cable is used to connect the probe at the skin to the electronics. The center conductor of the coaxial cable is connected directly to the input diode and the shield is tied to the switchable bias supply. Floating the shield in this manner minimizes the switchable supply transient effects by maintaining the coaxial center conductor to shield voltage relatively constant. The coaxial cable increases the effective shunt capacitance of the probe but the low level frequency response of the system remains more than adequate.

The switchable bias supplies use a μ A723 monolithic voltage regulators. Schematics for both positive (electron collecting probe) and negative (positive ion collecting probe) voltage switchable regulators are shown in Fig.'s 25 and 26 respectively. The regulator is provided with two transistor switches that are activated by the control logic. These switches control feedback resistors that determine the magnitude of the regulator output voltage. If no control voltages are applied the regulated output is 5 volts. When either of the two appropriate control voltages is applied, the corresponding regulator output will be 15 or 30 volts. By properly sequencing the control voltages the switchable voltage regulator is stepped from 5 volts to 15 volts to 30 volts.

The output of the log amplifier, now superimposed upon the switching bias level, is followed by a unity gain isolation amplifier and a common mode rejection circuit (Fig. 27). This circuit consists of two temperature stable

resistor dividers followed by an operational amplifier. The divider ratios are selected to provide both inputs with equal gains and to bring the voltage levels within the common mode range of the operational amplifiers. The output of the common mode rejection circuit is the log amplifier data output for a sequentially stepped bias probe. In order to relate the data to the proper bias levels and to minimize telemetry channel space a simulated commutator is used.

The simulated commutator has a standard RZ 10 x 30 IRIG format as described later in the report. A diagram of the commutator system is shown in Fig. 29. The clock (Fig. 28) is a temperature compensated unijunction oscillator producing 600 pulses per second. The format control logic is a divide 60 counter with peripheral gates and a divide by three counter that produce the synchronized gate and switchable bias supply control signals. Standard TTL SN5400 integrated circuits are used. Outputs T-15 and T-30 control the switchable voltage regulator while outputs Y1, Y2, Y3, and Y4 control the output gates. VR1 (1.25 volts) and VR2 (5.00 volts) are the reference voltages used to produce the zero data (1.00 volts) and full scale (5.00 volts) reference voltages. Four n-channel FET gates and drivers are used to time multiplex the data, reference, and sync pulses and provide return to zero intervals. The gates are followed by a precision network and a gain of two amplifier. The gate control waveforms Y1, Y2, Y3, and Y4 are shown in Fig. 30 along with a typical system output and the corresponding bias levels.

When gates S1 and S4 are closed the two reference voltages cause 5.00 volts to appear at the system output. This voltage is used in the sync and full scale reference pulses. Any time gate S4 opens the amplifier input is grounded and the return to zero interval is obtained. This interval occurs during the first half of the bias level period to allow settling time before the sample is made. When gates S3 and S4 are closed the zero scale reference voltage is obtained. Finally, the data appears at the system output when gates S1 and S4 are closed. The system output is now in a commutator format which may be transmitted on one telemetry channel and decommutated on the ground.

On flight A21.011-1 a three data channel PAM RZ 10 x 30 IRIG format simulated commutator was flown to conserve available telemetry channels. The commutator is similar to that used in the variable bias electrostatic probes and therefore will not be discussed any further. The three available data channels were used to monitor the two electron collecting probes at $S/R = 4.4$ and the telemetry incident power.

C. STRIPLINE PROBE

The stripline probe (Fig. 31) was included in the AD21.862 flight to observe the effects of the plasma sheath on the parameters of the probe and to compare the results with laboratory observations. The probe, a modification of a microstrip line, was a lossy feedthrough transmission line.¹⁵ The resistance strip, 4 in. long, 0.5 in. wide and .0315 in. deep was backed by a 5 x 1 x 0.5 in. cavity filled with 14 lb/ft³ density Eccofoam. The surface facing the plasma was covered by a .125 in. layer of boron nitride dielectric material. Two coaxial connectors provided access through the cavity to both ends of the resistive strip.

Although a nonradiating device in itself, the stripline possesses some fringing fields which extend beyond the cavity. This makes the stripline characteristics sensitive to any conducting surface, such as a plasma sheath, placed near the open side of the line. The main effect of the conducting surface is to add capacitance in parallel with the already present capacitance which exists between the resistive strip and the walls of the cavity. This added capacitance changes the characteristic impedance of the line and thus the attenuation and the reflection coefficient. As a conducting surface nears the stripline, the characteristic impedance of the line decreases, while the attenuation of the transmitted signal increases. This behavior of the line may be predicted and the expected changes in its transmission characteristics calculated from the transmission line equations.

The block diagram in Fig. 32 describes the stripline instrumentation which resembles the S-band experiment arrangement described in the preceding section of this report. Incident, reflected and the transmitted power through the stripline probe were measured. Under free space conditions the probe exhibited a reflection coefficient of 0.6 and an insertion loss of 17.5 dB. The expected range of variation for these two parameters during the flight was established by moving a curved metal sheath from a distance of a few centimeters until it touched the surface of the probe. The insertion loss increased monotonically from the free space value to 27.8 dB and the reflection coefficient decreased to 0.4. These values were used as the design limits for the detector and the signal conditioning circuits.

The power to the stripline was supplied by a 400 MHz oscillator producing approximately 11 milliwatts. A subminiature lumped parameter directional coupler monitored the incident power. Reflected power was measured with a narrow band lumped parameter circulator terminated by a matched crystal detector. The same circulator also provided the required isolation

for the microwave oscillator. A solid state microwave amplifier interposed between the output of the stripline probe and the detector mount boosted the transmitted and greatly attenuated signal by 10 dB. Semirigid 0.141 and 0.085 inch cables were used to interconnect the various components of the stripline system. The detector mount was produced from a single block of metal and included not only the three crystal detectors but also impedance matching resistors as well as three additional diodes for temperature compensation of the signal conditioning circuits.

A diagram of the signal amplifiers is shown in Fig. 33. The output stage of the circuits provided the required gain and the offset voltage to accommodate the expected signal range from each of the three detectors. The other operational amplifier with a forward biased diode (from the detector mount) at its non-inverting input terminal was used for temperature compensation. Matching of the diode temperature characteristics to the individual circuit requirements was accomplished by adjusting the diode bias current and the gain of the compensating amplifier.

CHAPTER IV

INJECTION SYSTEM

The alleviation experiment was designed to reduce the plasma electron density in the vicinity of the test antennas by injecting small quantities of electrophilic liquid.¹⁶⁻¹⁸ Freon 114B2, a relatively dense (2.175 g/cm^3) liquid with a low boiling point (47.3°C) and an excellent drop forming ability was chosen as the alleviant. The function of the injection system was to introduce pulses of Freon into the shock-ionized flow field while trying to maintain a somewhat constant mass ratio between the ionized air flowing over the antennas and the alleviant. Since the experiment was to be performed over 300,000 to 100,000 ft. region where the pressure and consequently the air mass flowing over the antennas varies considerably, two different injection modes were used. In the interval between 300,000 to 170,000 ft. the liquid was injected at essentially constant, relatively low flow rates, while below the 170,000 ft. level a continuously increasing flow rate injection was used. The pulsed mode of injection not only reduced the amount of fluid required for the experiment, but also made it possible to obtain some quantitative measure of the effectiveness of the alleviant over a wide range of conditions.

A photograph of the assembled injection deck is shown in Fig. 34. The liquid was carried in a stainless steel cylinder. From this reservoir two separate branches of tubing led to two sets of injection orifices located in a nozzle plate just above the transmitting test antenna ($S/R = 1.77$). The low-flow-rate branch had two .026 in. diameter orifices, while the high-flow-rate injection was accomplished through six .023 in. diameter holes. Injection was controlled by two solenoid valves with .032 in. and .093 in. diameter openings for the low and the high flow branches respectively. To avoid a possible clogging of the injection nozzles two 40 micron filters were included in the lines. The reservoir and the two tubes leading to the solenoid valves, when properly filled, could hold approximately 89 cm^3 of the alleviant. A piston was used to force the liquid from the cylinder into the lines and out of the orifices. When the piston was moved back during the filling operation, approximately 30 cm^3 of air at atmospheric pressure was trapped in the space behind it. This trapped air and the centrifugal force due to the spin of the vehicle supplied the drive to the piston during the high altitude experiment. At low altitudes, where relatively high injection rates were required, compressed gas provided the driving force for the piston. The nitrogen gas compressed at 3000 psi was contained in a 42.6 cm^3 explosively activated cylinder.

When released, the gas passed through a regulator and the pressure was reduced to a constant 550 psi. To achieve the continuously increasing rate of liquid injection the pressure on the piston was built up gradually by allowing the gas to flow through a constriction in the line. This constriction was 0.25 inches long and had an inside diameter of 0.01 inches.

The amount of liquid injected into the shock-ionized flow field was measured by monitoring the travel of the piston and by observing the pressure of the alleviant in the cylinder as well as at the nozzle plate. The miniature threaded, bolt type pressure transducers were mounted directly into the walls of the containers. The sensing surface (a stainless steel diaphragm) had a Wheatstone bridge of silicon resistors deposited by diffusion techniques. The sensors located in the cylinder and in the high-flow-rate line were capable of 500 psi full scale measurement, while the sensor in the low-flow-rate line had only 50 psi capability. The movement of the piston was monitored by a 3 in. linear displacement transducer with a 0.003 in. resolution. This high resolution was required to detect and measure the small amounts of fluid expended during each pulse (approximately 0.9 cm^3) in the high altitude portion of the experiment. The output of the linear displacement transducer was transmitted in two parts. A high gain amplifier was used to process the signal during the high altitude experiment. When the motion of the piston became large during the high-flow-rate injection, the amplifier output was clipped, and the data were transmitted directly from the transducer on a different telemetry channel. The output signals from the pressure transducers were also processed by operational amplifiers connected into an instrumentation amplifier configuration. All of these transducer output signals were commutated at 90 samples per second for telemetry transmission.

The control of the various phases of the experiment was accomplished through timing and through detection of predetermined deceleration levels. In the 300,000 to 275,000 ft. region, where the high altitude experiment was to begin, the electron density in the flow field could not be predicted with sufficient accuracy to be useful as the trigger mechanism to start the injection sequence. Past performance records of the Trailblazer II vehicle indicated that the time between the fourth stage ignition and the arrival of the nose cone at the 300,000 ft. level differed by not more than two seconds regardless of other variations in flight parameters. Therefore a direct timing was chosen to start the high altitude phase of the experiment. The timers were to operate approximately 22 seconds after the fourth stage ignition. The measured delay times before final assembly of the vehicle were 21.6 and 21.8 seconds for the primary and the back-up circuits respectively. The

timers started the operation of the low-flow-rate solenoid valve. During this high altitude portion of the experiment the valve was open for approximately 250msec once every second thus allowing the liquid to flow during three out of every twelve revolutions of the nose cone. As a back-up for the timers, a sufficiently large output voltage of an electrostatic probe located near the test antennas was also able to start the experiment. The override signal was set to correspond to an electron density encountered during normal flight near 245,000 ft. altitude.

The start of the low altitude experiment was signaled by a closure of a 2.5 G acceleration switch. This level was selected from the observations of the deceleration history and the encountered electron density by the nose cone of the AJD21.862 vehicle. The deceleration of 2.5 G's occurred at an approximate altitude of 170,000 ft. where the plasma reached sufficient density for the high volume injection to begin. A second G-switch operating independently in a parallel system served as a back-up trigger.

Closure of a G-switch activated the pressure cylinder and at the same time started the operation of the high-flow-rate valve. Therefore during the low altitude phase of the experiment the injection sequence was modified. The low volume injection pulse was followed by a high volume pulse of equal duration (250 msec) and then both of the solenoid valves were closed for 500 msec by electronic circuits.

Redundant electronic control of the timing and injection system was used to minimize the possibility that a minor component or connection failure could completely destroy the experiment. Since only a relatively short time reliability was necessary and the available space for the circuits was limited, dual circuit redundancy with a fault detector was used, instead of the more reliable series-shunt four element approach. Even the dual redundancy was somewhat compromised in that a failure of one of a few selected components would allow the low-flow-rate injection to operate prematurely. Such an event would have more or less reduced the range of the experiment but would not have destroyed it completely. Also the large mean time between failures (MTBF) of these few selected components made such a premature operation of the system a very remote possibility.

A general block diagram of the injection control is shown in Fig. 35. In the diagram the switches S1 and S2 were two separate DPDT normally open relays designed to operate under severe shock and acceleration conditions. The G-switches identified as G1 and G2 were set to close at the 2.5 G deceleration level and to open when the deceleration dropped below one G level. The SHORTS represent a shorting connector which was removed upon the sep-

aration of the nose cone from the spent third stage motor. These shorts prevented the operation of the timers, disabled the firing circuits for the explosively activated pressure cylinder and stopped the electrostatic probe signals from triggering the low-flow-rate injection sequence.

The signals from two of the electrostatic probes were able to start the injection experiment when a reasonable electron density was indicated. This feature was introduced to assure that the injection of the alleviant would take place even if the 22 second timers failed to trigger the system. This condition could occur if for some reason the fourth stage motor firing was delayed (this firing was timed from the lift-off) and the reentry would begin sooner than anticipated. Since no plasma was expected before reentry, the short was there primarily to prevent the ES probe calibration sequence from introducing premature triggering.

As soon as the power was applied to the payload the two valve driver circuits started operating (Fig. 36). Two synchronized UJT clocks operated at 4 pps and triggered a two bit ripple counter. The outputs of the counter were connected through the diode AND gates to the valve driver transistors and produced the one second injection sequence. The low and the high volume injection valve driver transistors were saturated sequentially for 250 msec each. This was followed by a 500 msec pause when both transistors were OFF. The turn-on time of the valves was approximately 3 msec, but the turn-off time varied to some extent, and in some instances could reach 20 msec. Therefore, the valve ON-time was slightly longer than the 250 msec driving pulse and there was a slight overlap at the end of the low-flow-rate pulse when the high-flow-rate valve opened.

When both relays (S1 and S2 in Fig. 35) were open the current through the valve solenoids was limited to a few milliamperes by the 10K resistors. This current was insufficient to operate the valves, but provided the signals for the monitor circuit. The monitor circuit (Fig. 37) received the switching signals directly from the solenoids (the valves and the control circuits were at different locations in the payload) differentiated them and periodically discharged the capacitor of the UJT delay circuit. The arrangement was such that once every 500 msec a positive pulse appeared at the discharge transistor indicating that a proper voltage change has occurred at one of the solenoid valves. The UJT timer was set to trigger the SCR 600 msec after the last discharge of the capacitor. Therefore, if the voltage at either solenoid did not change in the proper direction within this interval, the SCR was triggered and the relay S3 transferred the valve control to the secondary system. Since the binary counters of the two systems were also synchronized, the

same sequence of valve operation was continued. The two events monitored by the transfer circuit were the opening of the low-flow-rate valve and the closing of the high-flow-rate valve. Therefore, the most serious event that could have occurred during the injection sequence would have been the failure of the driver circuit to close the high-flow-rate valve. In that case, the loss of fluid through the valve before the switchover closed it would have reduced by one the predicted number of injection pulses.

In-flight system status information such as the operation of the valves and the closing of relays or G-switches was also provided by the monitor circuit. The valve operation sequence was indicated by a three-level stepping voltage, while the closing of switches, first the relays and later the G-switches, added more DC bias to that voltage.

When the spherical fourth stage motor fired it removed the shorting connector attached to the spent third stage of the vehicle. This started the 22 second timers by allowing the capacitor in the UJT circuit to charge (Fig. 38). When the transistor fired it activated the SCR and closed the switches S1 and S2. The low-rate injection valve received the full current and the high altitude experiment was underway. Also the firing circuits for the pressure release became armed and ready to fire.

At a deceleration level of 2.5 G's the G-switches closed and activated the explosive valve releasing the compressed gas and applying pressure to the piston in the liquid tank. The high-flow-rate valves also started operating at that time. When the G-switches connected the supply voltage to the emitter of the series transistor (Fig. 39) the trigger circuits produced the required 2.5 ampere, 2 msec pulse to activate the pressure release valve. This circuit was interposed between the battery and the valve to prevent a short circuit, which may have developed after explosion, from discharging the battery. Additional protection was provided by the ten-ohm, quarter-watt resistor in series with the igniter which limited the current and also served as a fuse.

CHAPTER V

TELEMETRY SYSTEM

The S-band PAM/FM/FM telemetry system (Fig. 9 and 10) operated at 2220.5 MHz. Each of the four antennas radiated slightly more than one watt of power. They were located near the base of the nose cone to insure that the radiated signal attenuation by the plasma sheath was minimized. The electron density at that location was considerably less than at the test antenna and therefore the telemetry signal continued to be received even after the test signal has been completely blacked out.

During the AD21.862 flight the power to the antennas was supplied via a matched, but unisolated, four-way power divider. This arrangement was quite satisfactory during the free space flight, but during the reentry the power delivered to any antenna was a function of the relative magnitudes and phases of the reflected waves from other antennas. This continuously changing power distribution was evident from the incident power variations monitored by the reflectometer at one of the antennas. Undoubtedly this variation affected the antenna pattern and, although it might not have degraded the signal, it certainly made the evaluation of the plasma effects on the telemetry signal more difficult. Twenty-three dB isolation was provided for all four antennas on the A21.011-1 flight.

The combined radiation pattern of the four antennas exhibited four rather narrow but deep nulls which extended up to 24 dB below an average level. The antenna patterns shown in Fig. 40 are for the 60° and the 70° look angles. They illustrate the approximate signal strength variation that would be seen by the receiving antennas in the absence of plasma over the reentry altitudes. The look angles represented in the plots are formed between the roll axis of the nose cone and the central axis of the beam of the receiving antenna. The angles along the horizontal axis of the plots represent the rotation of the vehicle. Since the predicted signal performance margin at the beginning of the reentry period varied from 35 dB for the Advanced Data Acquisition System to 25 dB for the Mobile Site, the narrow nulls were not considered to present a serious threat to a good data reception.

The subcarrier and the commutator channel assignments for the two flights are given in Tables III and IV. All commutated data associated with a direct measurement of the plasma parameters was sampled between 80 and 120 times per second. This ensured at least six data samples during one complete revolution of the reentering nose cone.

The commutator used to sample the various signals provided 28 pulse-amplitude-modulated (PAM) data channels and one synchronization pulse at the rate of 30 frames per second. Some of the electrostatic probe data were also presented to the subcarriers in a commutator format having 28 channels and operating at a rate of 10 frames per second. The output format used was the return to zero, 50 percent duty cycle with a full scale frame synchronization pulse and a one volt positive pedestal in each data channel. The frame synchronization pulse occupied three segments and had a full scale amplitude of 5 volts. Because the one volt positive pedestal was used for channel synchronization, the commutated data was compressed. An input data which varied between zero and five volts were represented in the output of the commutator as a signal ranging from one to five volts. Of course, the compression of the data was automatically removed during the decommutation process.

A standard IRIG proportional bandwidth subcarrier system was used.¹⁹ The voltage controlled subcarrier oscillators accepted signals from zero to five volts which produced ± 7.5 percent frequency deviation about their center frequencies. To conserve space the oscillators were microminiature hybrids, also known as wafer oscillators. One megahertz RF bandwidth was utilized for data transmission. The total transmitter deviation was apportioned among the subcarriers according to the well known three-halves-power pre-emphasis setting.²⁰ The deviation of the transmitter by the lower frequency subcarriers was somewhat increased from the calculated values to overcome any incidental frequency modulation which may have been present in the carrier.

CHAPTER VI

PERFORMANCE AND DATA

Telemetry records indicate that in general the vehicles and the instruments performed well during both flights. The AD21.862 vehicle functioned within the predicted performance limits and reached the 18,000 ft/sec reentry velocity. The flight pattern of A21.011-1 rocket deviated somewhat from the nominal performance parameters. The nose cone reentered at slightly shallower angle than expected and developed a peak velocity of only 16,200 ft/sec. For this reason the vehicle not only survived the reentry but also remained in the region of plasma densities, which in the records of the previous flights could be observed only as very brief transitions. Also the telemetry signal was received without interruption throughout this flight. Time measured from lift-off and the corresponding altitudes for the two vehicles over the reentry range are given in table V.

A. AD21.862

Shortly after lift-off of the AD21.862 vehicle the Advanced Data Acquisition System (ADAS) of the Wallops Station experienced a breakdown and lost the telemetry signal. Also the main back-up receiving station located down-range in the Coquina Beach, Va. area had some difficulties with the receiving equipment and produced a rather noisy signal. The loss of the two main receiving sites left only the van at the Wallops Station to receive the telemetry signals. This resulted in an 18dB reduction of the expected carrier to noise ratio. Combination of this reduced performance margin and the variation in the transmitted signal strength due to the nulls in the antenna pattern produced a considerable number of clicks in the telemetry data throughout the flight. The noise generated clicks became more numerous during reentry and are clearly visible in the data obtained from the TM reflectometer shown in Fig. 41. In both of the records reproduced in that figure zero dB refers to the TM incident power level at the antenna under free-space conditions.

The fine structure visible in the reflected as well as in the incident power of the TM antenna was caused by the rotation of the nose cone. Since the nose cone reentered the atmosphere at an angle of attack different from zero the plasma density around the vehicle varied considerably. This plasma density variation produced continuously changing reflection coefficient at the

antenna and thus the cyclic variation in the reflected power. Superimposed upon the variations caused by the antenna reflection coefficient are the changes in the incident power. These incident power variations were caused by a redistribution of the power within the four-way power divider. As was mentioned earlier in the report, three branches of this divider were unprotected against reflected power. The variations in the magnitude and the phase of the reflected waves from the three antennas produced complex impedance changes at the divider junctions affecting the power distribution. Incident power variations in excess of 10 dB occurred between 411 and 412 seconds after lift-off. In the same altitude region between 70 and 80 percent of the incident power was reflected resulting in an approximate 10 dB reduction of the radiated power from that antenna. A burst of noise may be observed just before 413th second marker. At that point AGC records of the receiver indicated that the average signal attenuation reached approximately 20 dB below the free-space level measured just before the beginning of the reentry period. Extraction of any useful information from the TM records after this time becomes rather difficult.

The behavior of the test signal during reentry may be observed in Fig. 42 where the telemetry records of the reflected and the coupled power are shown. Since the transmitter was protected by the circulator of the reflectometer, the incident power remained constant throughout the flight. In the reflected power record the dB scale is once again referred to the free-space incident power level, while the scale on the two coupled signal traces is referenced to the coupled signal level under free-space conditions. As can be observed there was some increase in the coupled power at the beginning of the reentry period. In less than a second both coupled signal amplifiers bottomed indicating that the received power decreased by more than 25 dB which included a 10 dB contribution by the decrease in the radiated power of the test antenna. Thus the mutual coupling between the two test antennas decreased more than 15 dB. Once again a considerable number of noise clicks become evident in the records as the plasma density increased during the reentry.

The data obtained from the stripline probe indicates that the transmitted as well as the reflected signals varied over a greater range than expected. It may be observed in Fig. 43 that there was a slight increase in the transmitted signal at the very beginning of the reaction period while the reflected power remained constant. Following this brief interval there appears to be a break-up of the signal. This was the result of insufficient sampling rate of the signals (120 samples/sec) by the commutator during the rapid build-up of plasma at the probe. Finally the transmitted power decreased below the

range of the signal conditioning amplifier and remained there until the loss of the signal. The reflected power decreased as expected and produced cyclic variations where the return loss first ranged from 13 to 7.5 dB and then stabilized in the 10 to 7.5 dB range. The rather erratic signal near the end of the trace was caused by noise in the signal being decommutated.

The electrostatic probe data taken during the reentry period of vehicle AD21.862 is displayed in Figs. 44-47. The data is presented as probe current plotted versus time from rocket lift-off. Fig. 44 displays the behavior of the fixed bias positive ion collecting electrostatic probe located at the nose cone stagnation point (refer to Table I for probe locations). As can be seen at 407 seconds the probe current started increasing in a smooth continuous manner and by 410 seconds it had reached its maximum value. At 412 seconds some noise in the system became apparent and by 414 seconds the noise had increased to such an extent that no usable data could be extracted from the records.

The behavior of the fixed bias electron collecting electrostatic probe located at $S/R = 2.58$ is displayed in Fig. 46. Since the probe is not located at the stagnation point sinusoidal modulation caused by the spin of the vehicle appears superimposed upon the probe current build up. The probe current is larger on the windward side of the vehicle where the plasma density is greatest and smaller on the leeward side where the plasma density is a minimum. It should be pointed out that most of the electrostatic probe data was commutated, resulting in the staircase effect seen in the TM data. The average probe current increased in a manner similar to that of the probe located at the stagnation point.

Fig. 47 presents the positive ion current data for the variable bias electrostatic probe located at $S/R = .475$. Three graphs are used to present probe currents for each of the three bias levels. As was expected the probe currents of the higher voltage bias levels were larger and appeared slightly before those of the lower voltage bias. At approximately 409.5 seconds the 15V and 30V bias data become very erratic due to a faulty ground station decommutator. Since at that time it was not possible to remake the strip charts using another decommutator the data is presented here with the envelope of the correct data shown with dashed lines. The corrected data were obtained from other records which due to different processing and scale could not be reproduced in this report.

B. A21.011-1

The liquid injection system performed well. Timers initiated the high altitude experiment at an approximate altitude of 280,000 ft., 21.6 seconds after the fourth stage ignition. Seven low volume pulses of Freon 114B2 were injected before the pressurization of the fluid reservoir occurred. The first of the five high volume injection pulses occurred at approximately 160,000 ft. and the fluid was expended at approximately 88,000 ft. The telemetry records of the pressure build-up and the output of the linear displacement transducer monitoring the piston movement in the cylinder are presented in Fig. 48. As previously described, the valves in the low-flow-rate branch and the high-flow-rate branch of the injection system were opened consecutively for 250 msec. The outputs of the pressure sensors monitoring the injection nozzles show that the pressure build-up did not occur at the start of the valve opening. During the first three injection pulses the waveform from the pressure sensor at the low-flow-rate nozzles showed a very gradual increase in pressure when the valve was open. Also the pressure increase at the high-flow-rate nozzles exhibited a considerable delay which is evident from the width of the output waveforms when compared with the 250 msec duration when the valves were open. This suggests that a considerable boil-off of the liquid trapped in the tubing between the valves and the nozzles occurred during periods when the valves were shut. Therefore each time the valves opened the tubing had to be refilled before the pressure at the nozzles reached the steady state level. As the pressure on the liquid in the reservoir increased the tubing was refilled faster, as indicated by the wider pressure pulses in the TM records. This boil-off process, which may be regarded as a continuous low volume injection, must be considered when viewing the data obtained from the microwave experiments and the electrostatic probes.

The reproduction of the A21.011-1 flight telemetry records obtained from the test signal reflectometer, the mutual coupling instrument and the TM reflectometer are shown in Fig. 49. Pressurization of the liquid in the reservoir is marked by letter P. The staircase waveform indicates the injection sequence. The low level signifies the period when both of the solenoid valves were closed, the middle step shows when the low-flow-rate valve was open and the upper step indicates the high-flow-rate valve operation. Since the incident power of the telemetry and the test signals were relatively constant throughout the reentry period, the records of these two signals are not shown.

Isolation of all four telemetry antennas on this flight produced a relatively simple reflected power pattern. The records show the familiar cyclic variation due to the non-zero angle of attack of the reentering and rotating

nose cone. It should be noted that the reflected power returned to the free-space condition during each rotation period indicating lower plasma density than usual. Also there appeared a secondary increase in the reflected power on the side of the main cycle when in general the reflection was decreasing. This particular portion of the cycle was very susceptible to the injection of the liquid. Even during the first low-flow-rate injection pulse after the pressurization, this secondary reflection was drastically reduced and remained near free-space level for the rest of the reentry period. The main reflection cycle does not appear to have been altered by the injection.

The alleviant significantly affected the mutual coupling between the two test antennas, while the influence on the reflected power was not as pronounced. The high volume injection considerably increased the lower levels of the coupled power in each cycle, but the higher levels were less affected. Also the small secondary changes modifying the main coupled power cycle before pressurization of the liquid, became more visible after the pressure was applied. Eventually, as the reentry progressed, the coupled power started varying at twice the spin rate of the nose cone. Similar occurrences of the double frequency may be observed in the waveforms obtained from the four probe field meter shown in Fig. 50. The effects of the alleviant on the amplitudes of the waveforms, which depend not only on the phase but also on the magnitude of the reflected waves are clearly visible in the display. Unfortunately the phase variation of the reflected wave can not be shown without further data reduction.

The electrostatic probe data for vehicle A21.011-1 is displayed in Fig.'s 51-53. Fig.'s 51a and b present the probe current data for the two $S/R = 4.4$ electron collecting fixed bias probes located at $\theta = 52.5^\circ$ and $\theta = 142.5^\circ$ respectively (refer to Table II for locations). The reaction of both probes to the low-flow-rate injection pulses of Freon 114B2 can be seen up until 412.2 seconds. The injected pulses of alleviant cause severe reduction in probe currents on the leeward side of the vehicle. The probe located below the injection nozzle (Fig. 51) has a large and a continuous reduction in probe current. The probe located 90° away shows a distinctive reaction to each injection pulse. The high-flow-rate injection pulses start at 412.2 seconds, causing both probes to have their leeward side currents reduced almost continuously.

Fig. 51c displays the probe current data for the electron collecting fixed bias probe located at $S/R = 2.4$. Again the effects of both the low and the high-flow-rate injection pulses can be seen. Due to the previously discussed decommutator problem the upper side of the data envelope was deter-

mined from other records and is shown with a dashed line.

Two variable bias electrostatic probes were located between the two test antennas directly below the injection nozzles. One probe collected electrons (Fig. 52) and the other collected positive ions (Fig. 53). The electron collecting probe currents were severely reduced by the injected alleviant, especially at the 5 V bias level. The positive ion collecting probe currents were reduced to some extent and the 5 V level data was delayed in a manner similar to that of the previous flight. The large reduction in electron current was expected because of the electrophilic fluid injected into the flow field. The electrons in the plasma became attached to the molecules of the injected fluid causing a decrease in the free electron density with no appreciable decrease in the ion density. The positive ion current is reduced to some extent through recombination of positive ions with electrons on the surface of the injectant droplets. At no time was there sufficient injectant introduced to cool the plasma and thereby reduce the ion density.

ACKNOWLEDGEMENT

The authors wish to acknowledge the splendid cooperation and the support given by the personnel of AFCRL in preparation of the experiments. Special recognition must be extended to R. Walters who directed the mechanical design and to Major L. Maloney and J. L. Poirier who coordinated the joint effort.

BIBLIOGRAPHY

1. Rotman, W., "Microwave Measurements of Flow Field Characteristics at the Stagnation Point of a Blunt Reentry Body", presented at the AIAA 5th Fluid and Plasma Dynamics Conference, Boston, Massachusetts. June 1972.
2. Ryback, J. P., "Causes, Effects and Diagnostic Measurements of the Reentry Plasma Sheath", Scientific Report No. 1, Contract No. F19628-70-C-0035, Department of Electrical Engineering, Colorado State University, Fort Collins, Colorado. December 1970.
3. Rotman, W., "Studies of Reentry Plasma Sheath Effects Upon Antenna Performance", presented at the Symposium on the Entry Plasma Sheath and Its Effects on Space Vehicle Electromagnetic Systems (4th Plasma Sheath Symposium), NASA Langley Research Center, Hampton, Virginia. October 1970.
4. Poirier, L. J., Rotman, W., Hayes, D. T., and Lennon, J. F., "Effects of the Reentry Plasma Sheath on Microwave Antenna Performance: Trailblazer II Rocket Results of 18 June 1967", Report No. AFCRL-69-0354, U. S. Air Force Cambridge Research Laboratories. August 1969.
5. Rotman, W., "Trailblazer II Rocket Tests of the Effects of Reentry Plasma Sheaths Upon Microwave Antenna Performance", presented at the Symposium on the USAF Antenna Research and Development (7th Annual Symposium), University of Illinois, Urbana, Illinois. November 1967.
6. Huber, P. W. and Sims, T., "Research Approaches to the Problem of Reentry Communications Blackout", Proceedings of the Third Symposium on the Plasma Sheath-Plasma Electromagnetics of Hypersonic Flight; Vol. II: Electrical Properties of Shock-Ionized Flow Fields, Report No. AFCRL-67-0280 (vol. II)' Special Report No. 64 (II), U. S. Air Force Cambridge Research Laboratories. May 1967.
7. Huber, P. W. and Sims, T., "The Entry-Communications Problem", Astronautics and Aeronautics; Vol. 2, No. 10, October 1964.

8. Aisenberg, S. and Pung, N. H., "A Theoretical and Experimental Study of the Basic Properties of Plasmas", Final Report, AFCRL-71-0018, Contract No. F19628-68-C-0127, Whittaker Corporation, Space Sciences Division, Waltham, Massachusetts. November 1970.
9. Aisenberg, S. and Chang, K. W., "Chemical Additives and Diagnostics for High Temperature Air Plasmas", Final Report, AFCRL-72-0354, Contract No. F19628-71-C-0077, Whittaker Corporation, Space Sciences Division, Waltham, Massachusetts. November 1971.
10. Mukaihata, T., Bottjer, M. F., and Tondreau, H. J., "Rapid Broad-Band Directional Coupler Directivity Measurements", IRE Transactions on Instrumentation, Vols. 1-9, No. 2, September 1960.
11. Adam, S. F., "Microwave Theory and Applications", Prentice-Hall Inc., 1969.
12. Caldecott, R., "Multiprobe Reflectometer and its Applications to Automated Transmission Line Measurements", submitted for publication in the IEEE Transactions for G-AP, July, 1972.
13. Bohley, P., Caldecott, R., McGown, R., and Taylor, R. C., "Measuring Missile Antenna Impedance in Flight", Electronics, 36, No. 28, July 12, 1963.
14. Hayes, D. T., "Electrostatic Probe Measurements of Flow Field Characteristics of a Blunt Body Reentry Vehicle", presented at the AIAA 5th Fluid and Plasma Dynamics Conference, Boston, Massachusetts. June 1972.
15. Karas, N. V., "Microstrip Plasma Probe", Report No. AFCRL-72-0417, U. S. Air Force Cambridge Research Laboratories. July 1972.
16. Hayes, D. T., Herskovitz, S. B., Lennon, J. F., Poirier, L. J., "Preliminary Report on the Trailblazer II Chemical Alleviation Flight of 28 July, 1972", Report in preparation, U. S. Air Force Cambridge Research Laboratories.
17. Haldeman, C. W. and Holmes, D. G., "Effect of an Alleviated Plasma

Boundary Layer on the Transmission of High Power Microwave Signals",
Final Report, AFCRL-71-0562, Contract No. F19628-69-C-0043,
Massachusetts Institute of Technology Aerophysics Laboratory,
Cambridge, Massachusetts. December 1971.

18. Jacavano, D. J. and Herskovitz, S. B., "Determination of Electron Quenchant Efficiencies Under Simulated Entry Condition", presented at the Symposium on the Entry Plasma Sheath and Its Effects on Space Vehicle Electromagnetic Systems (4th Plasma Sheath Symposium), NASA Langley Research Center, Hampton, Virginia. October 1970.
19. "Aerospace Telemetry Standards" MIL-STD-442B, 1 December 1967.
20. Stiltz, H. L., "Aerospace Telemetry", Prentice-Hall, Inc., 1963.

PERSONNEL

A list of the engineers and technicians who contributed to the work reported is given below:

J. Spencer Rochefort, Professor of Electrical Engineering, Principal Investigator.

Raimundas Sukys, Senior Research Associate, Engineer.

Ronald Symmes, Research Assistant, Engineer.

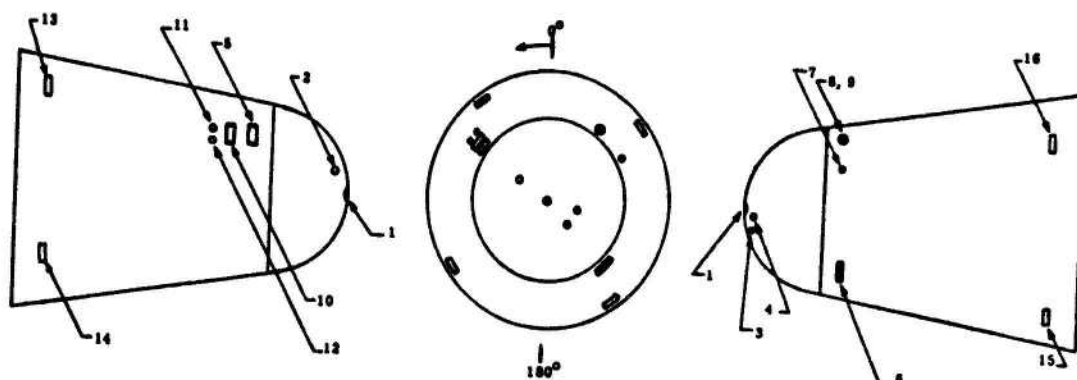
William M. Thompson, Technician, Electrical Engineering.

RELATED CONTRACTS AND PUBLICATIONS

AF19(604)-3506	1 April 1958 through 30 June 1963
AF19(628)-2433	1 April 1963 through 31 March 1967
AF19(628)-5110	1 September 1965 through 28 February 1969
F19628-69-C-0150	1 March 1965 through 31 August 1972
F19628-72-C-0050	16 August 1971 through present

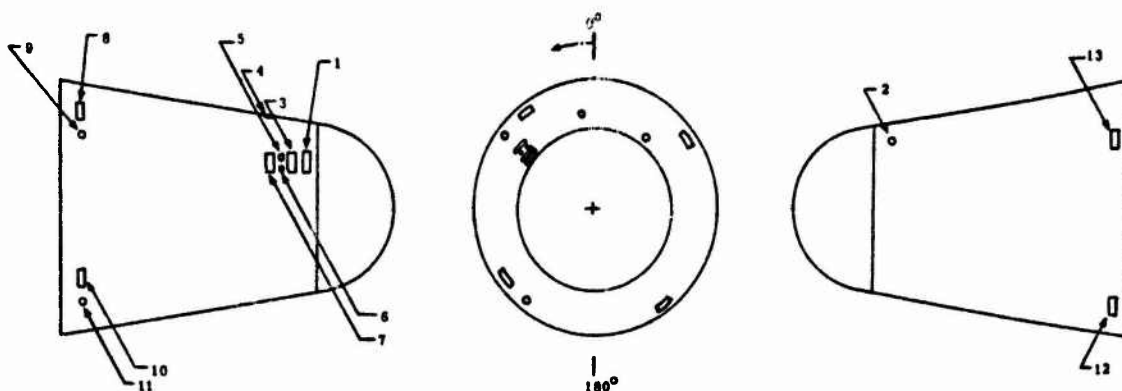
J. S. Rochefort, L. J. O'Connor, C. H. Price, Jr., and R. Sukys, "Data Transmission and Trajectory Determining Devices For Research Rockets and Satellites", Final Report, Contract No. AF19(604)-3506, 30 June 1963.

J. S. Rochefort, L. J. O'Connor, R. Sukys and A. Glazer, "Data Transmission and Instrumentation Systems for Space Vehicles", Final Report. Contract No. AF19(628)-2433, 30 April 1967.



No	Device		S/R	θ
1	Electrostatic probe.	Fixed negative bias.	0	NA
2	Electrostatic probe.	Switchable negative bias.	.475	52.5°
3	Thermocouple.	ES probe temperature.	.475	232.5°
4	Thermocouple.	Skin temperature.	.475	258.5°
5	Test antenna.	Transmitting.	1.84	52.5°
6	Stripline probe.		1.84	223.5°
7	Thermocouple.	Skin temperature.	1.84	300.5°
8	Conductivity probe.		1.34	322.5°
9	Thermocouple.	In conductivity probe.	1.34	322.5°
10	Test antenna.	Receiving.	2.30	52.5°
11	Electrostatic probe.	Fixed positive bias.	2.53	48.0°
12	Electrostatic probe.	Switchable negative bias.		57.0°
13	Telemetry antenna.			37.0°
14	Telemetry antenna.		4.35	127.0°
15	Telemetry antenna.		4.35	217.0°
16	Telemetry antenna.		4.35	307.0°

TABLE I. ANTENNA AND PROBE LOCATIONS. AD21.862



No	Device	S/R	θ
1	Injection nozzles.	1.77	52.5°
2	Electrostatic probe. Fixed negative bias.	1.77	322.5°
3	Test antenna. Transmitting.	2.09	52.5°
4	Electrostatic probe. Fixed positive bias.	2.4	7.5°
5	Electrostatic probe. Switchable positive bias.	2.4	48.0°
6	Electrostatic probe. Switchable negative bias.	2.4	57.0°
7	Test antenna. Receiving.	2.71	52.5°
8	Telemetry antenna.	4.4	37.0°
9	Electrostatic probe. Fixed positive bias.	4.4	52.5°
10	Telemetry antenna.	4.4	127.0°
11	Electrostatic probe. Fixed positive bias.	4.4	142.5°
12	Telemetry antenna.	4.4	217.0°
13	Telemetry antenna.	4.4	307.0°

TABLE II. ANTENNA AND PROBE LOCATIONS. A21.011-1

SUBCARRIERS

<u>Band</u>	<u>Center Frequency</u>	<u>Data</u>	<u>Description</u>
8	3.0 kHz	Positive ion current.	S/R = 0.
9	3.9 kHz	Reflected power.	Test antenna.
10	5.4 kHz	Coupled power.	High level signal.
11	7.35 kHz	Coupled power.	Low level signal.
12	10.5 kHz	Incident power.	Telemetry antenna.
13	14.5 kHz	Reflected power.	Telemetry antenna.
14	22.0 kHz	Coil 1 output.	Conductivity probe.
16	40.0 kHz	Coil 2 output.	Conductivity probe.
17	52.5 kHz	Positive ion current.	Switchable, S/R = .475
18	70.0 kHz	Positive ion current.	Switchable, S/R = 2.58
20	124.0 kHz	Commutator.	

COMMUTATOR

<u>Channels</u>	<u>Data</u>	<u>Description</u>
1	Zero data calibration.	
2	Full scale data calibration.	
3-11-18-26	Electron current.	S/R = 2.58.
4-12-19-27	Reflected power.	Stripline probe.
5-13-20-28	Transmitted power.	Stripline probe.
6-21	Temperature.	ES probe. S/R = .475.
7	Temperature.	Skin. S/R = .475.
8	Incident power.	Test antenna.
9	Vehicle motion.	50 G accelerometer.
10	Battery voltage.	Test supply.
14	Temperature.	Conductivity probe.
15	Temperature.	Skin. S/R = 1.84.
16	Incident power.	Stripline probe.
17	Battery voltage.	Telemetry supply.
22	Frequency change.	Conductivity probe.
23	Temperature.	Payload mounting plate.
24	Vehicle motion.	5 G accelerometer.
25	Temperature.	Inner surface of nose cone.

TABLE III. TELEMETRY CHANNEL ASSIGNMENT. AD21.862

SUBCARRIERS

<u>Band</u>	<u>Center Frequency</u>	<u>Data</u>	<u>Description</u>
9	3.9 kHz	Reflected power.	Telemetry antenna.
10	5.4 kHz	Coupled power.	Test antennas.
11	7.35 kHz	Reflected power.	Test antenna.
12	10.5 kHz	Probe 4 output.	Field meter.
13	14.5 kHz	Probe 3 output.	Field meter.
14	22.0 kHz	Probe 2 output.	Field meter.
16	40.0 kHz	Probe 1 output.	Field meter.
17	52.5 kHz	Electron current.	Commutated probes at S/R = 4.4.
18	70.0 kHz	Electron current.	Switchable. S/R = 2.4.
19	93.0 kHz	Positive ion current.	Switchable. S/R = 2.4.
20	124.0 kHz	Commutator	

COMMUTATOR

<u>Channels</u>	<u>Data</u>	<u>Description</u>
1	Zero data calibration.	
2	Full scale data calibration.	
3-11-18-26	Positive ion current.	S/R = 1.77.
4-12-19-27	Electron current.	S/R = 2.4.
5-13-22	Pressure.	Low rate injection nozzle.
6-14-23	Pressure.	Reservoir.
7-15-24	Pressure.	High rate injection nozzle.
8-16-25	Injected volume.	High altitude experiment.
9-17-28	Injected volume.	Low altitude experiment.
10	Vehicle motion.	50 G accelerometer.
20	Injection sequence monitor.	
21	Incident power.	Test antenna.

TABLE IV. TELEMETRY CHANNEL ASSIGNMENT. A21.011-1

Vehicle				
AD21.862			A21.011-1	
<u>Time From Lift-off (sec)</u>	<u>Altitude (ft)</u>	<u>Velocity (ft/sec)</u>	<u>Altitude (ft)</u>	<u>Velocity (ft/sec)</u>
403			307,494	16,116
404			292,050	16,136
405	305,058	17,823	276,580	16,166
406	287,420	17,859	261,071	16,195
407	269,750	17,899	245,532	16,214
408	252,048	17,930	229,978	16,226
409	234,814	17,965	214,406	16,235
410	216,547	17,965	198,816	16,240
411	189,913	17,940	183,224	16,219
412	181,529	17,880	167,670	16,137
413	164,545	17,800	152,203	15,008
414	148,683	17,500	136,896	15,764
415			121,906	15,298
416			107,504	14,489
417			94,089	13,186
418			82,185	11,342
419			72,230	9,184
420			64,320	7,096

TABLE V. REENTRY PARAMETERS

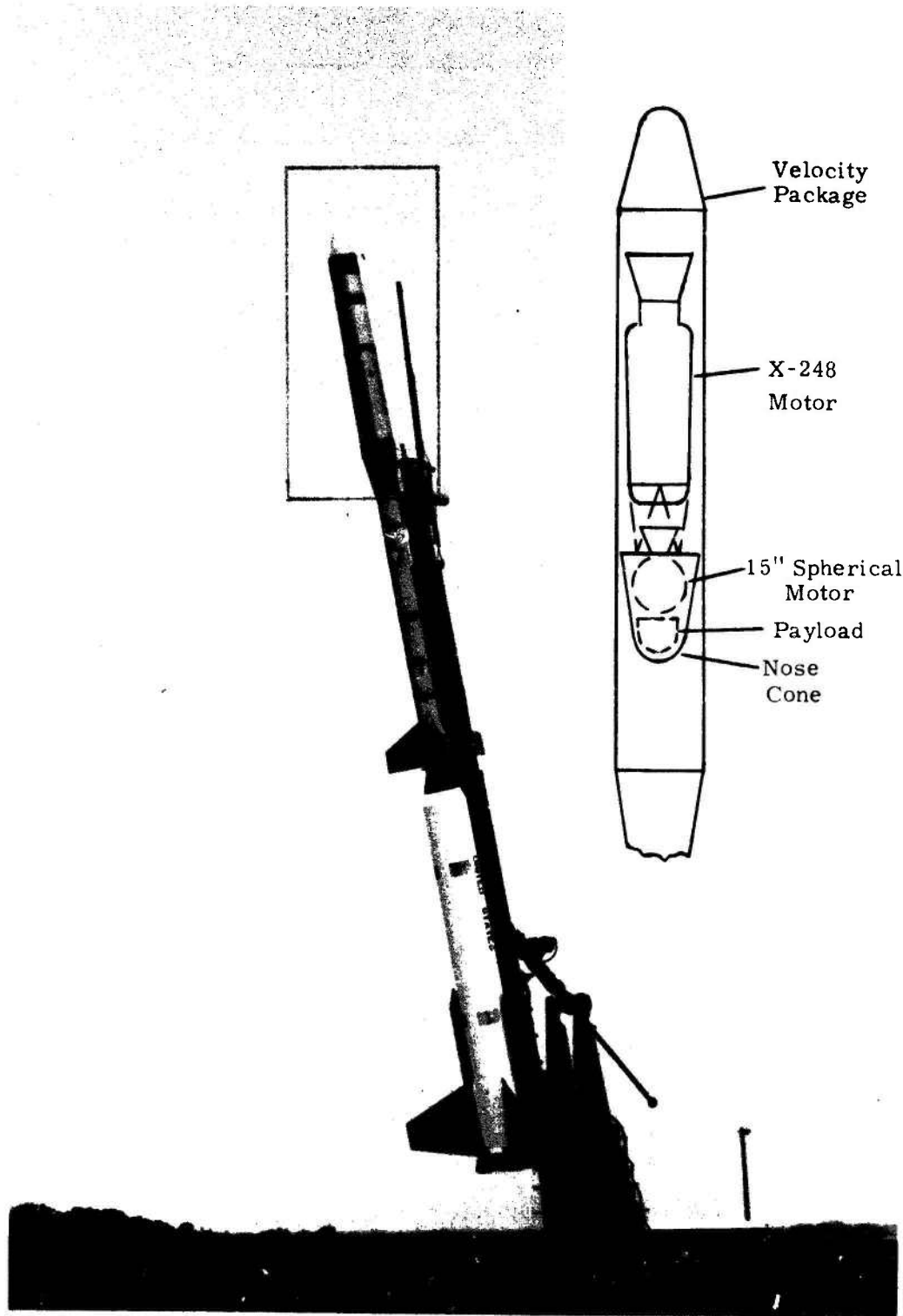


Fig. 1 TRAILBLAZER II ROCKET

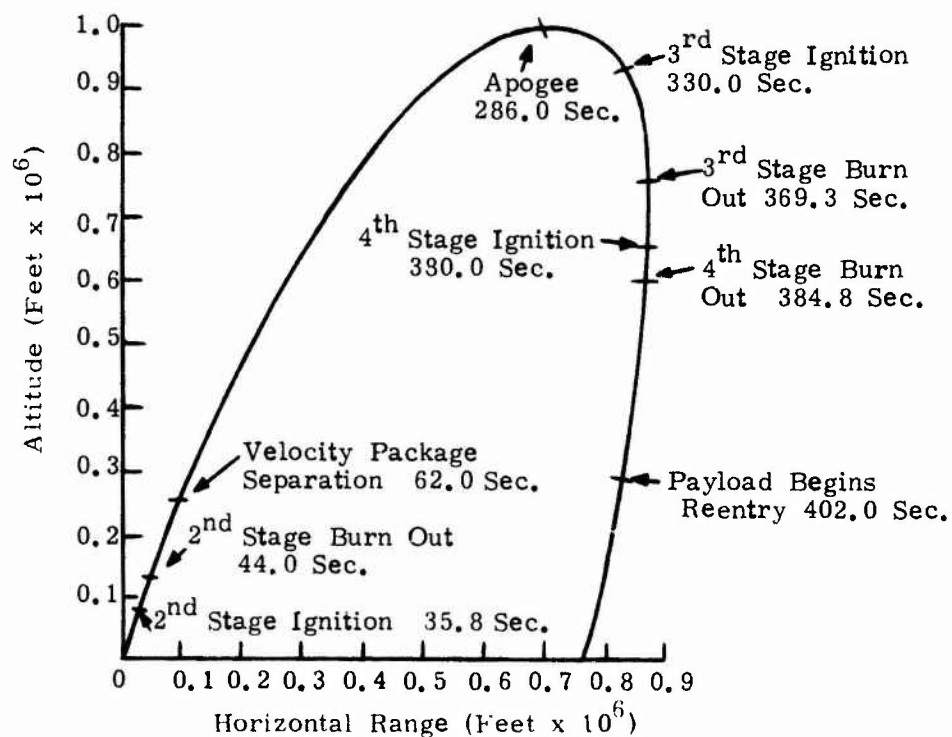


Fig. 2 TRAJECTORY AND STAGING

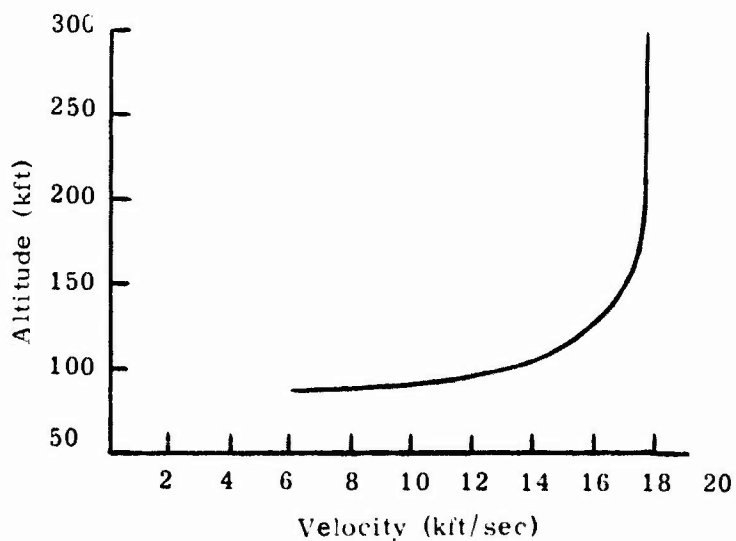


Fig. 3 REENTRY VELOCITY

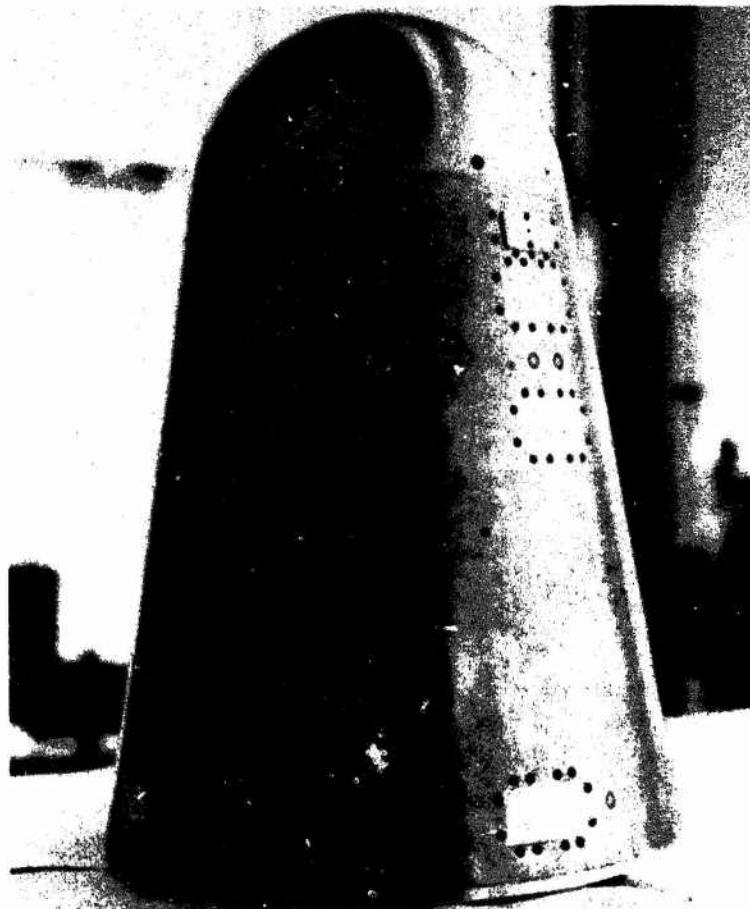


Fig. 4 NOSE CONE A21.011-1

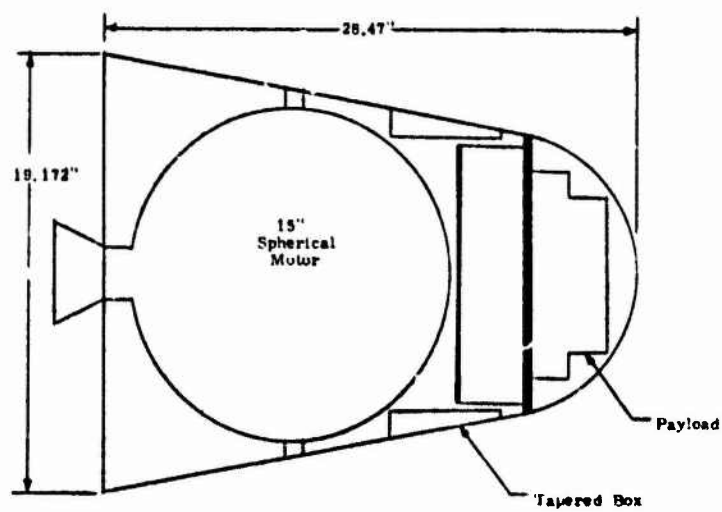


Fig. 5 NOSE CONE CONFIGURATION

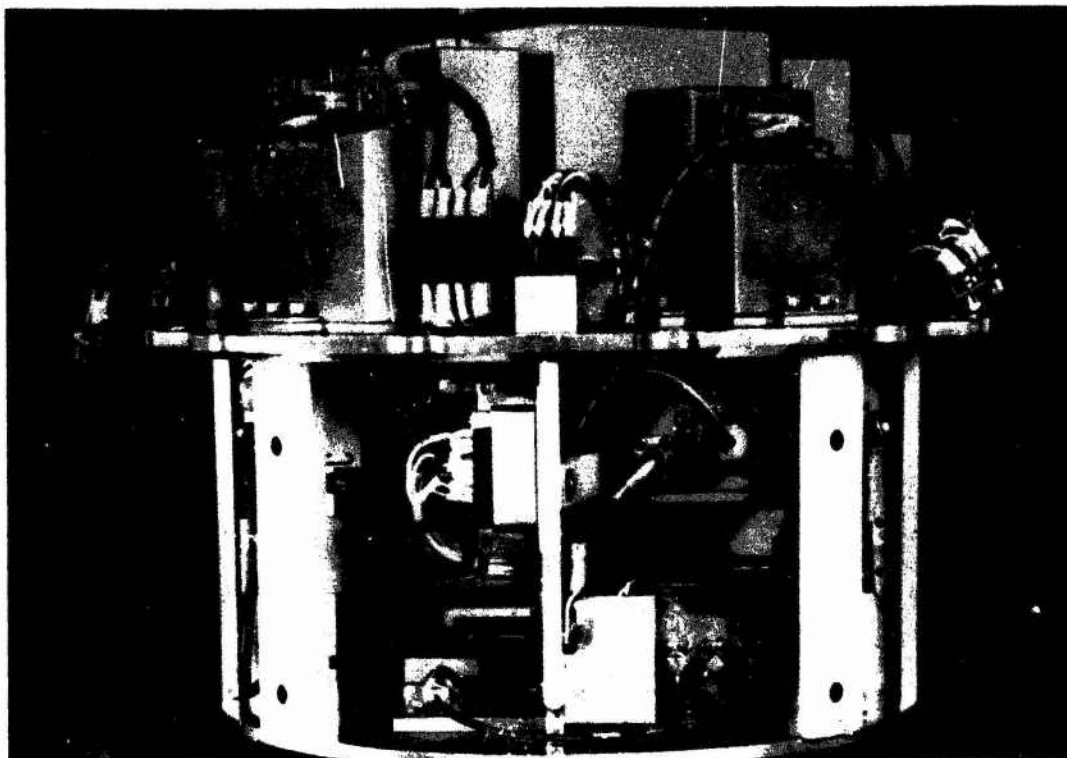


Fig. 6 FORWARD SECTION OF A21.011-1 PAYLOAD

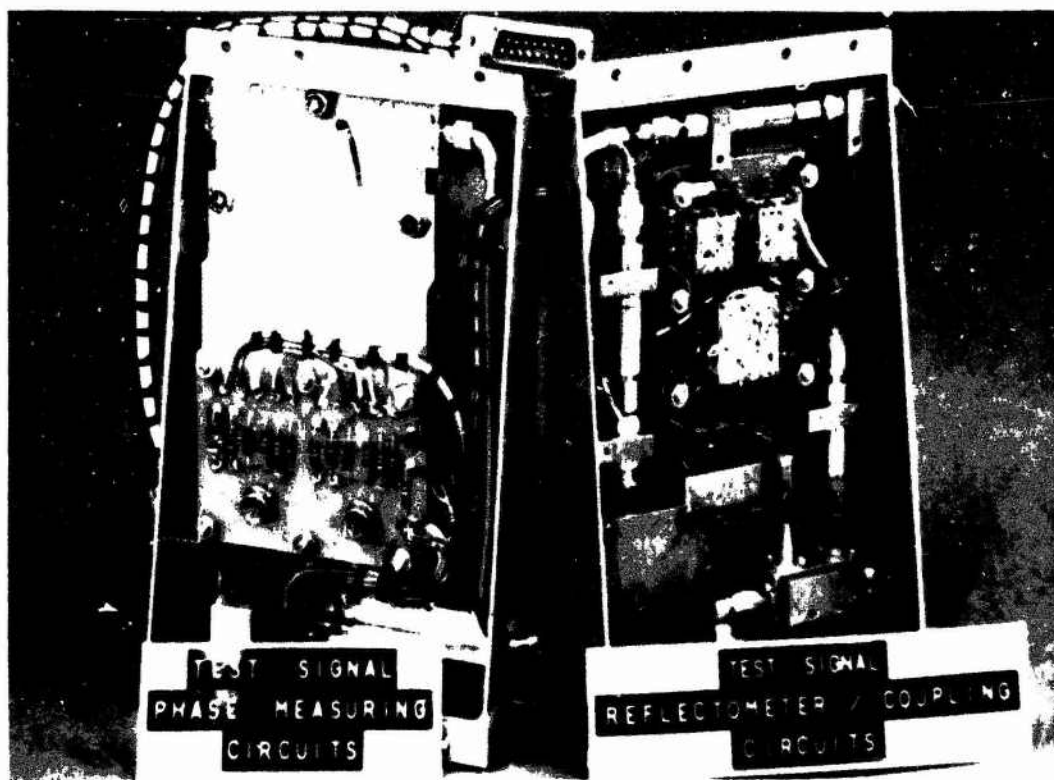


Fig. 7 TAPERED BOXES

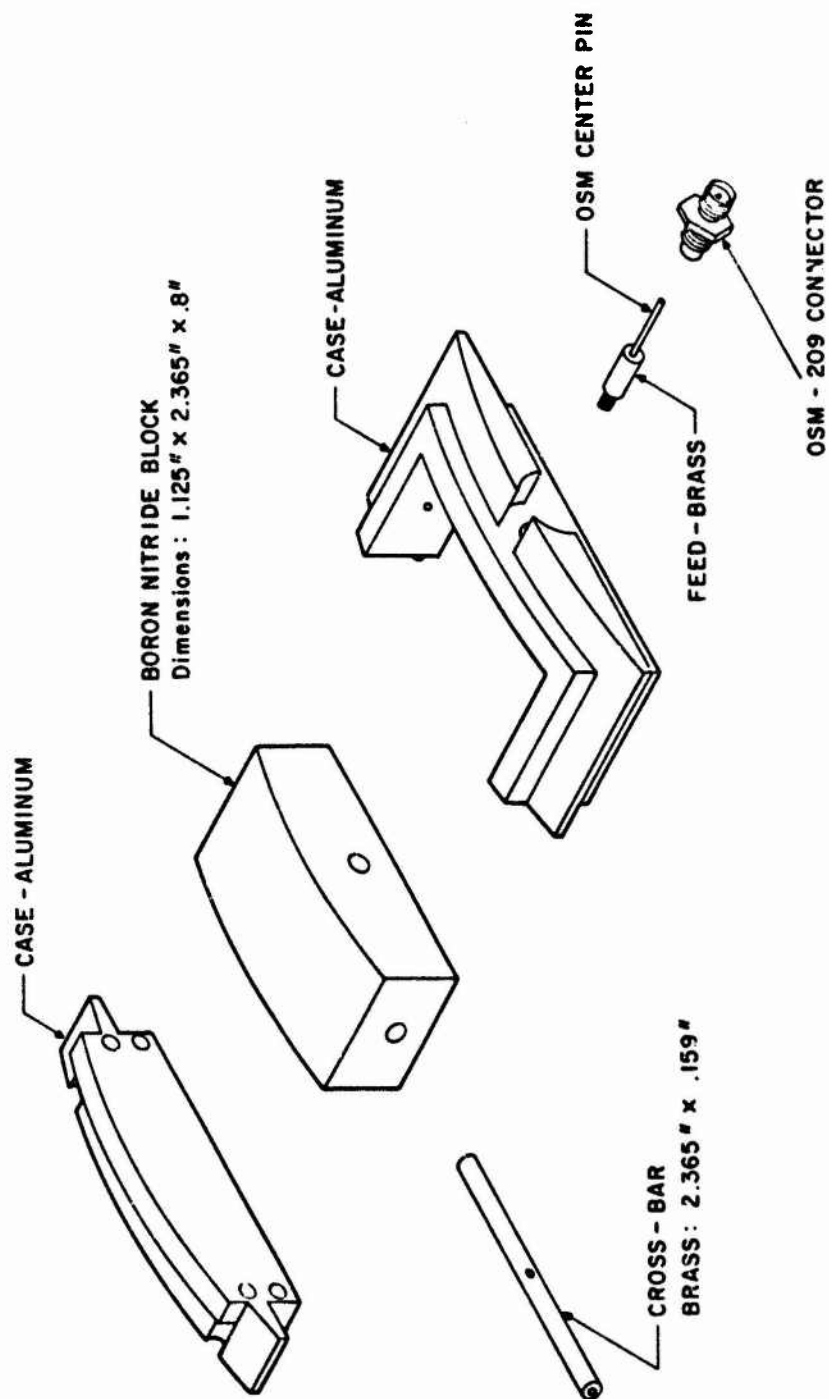


Fig. 8 TEST ANTENNA

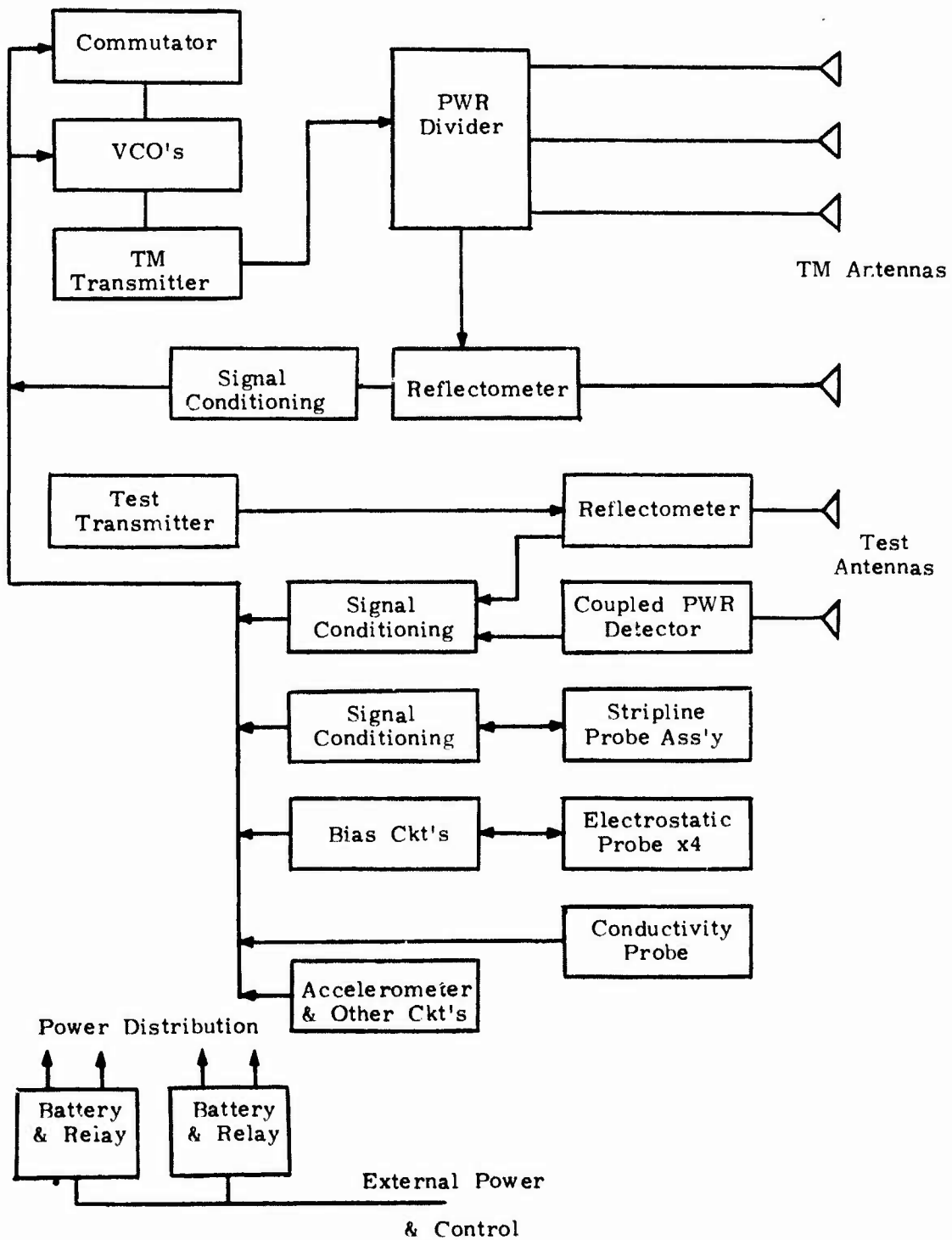


Fig. 9 BLOCK DIAGRAM OF AD21.862 INSTRUMENTATION

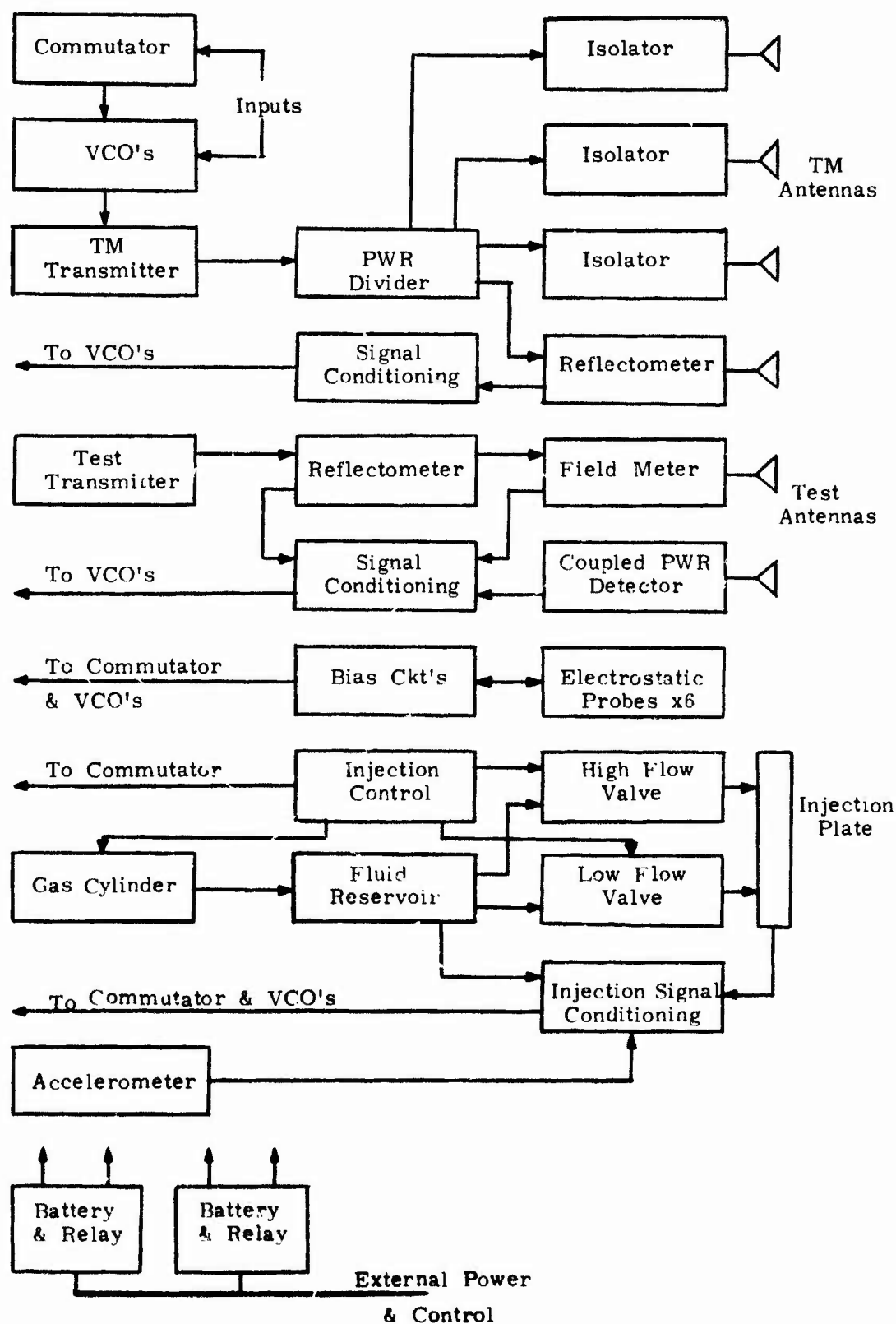


Fig. 10 BLOCK DIAGRAM OF A21.011-1 INSTRUMENTATION

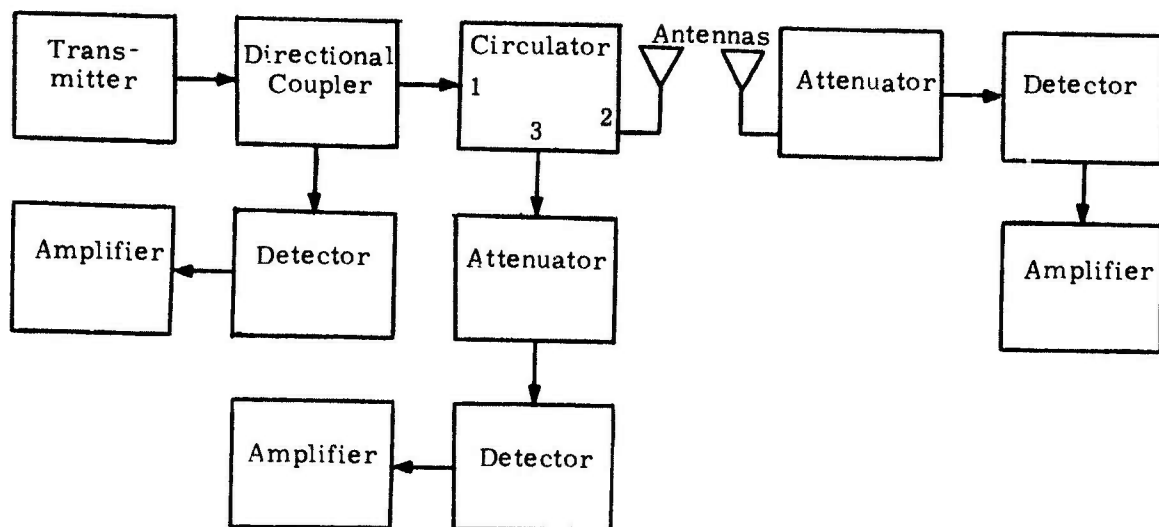


Fig. 11 S-BAND EXPERIMENT BLOCK DIAGRAM

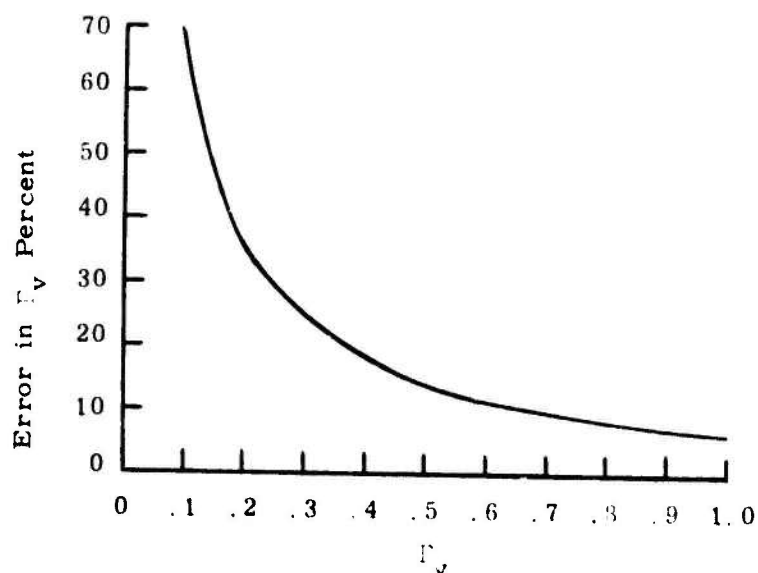


Fig. 12 ERROR IN MEASURED REFLECTION COEFFICIENT

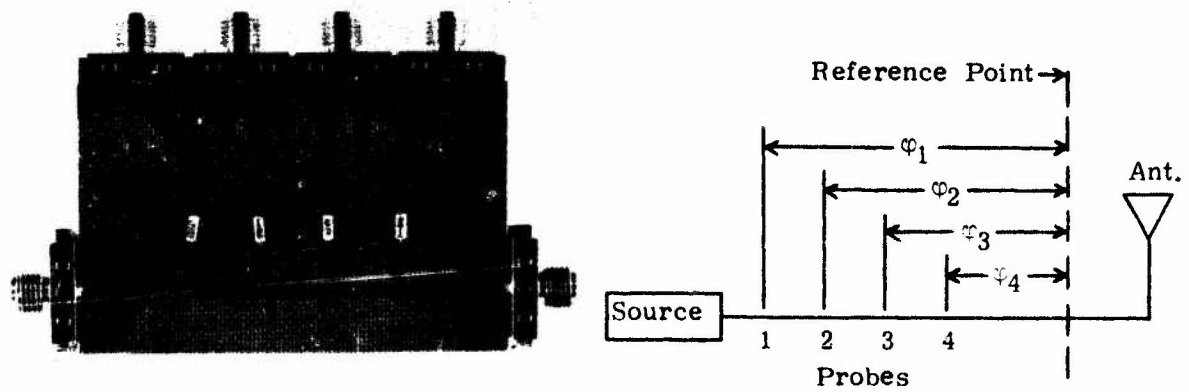


FIG. 13 FOUR PROBE FIELD METER

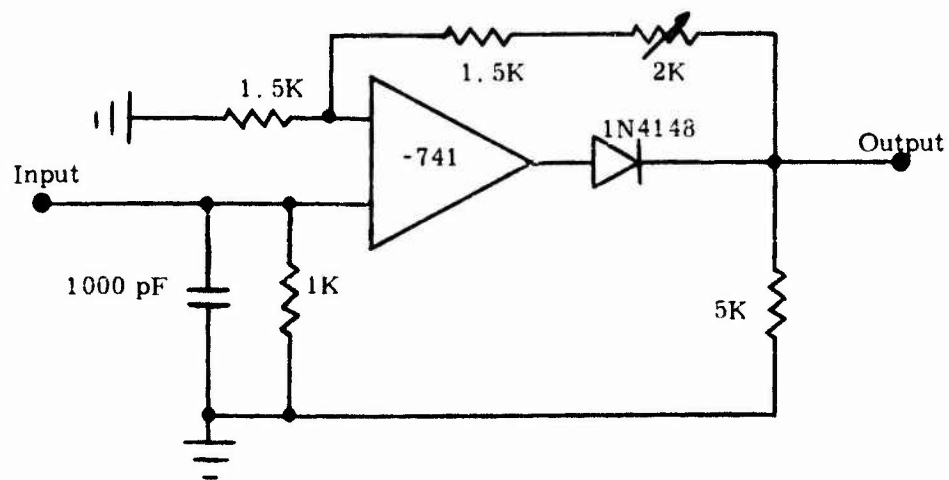


Fig. 14 PROBE SIGNAL AMPLIFIER

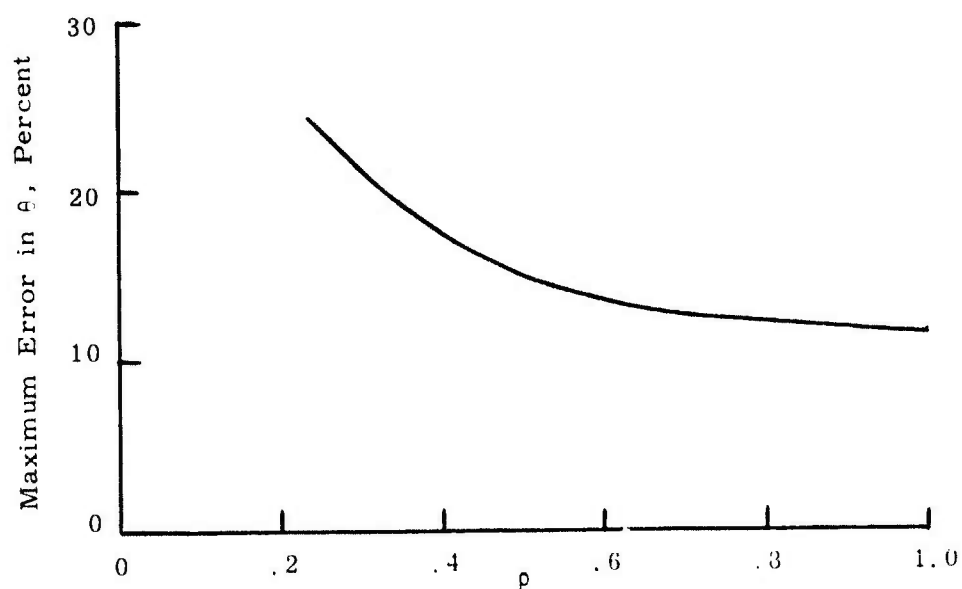


Fig. 15 ERROR IN MEASURED PHASE ANGLE

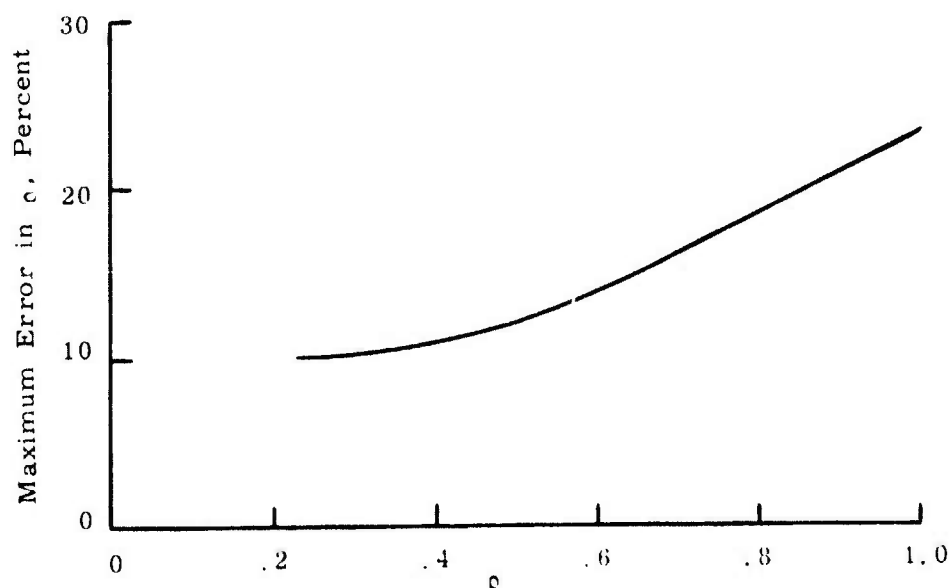


Fig. 16 ERROR IN MEASURED MAGNITUDE OF REFLECTION COEFFICIENT

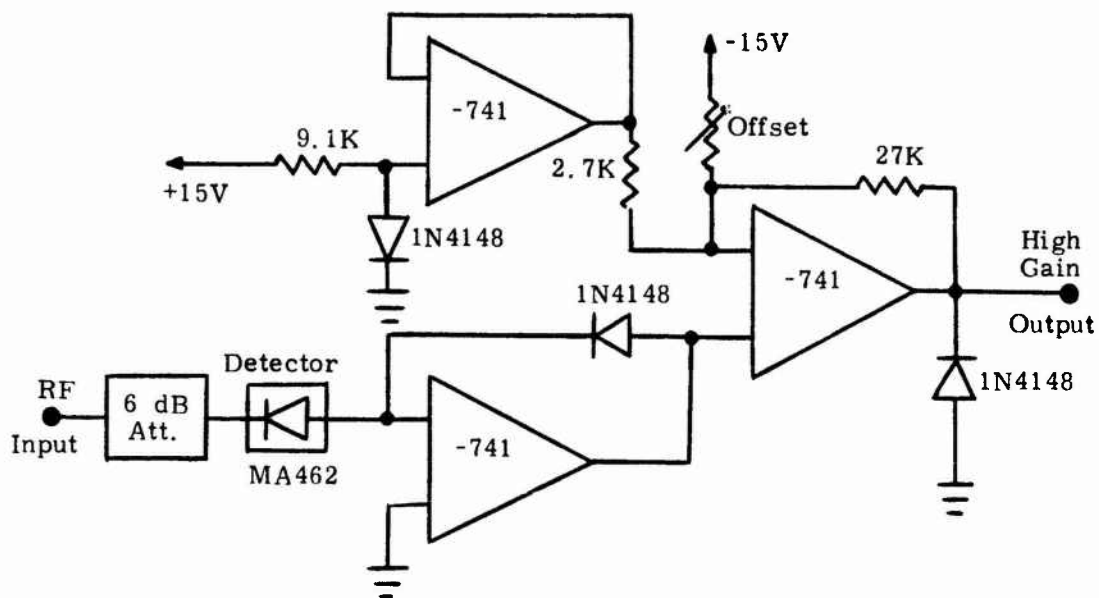


Fig. 17 COUPLED SIGNAL AMPLIFIER

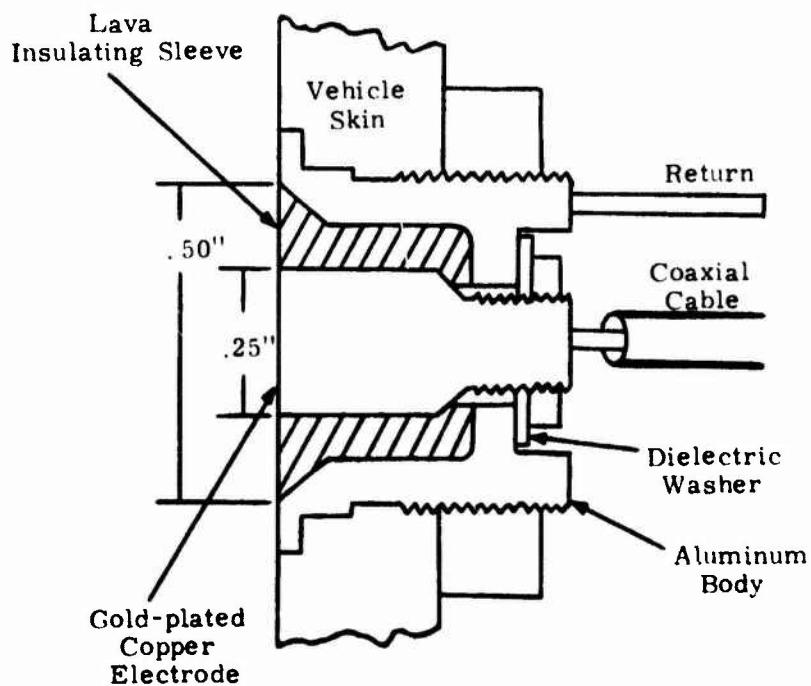


Fig. 18 FLUSHMOUNTED ELECTROSTATIC PROBE CONFIGURATION

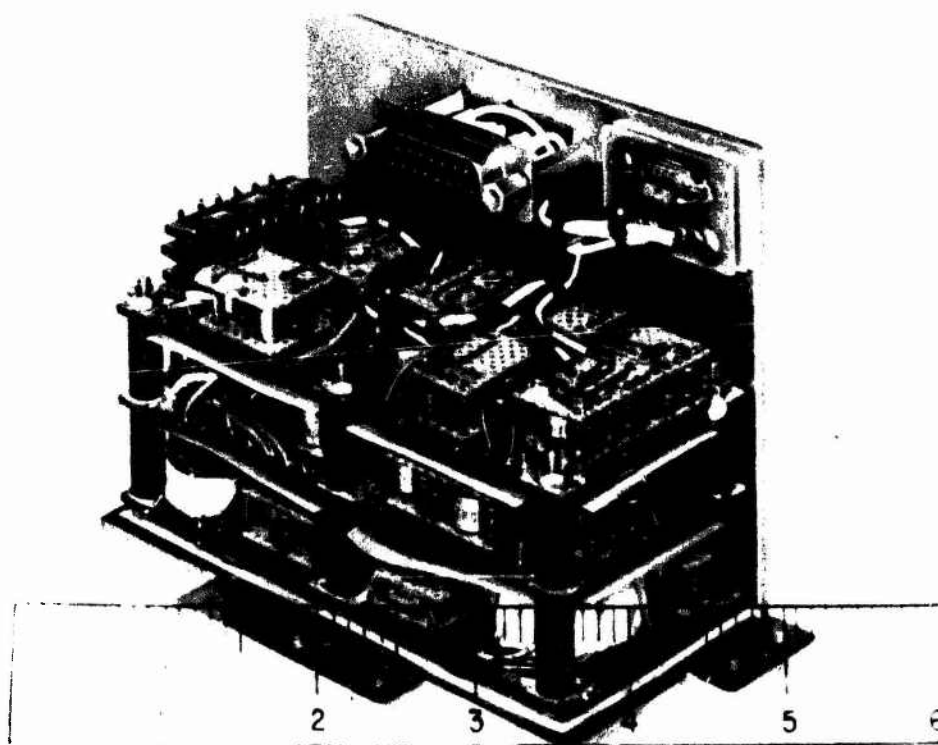


Fig. 19 DUAL ELECTROSTATIC PROBE ELECTRONICS

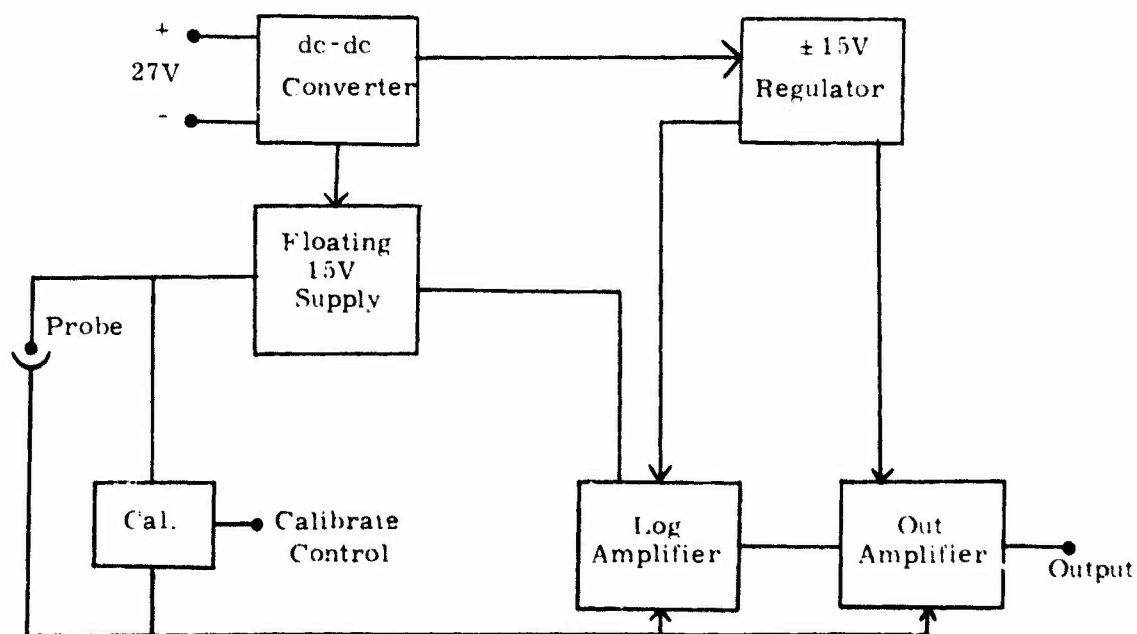


Fig. 20 FIXED BIAS ELECTROSTATIC PROBE

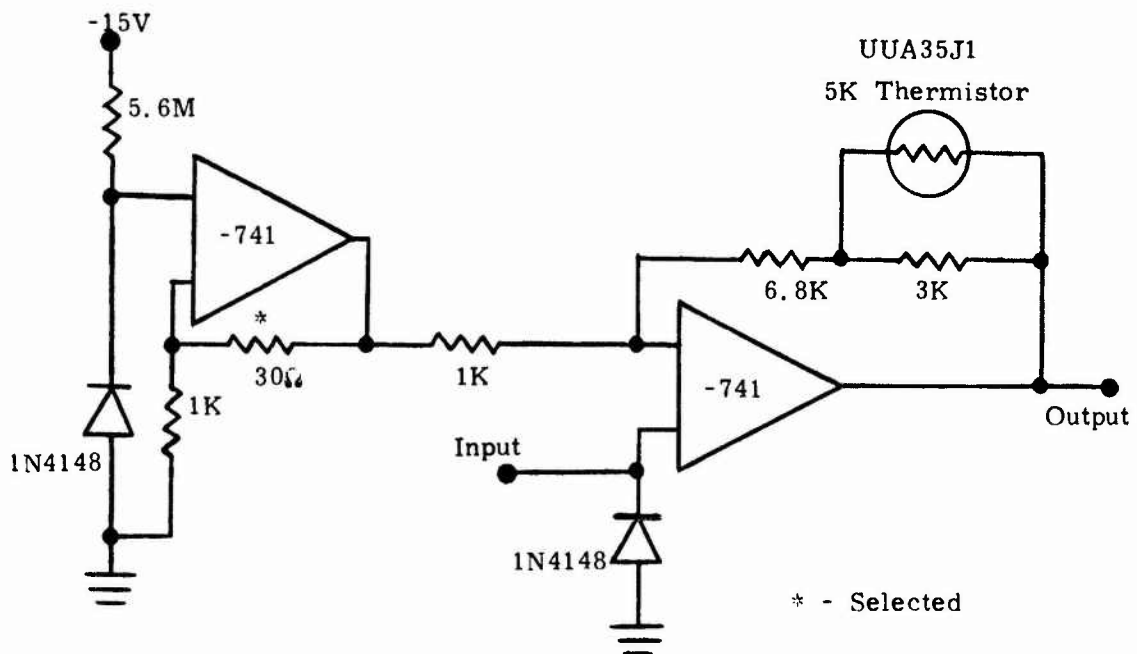


Fig. 21 LOG AMPLIFIER

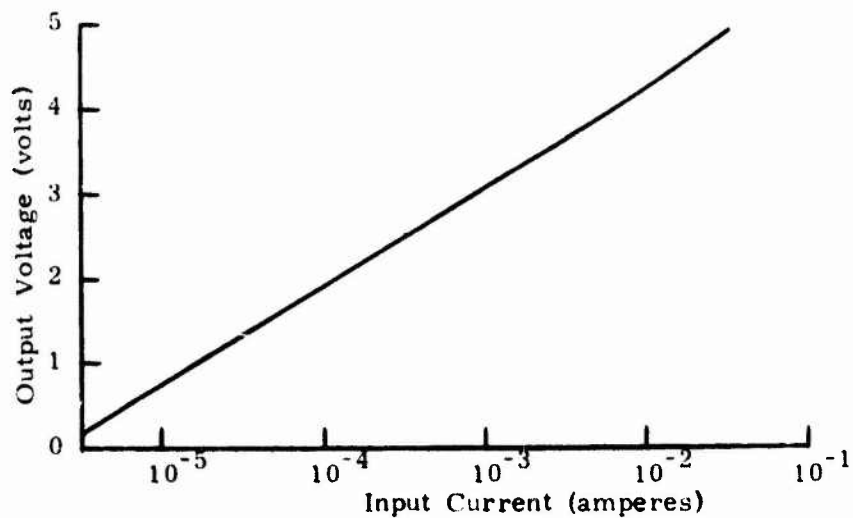


Fig. 22 TYPICAL LOG AMPLIFIER CHARACTERISTIC

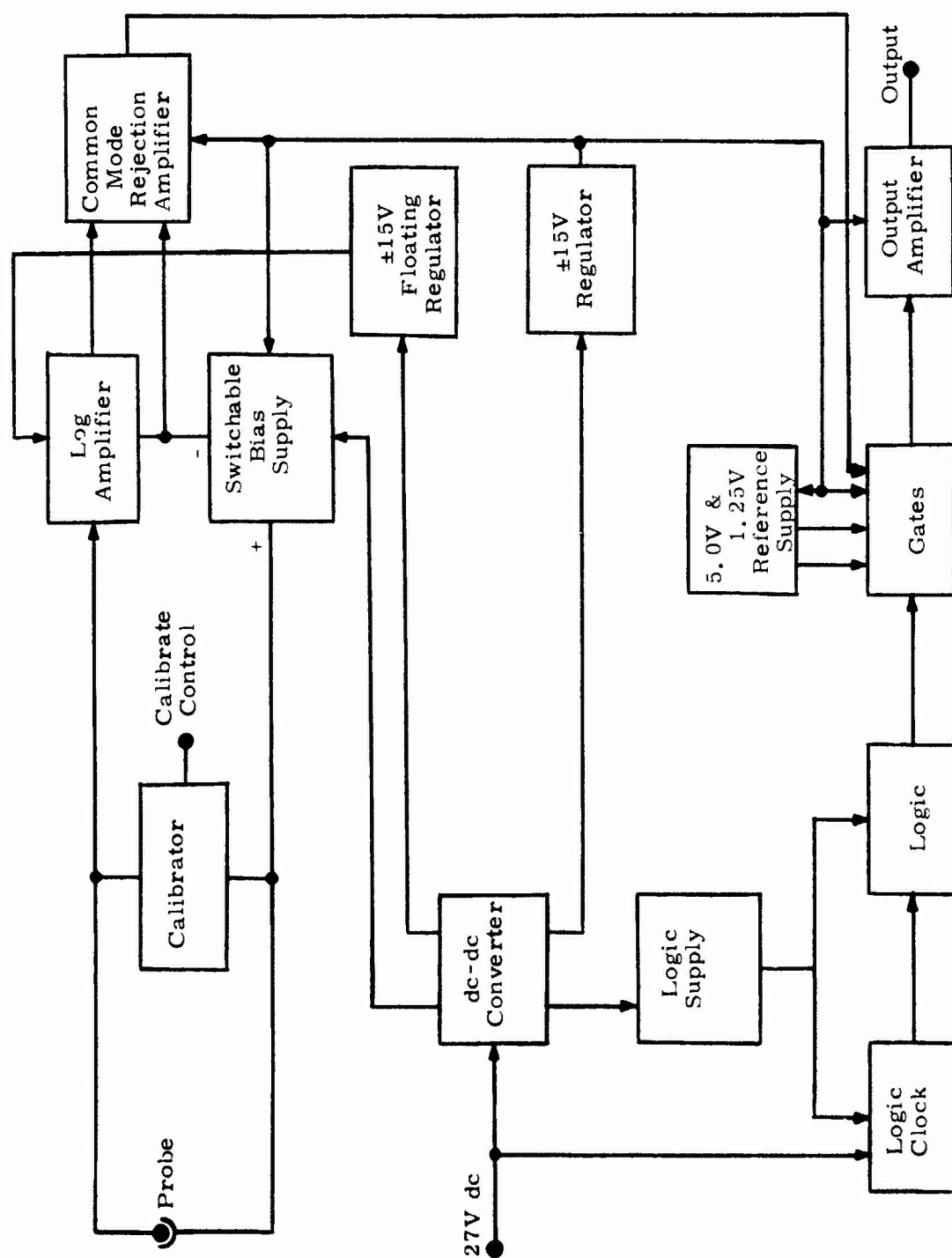


Fig. 23 VARIABLE BIAS ELECTROSTATIC PROBE

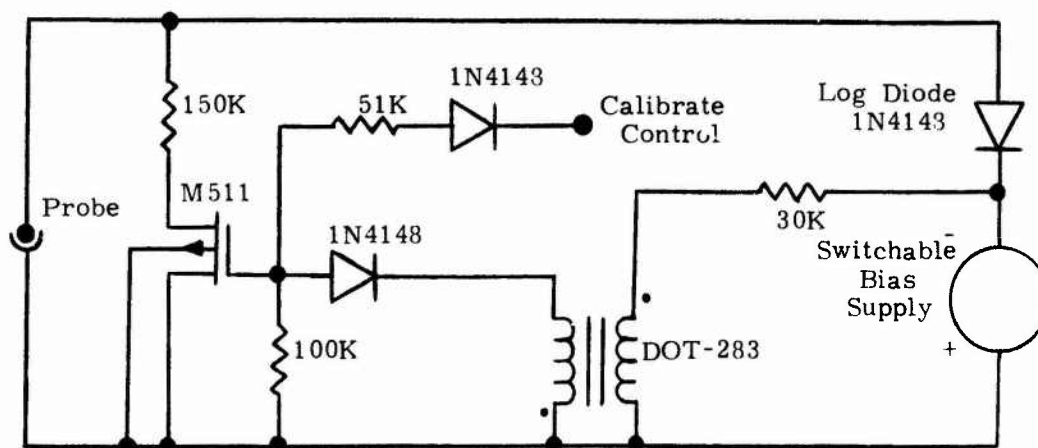


Fig. 24 STEADY STATE RESTORATION CIRCUIT

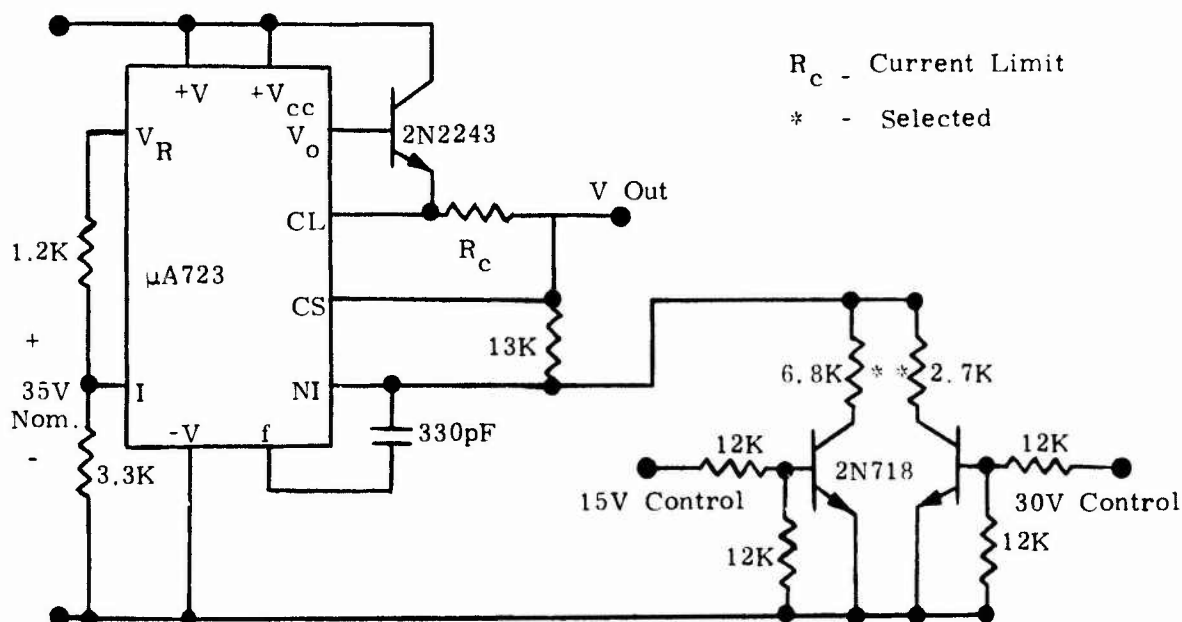


Fig. 25 SWITCHABLE POSITIVE VOLTAGE REGULATOR

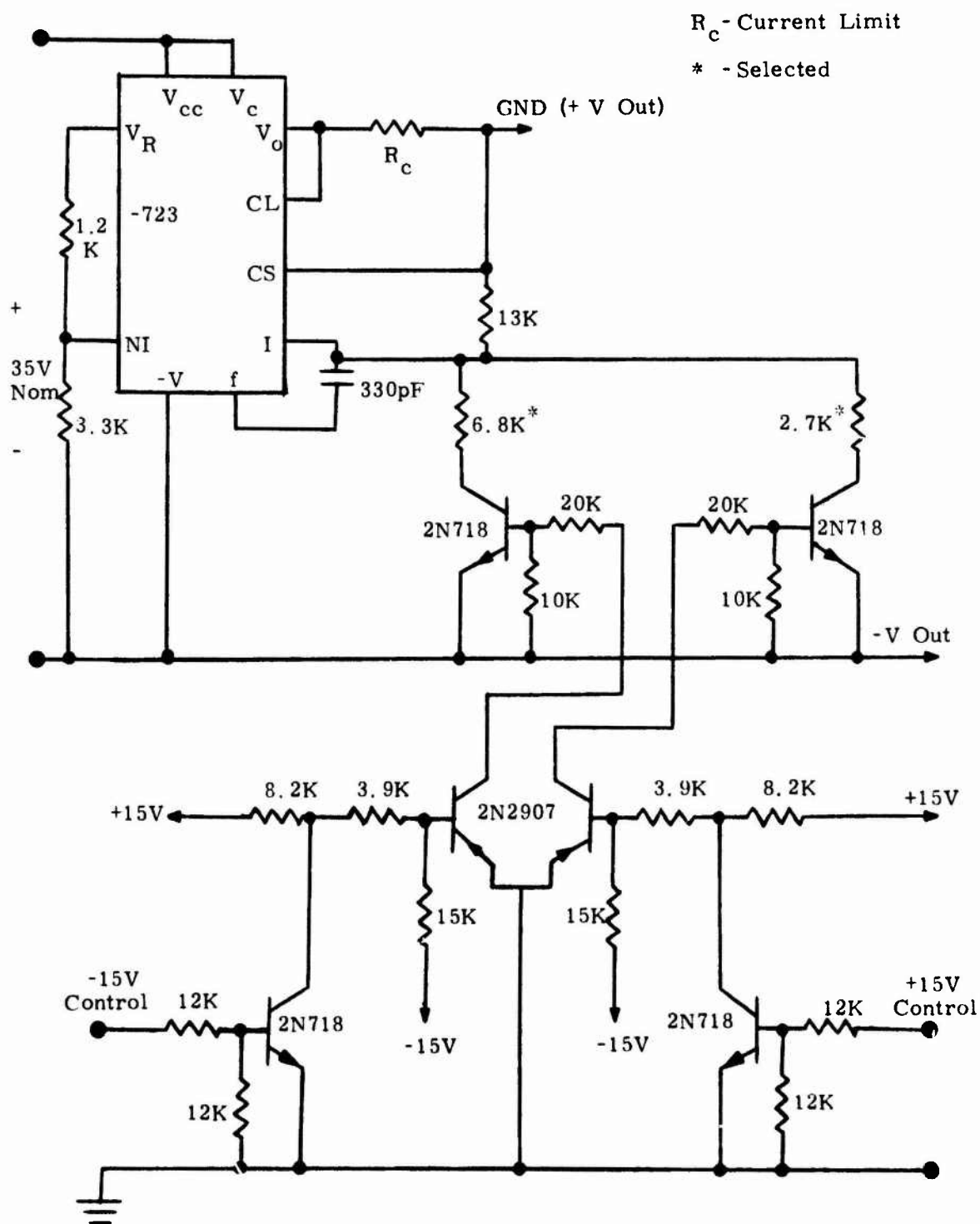


Fig. 26 SWITCHABLE NEGATIVE VOLTAGE REGULATOR

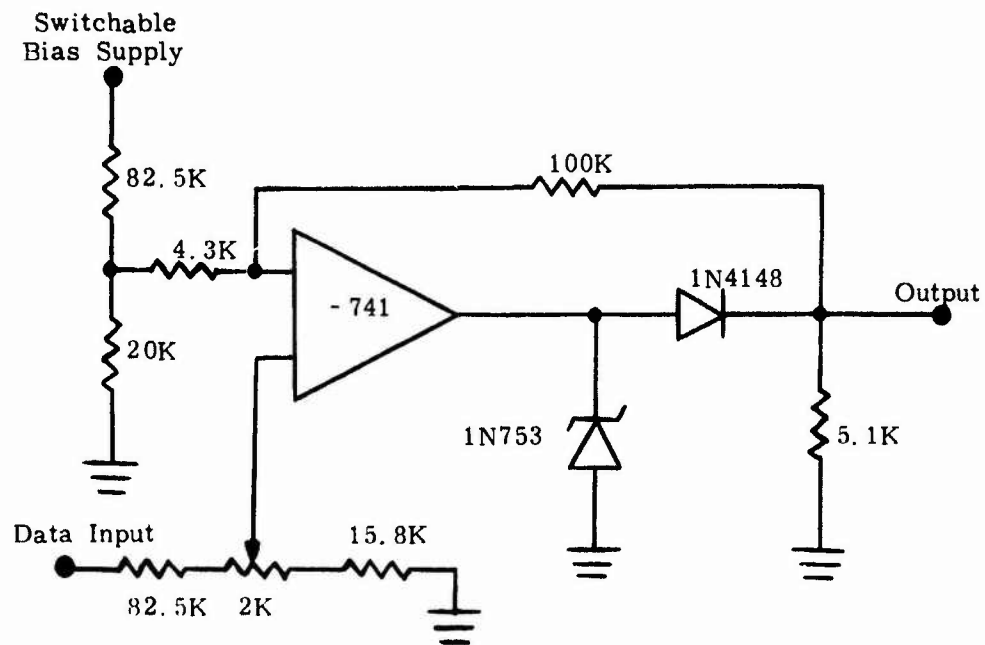


Fig. 27 COMMON MODE REJECTION CIRCUIT

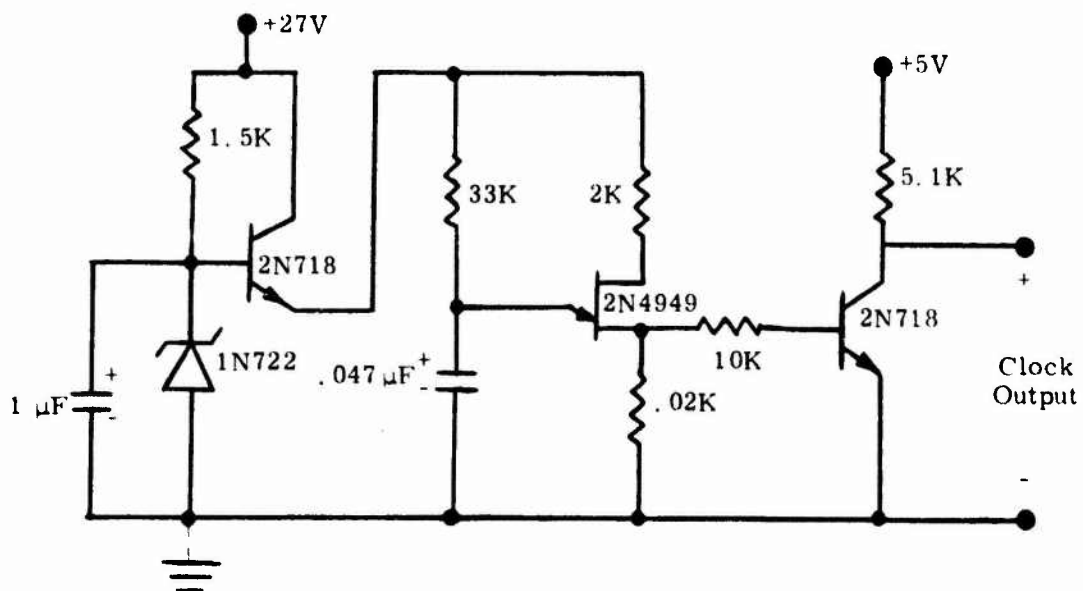
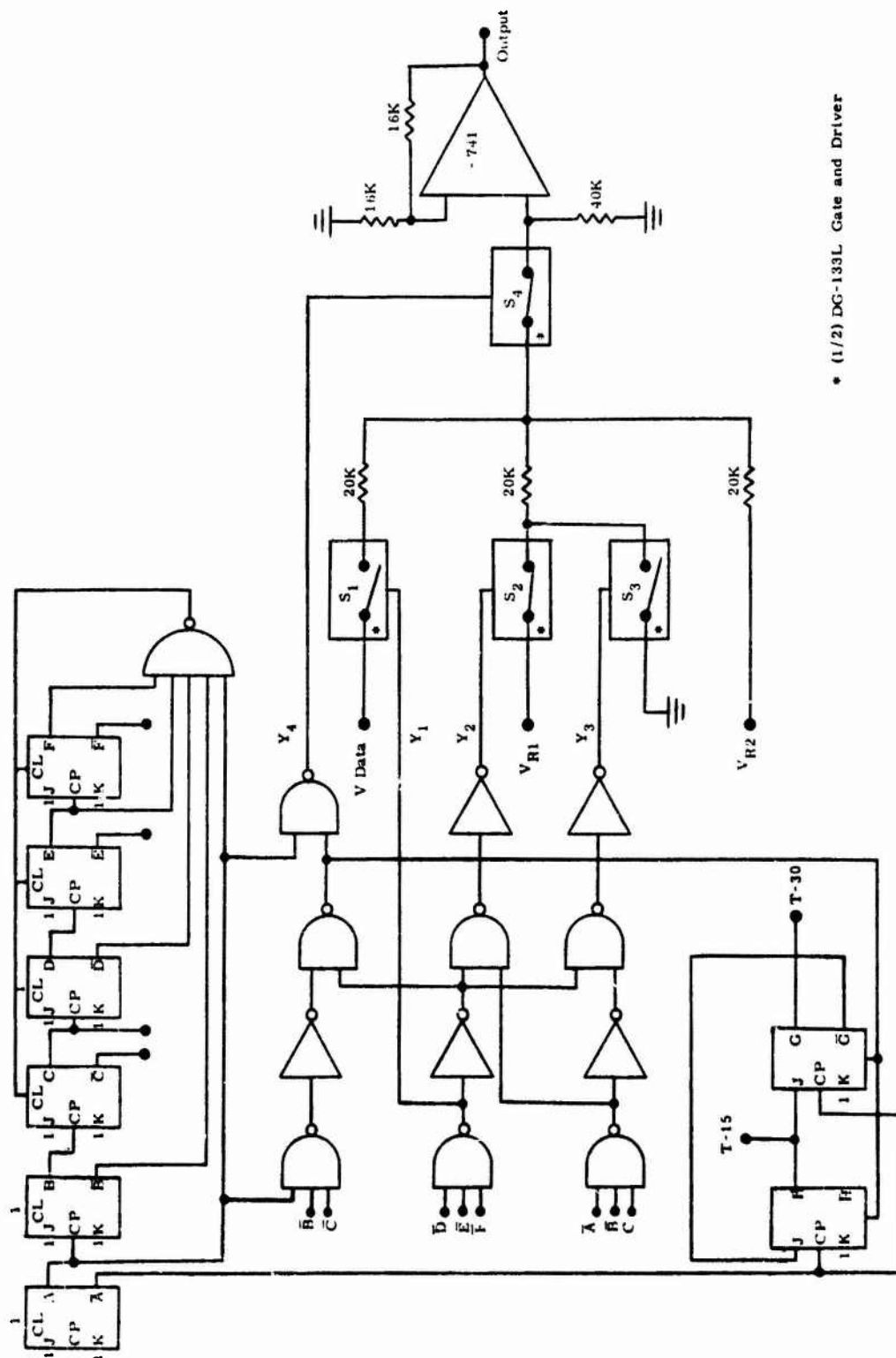


Fig. 28 LOGIC CLOCK



* (1/2) DG-133L Gate and Driver

Fig. 29 SIMULATED COMMUTATOR DIAGRAM

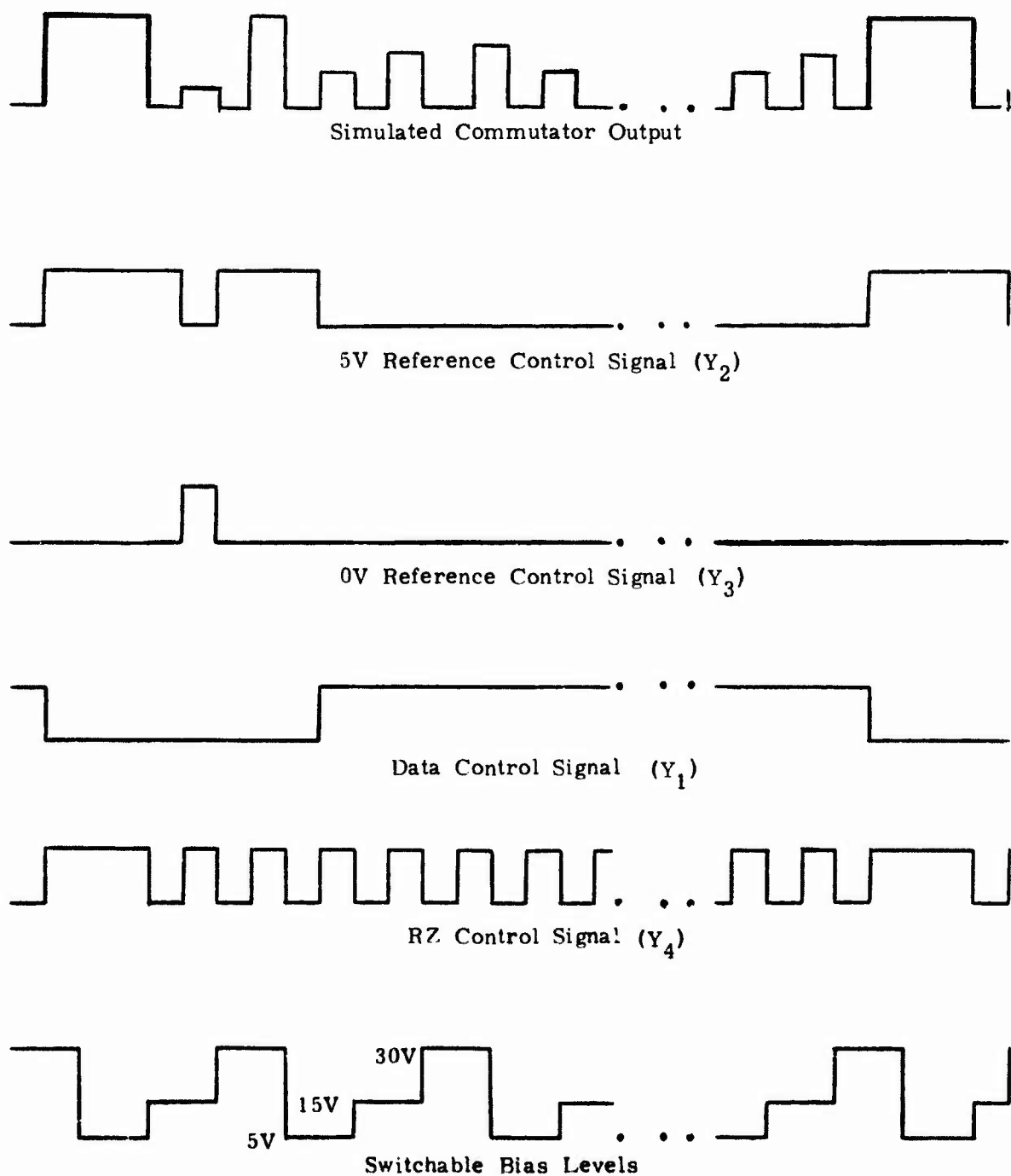


Fig. 30 SIMULATED COMMUTATOR WAVEFORMS

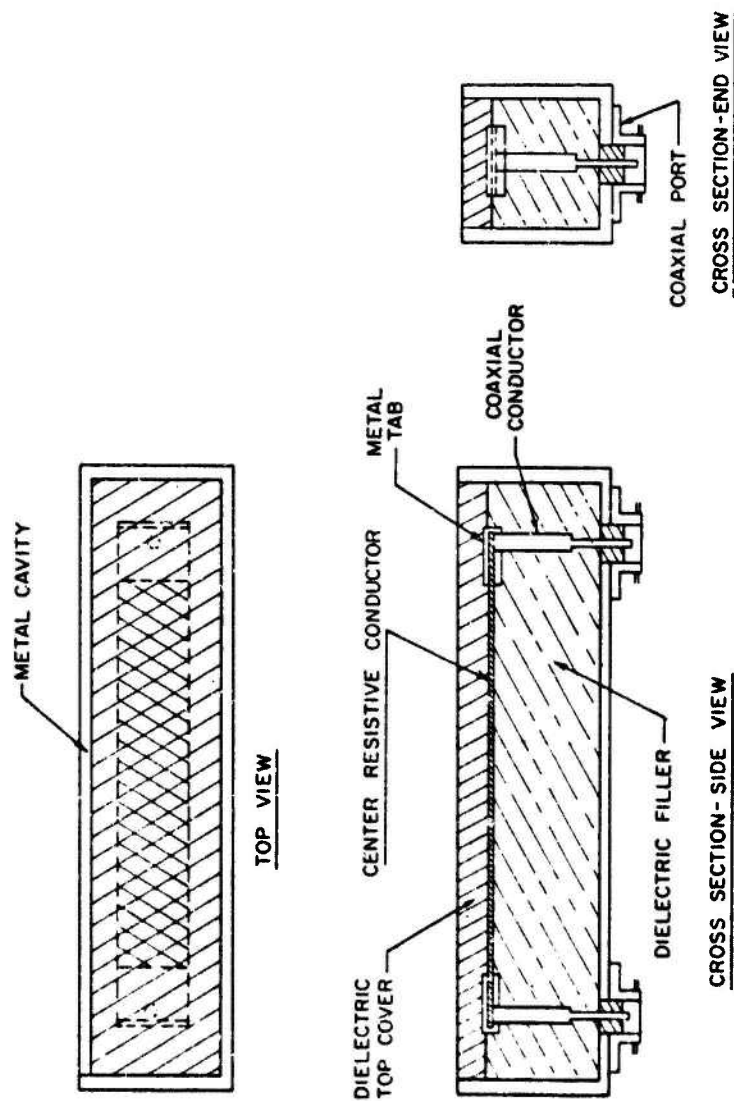


Fig. 31 STRIPLINE PROBE

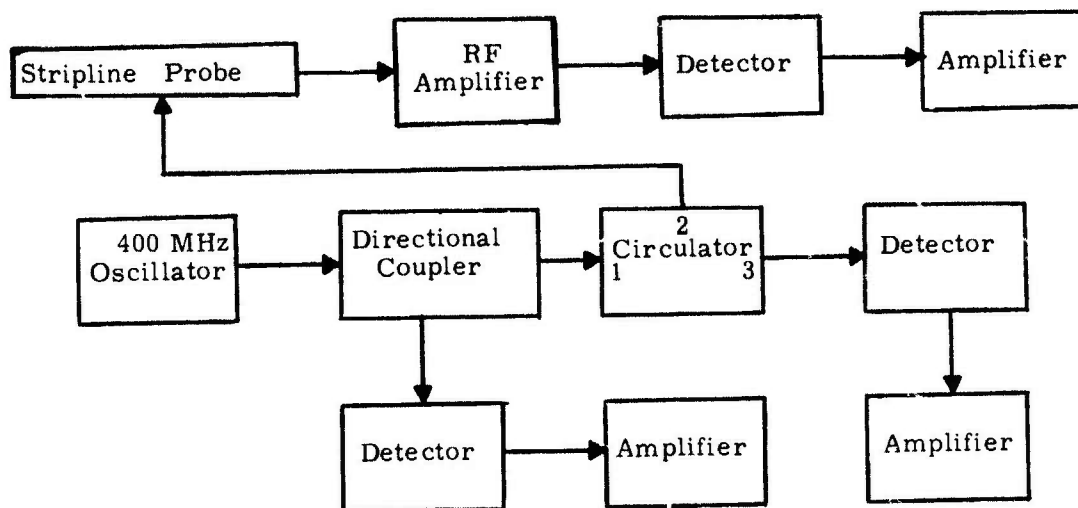


Fig. 32 STRIPLINE BLOCK DIAGRAM

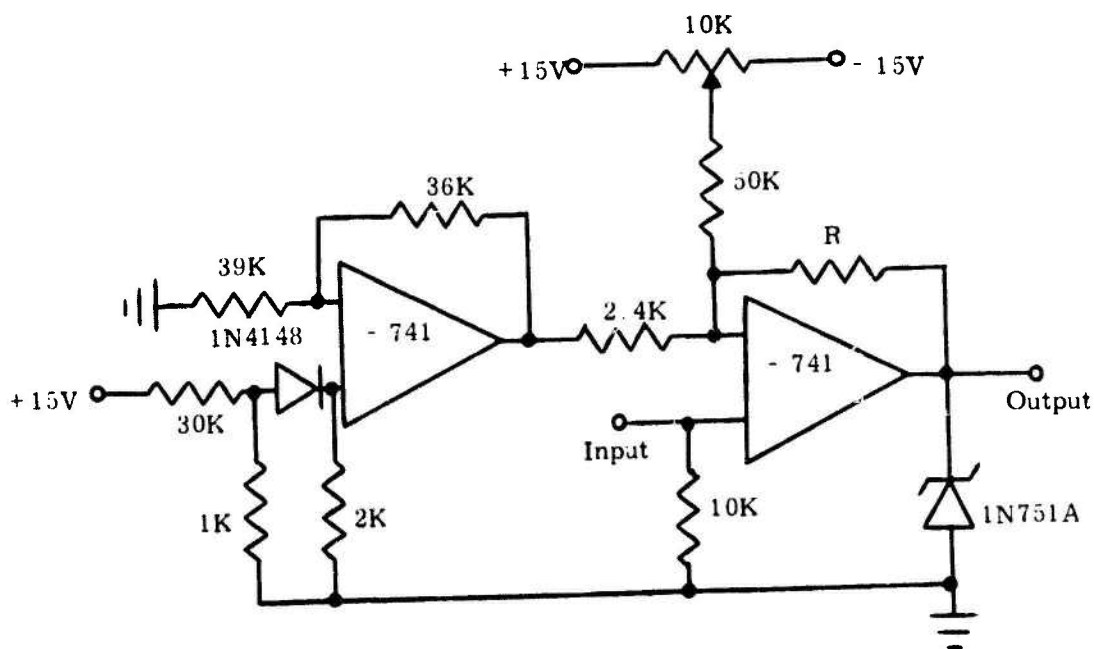


Fig. 33 STRIPLINE SIGNAL AMPLIFIER

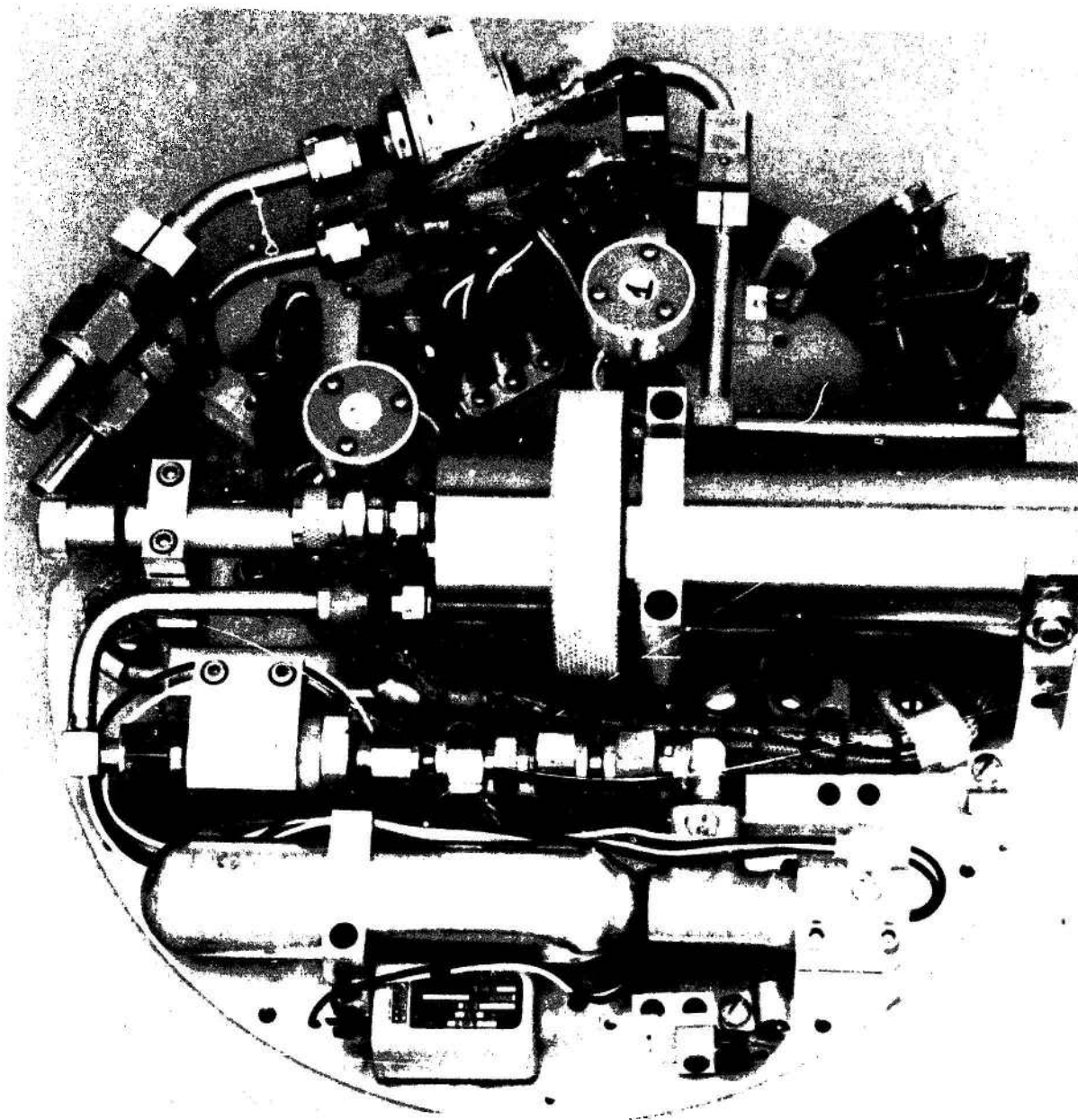


Fig. 34 CHEMICAL INJECTION DECK

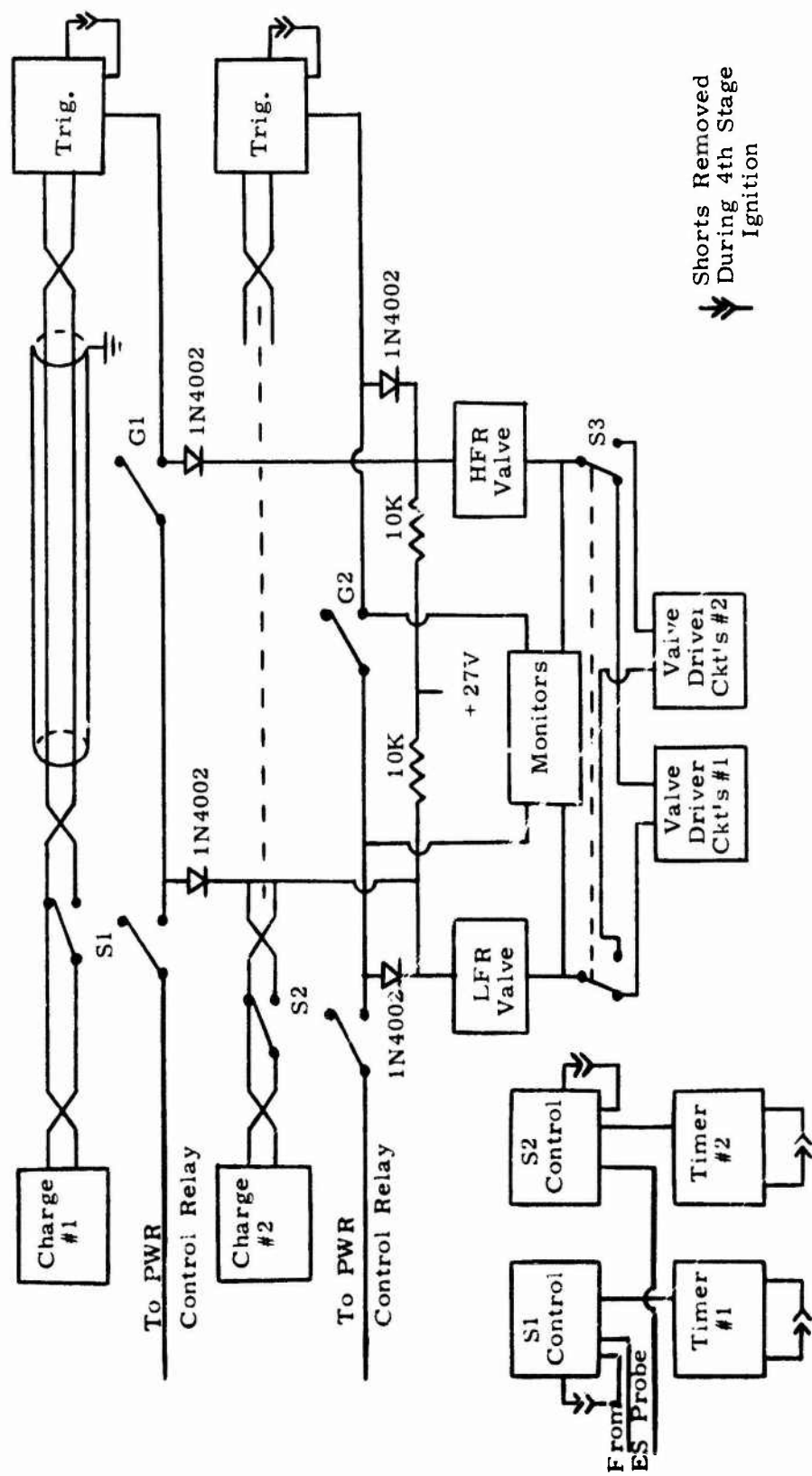


Fig. 35 INJECTION CONTROL GENERAL DIAGRAM

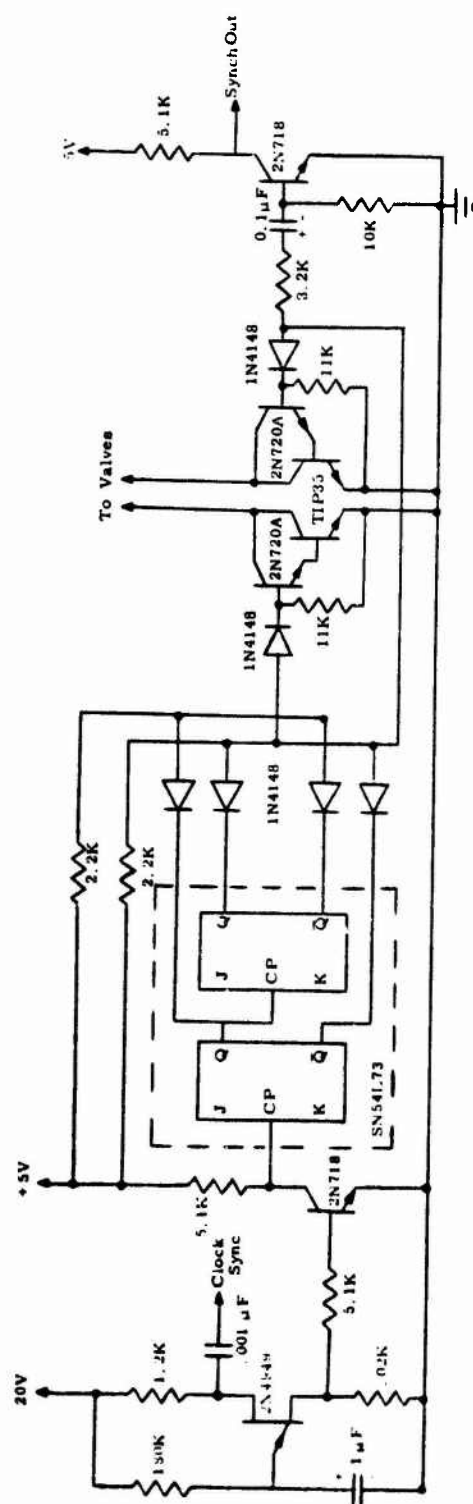


Fig. 36 VALVE CONTROL CIRCUIT

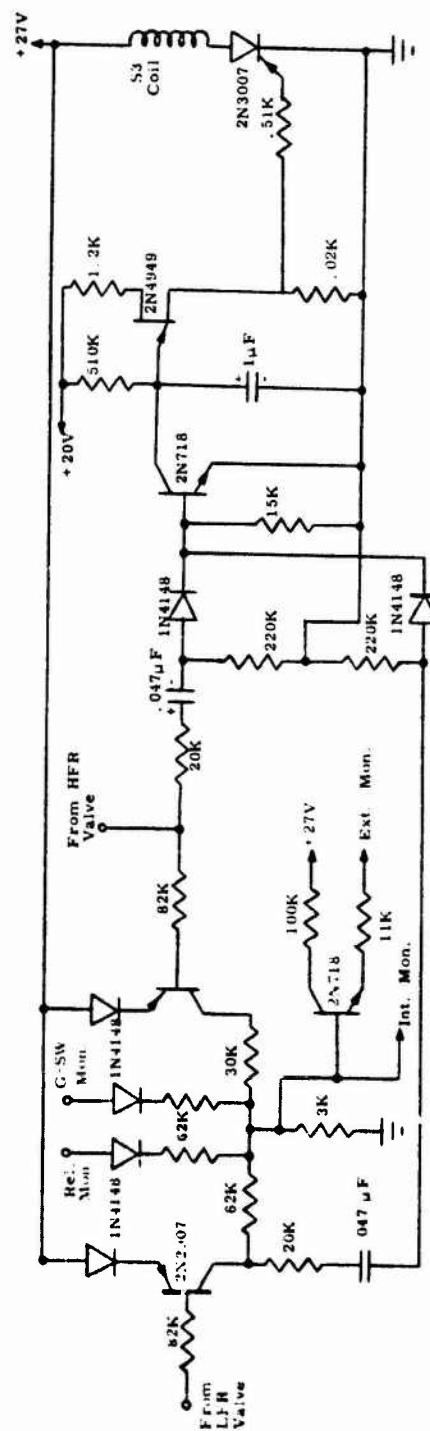


Fig. 37 MONITOR AND FAULT DETECTOR

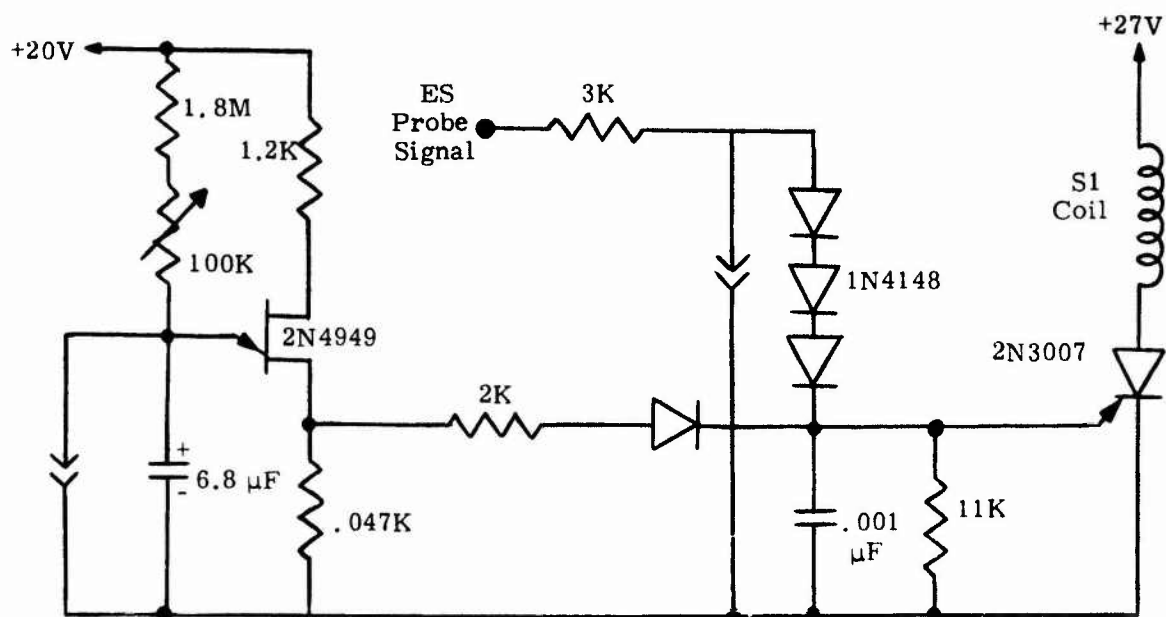


Fig. 38 TIMING AND S1 CONTROL CIRCUIT

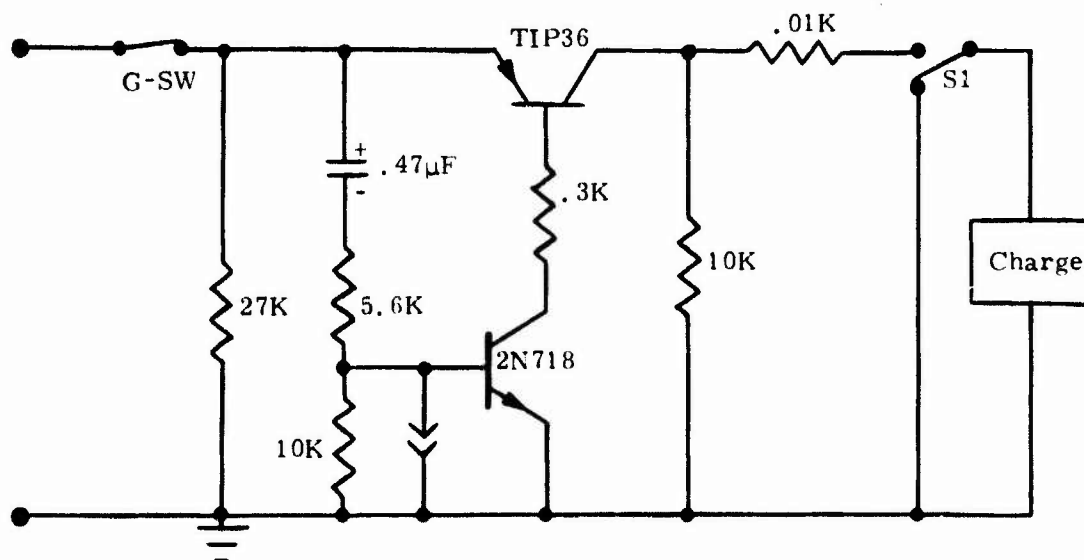


Fig. 39 EXPLOSIVE VALVE TRIGGER CIRCUIT

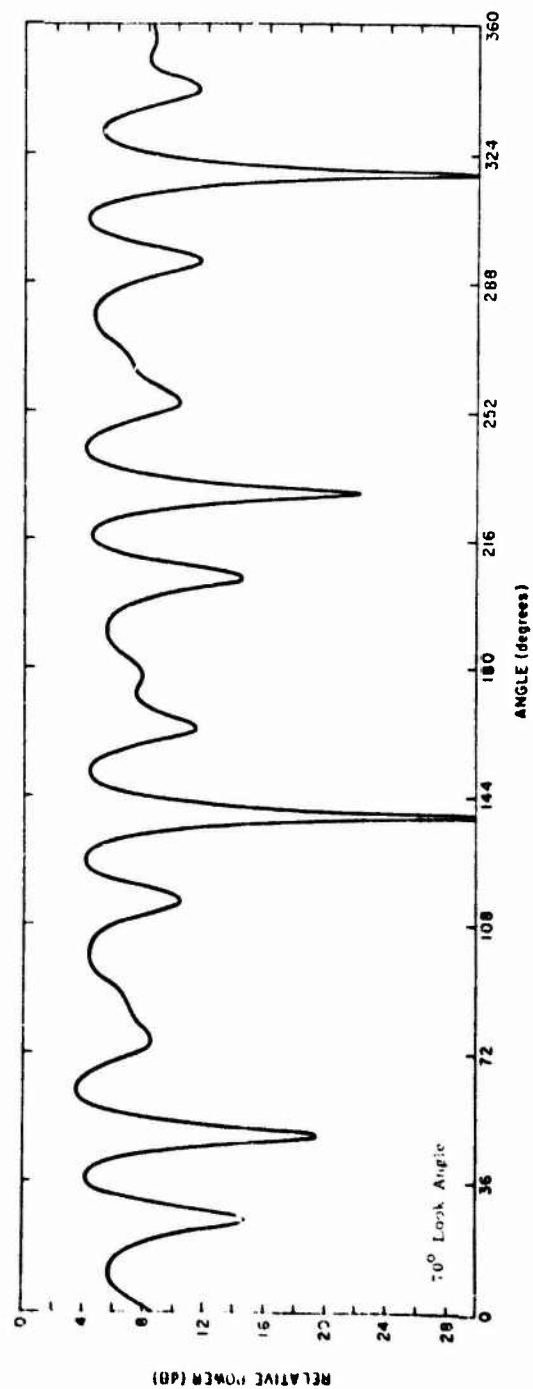
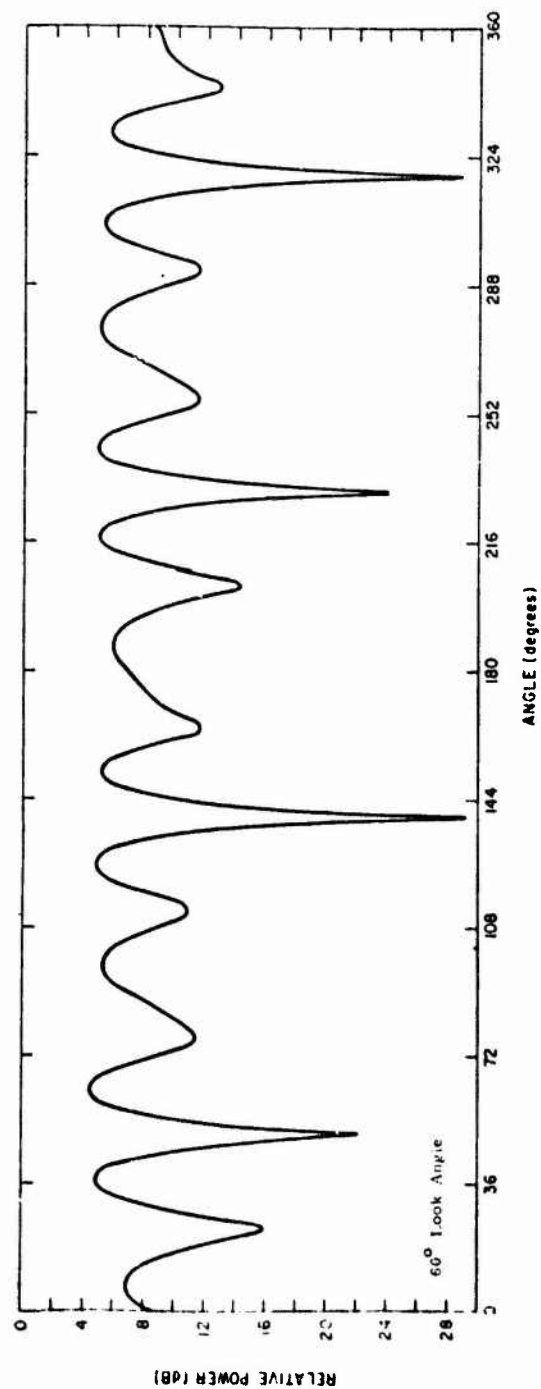


Fig. 40 TELEMETRY ANTENNA PATTERNS

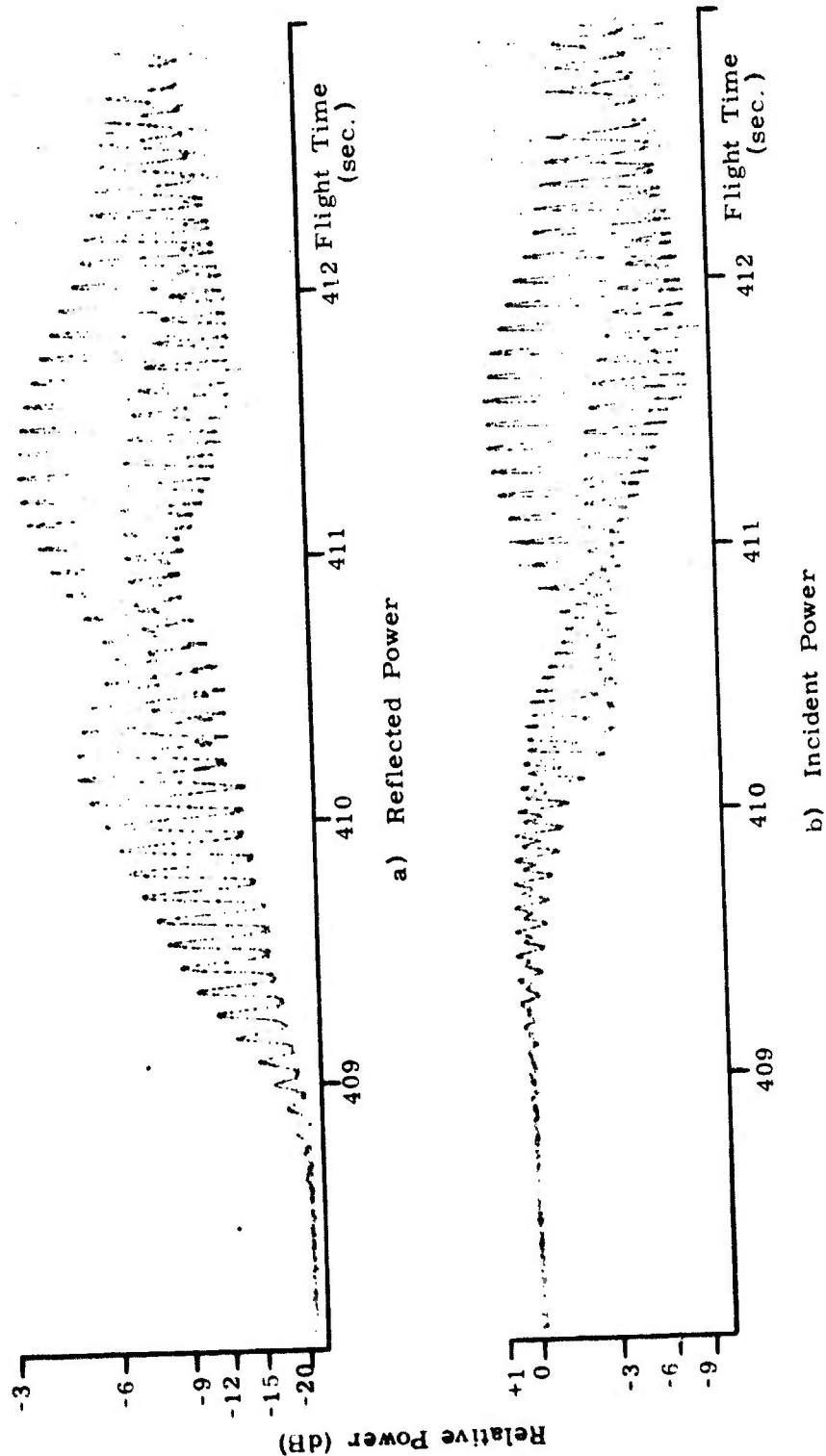


Fig. 41 TM REFLECTOMETER DATA. /D21.862

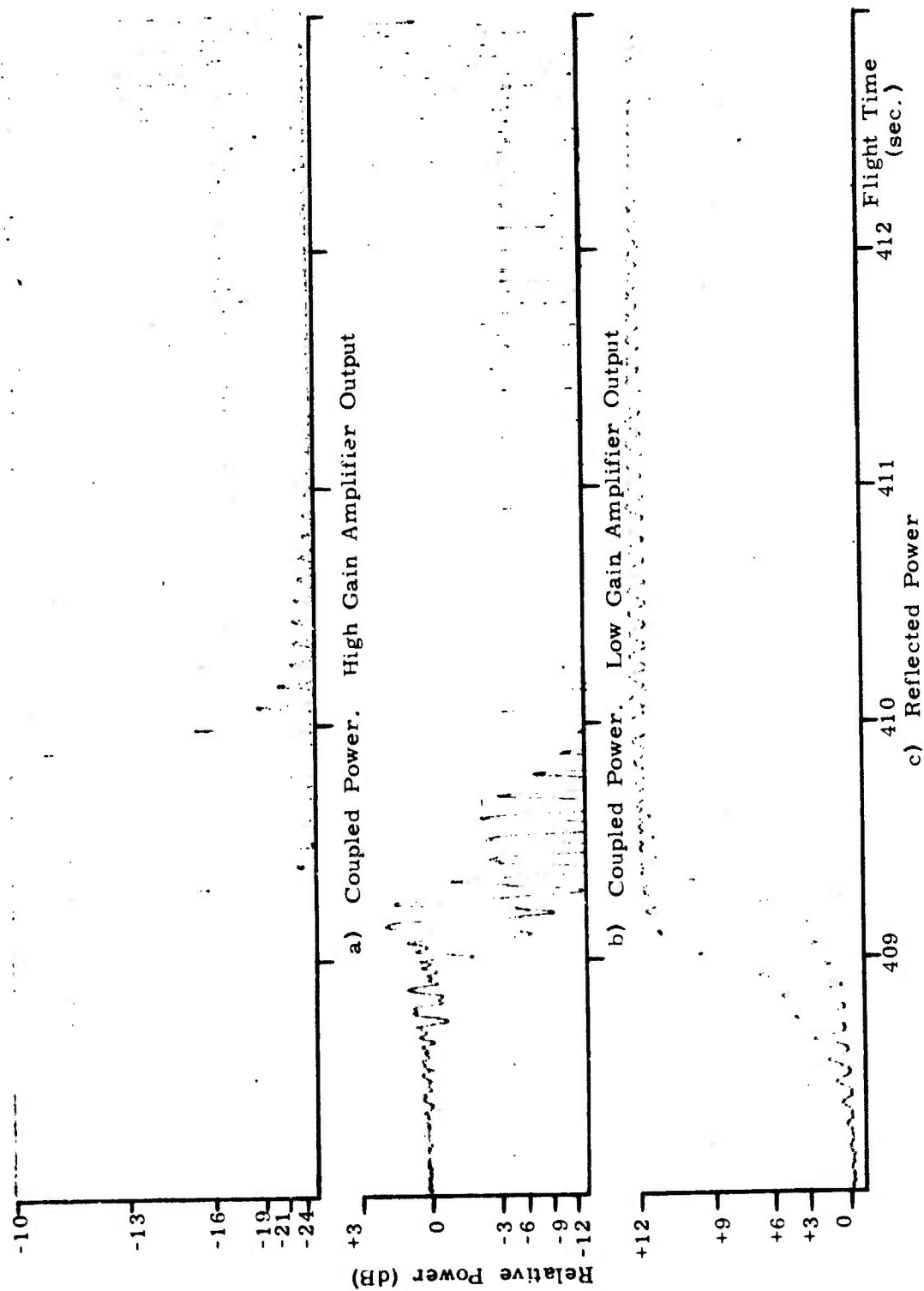


Fig. 42 TEST SIGNAL DATA. AD21.862

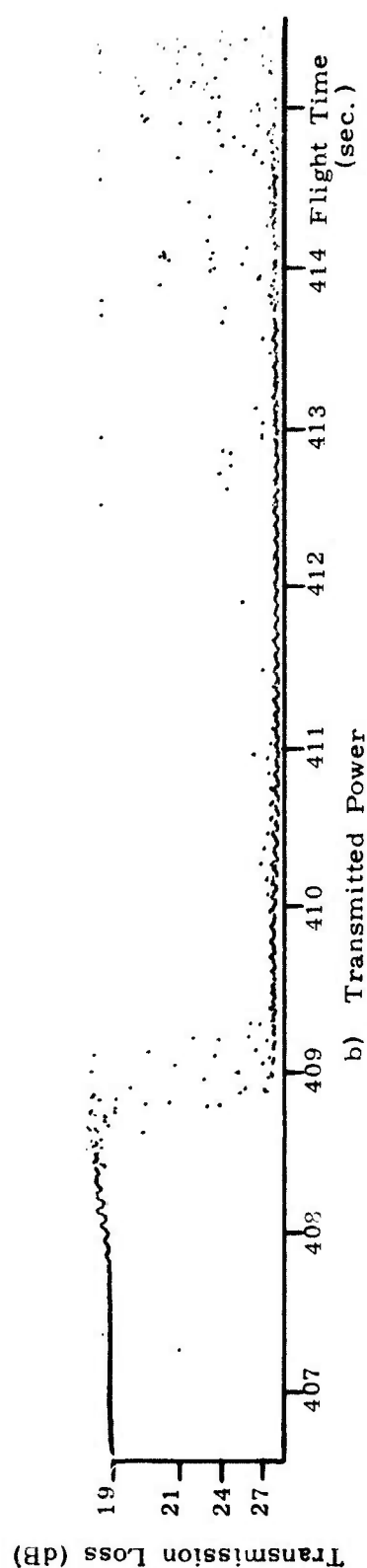
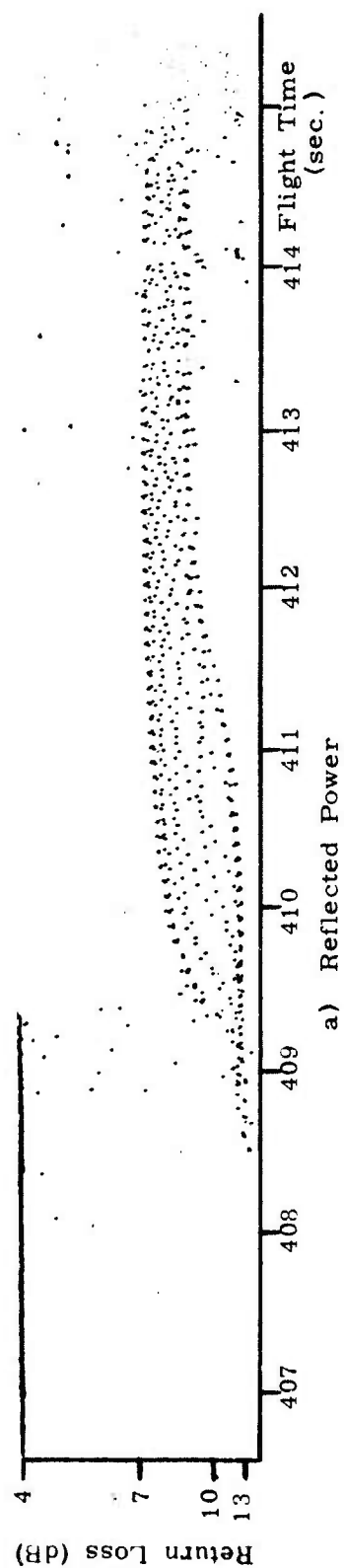


Fig. 43 STRIPLINE DATA

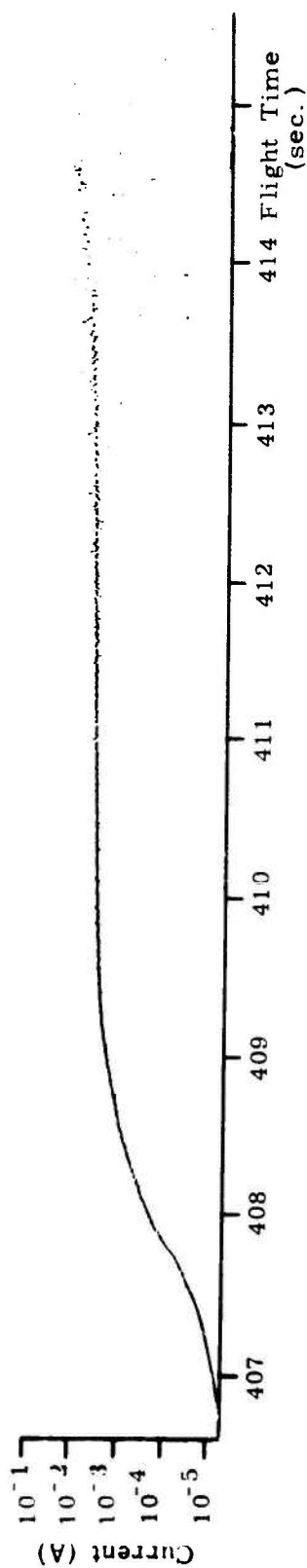


Fig. 44 ELECTROSTATIC PROBE DATA S/R - 0. AD21.862

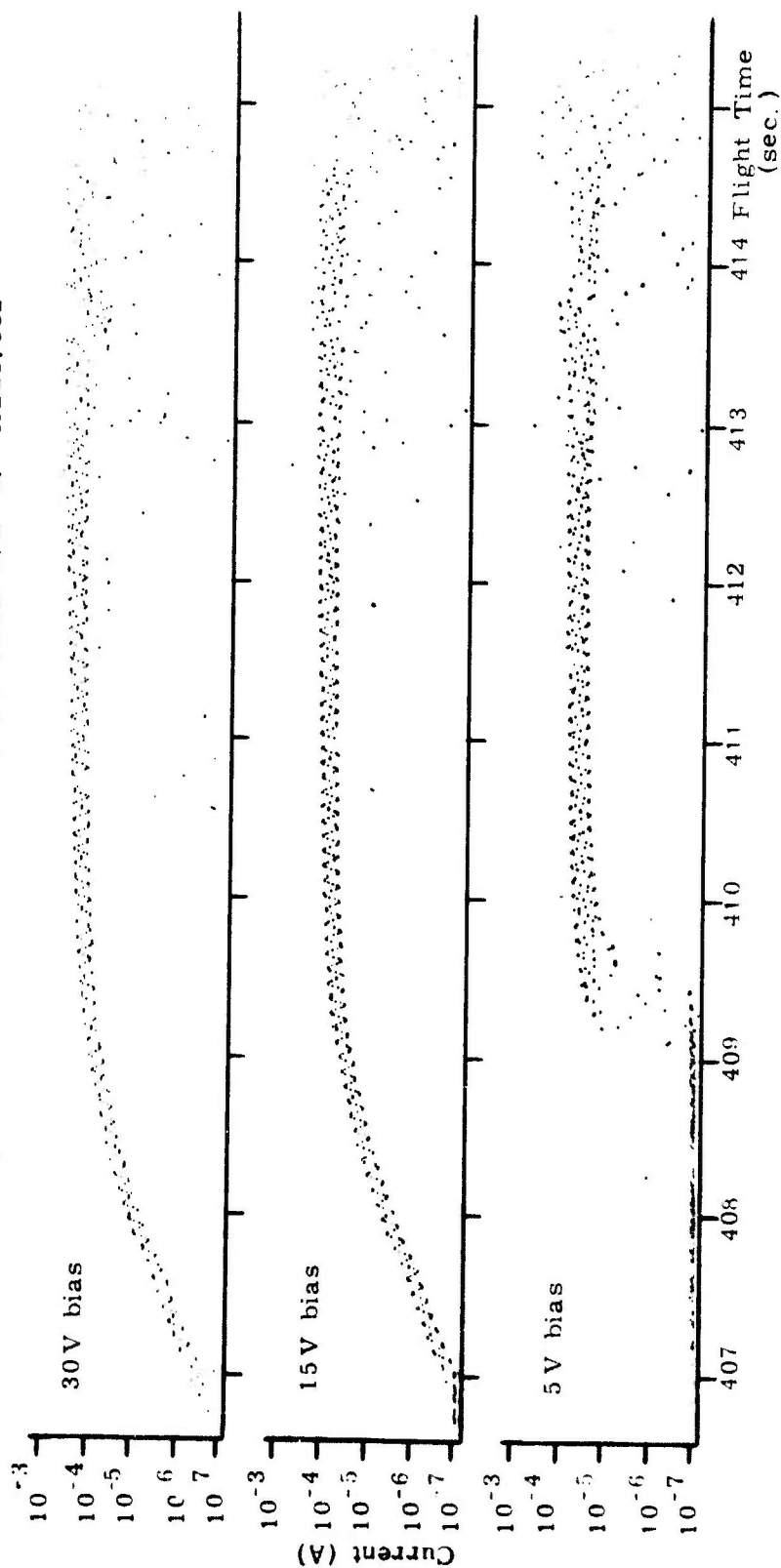


Fig. 45 ELECTROSTATIC PROBE DATA S/R - 0, $\alpha = 57.0^\circ$. AD21.862

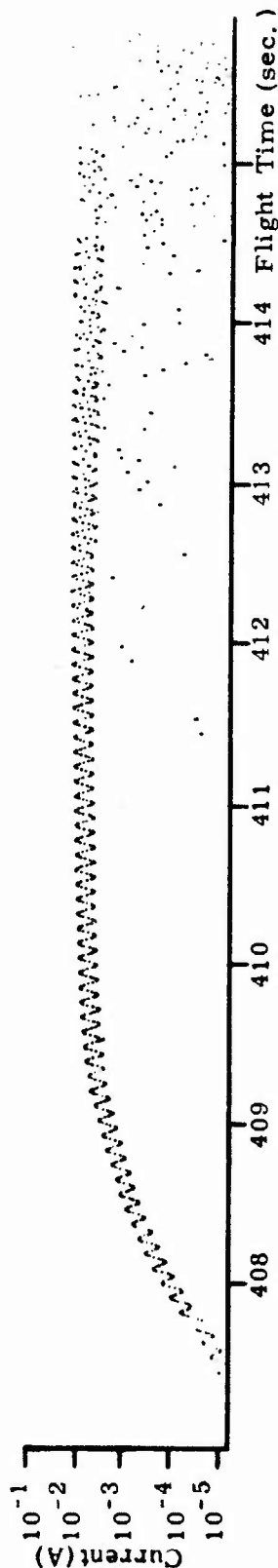


Fig. 46 ELECTROSTATIC PROBE DATA S/R = 2.58, $\theta = 48.0^\circ$, AD21.862

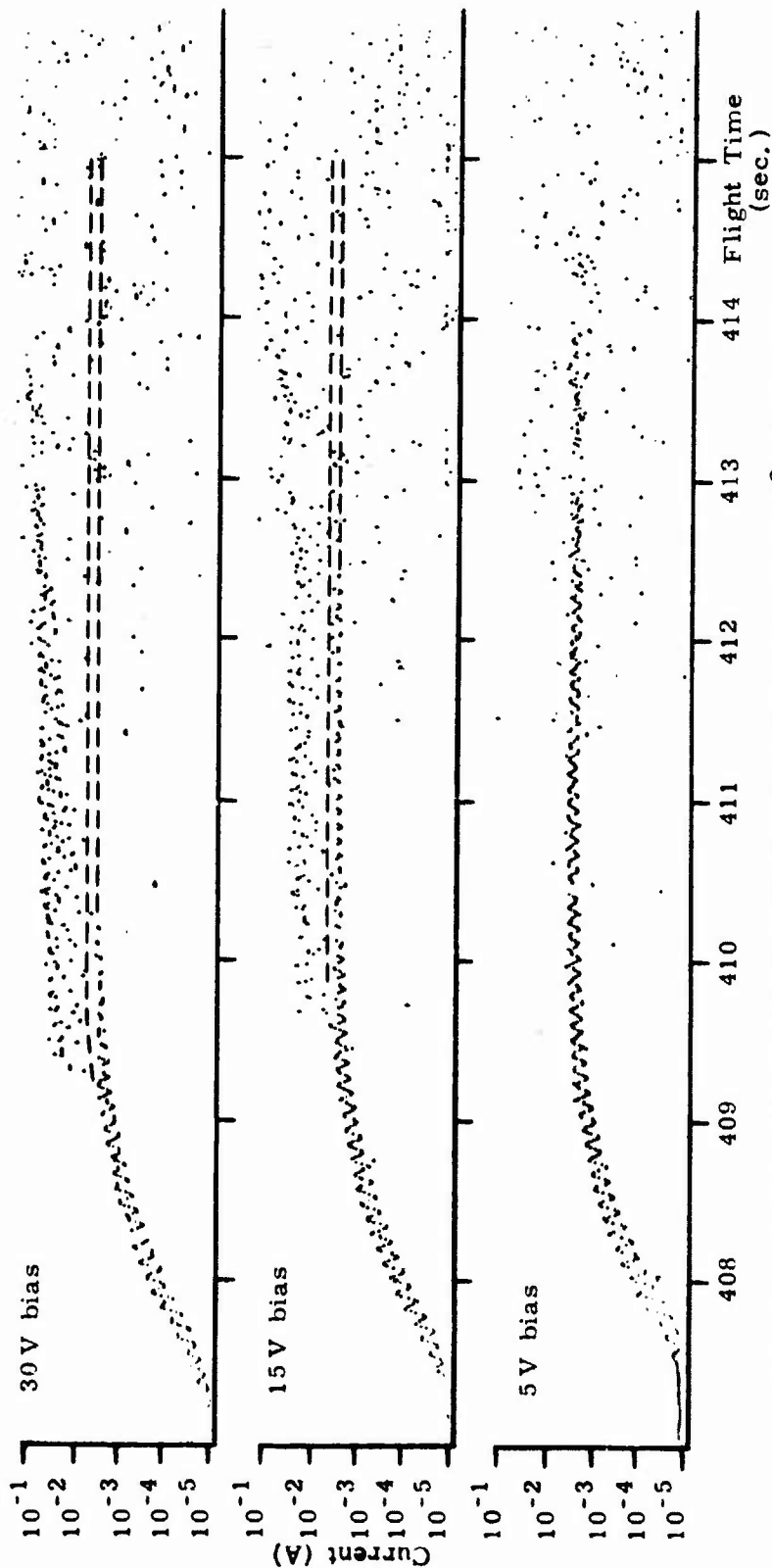


Fig. 47 ELECTROSTATIC PROBE DATA S/R = .475, $\theta = 52.5^\circ$, AD21.862

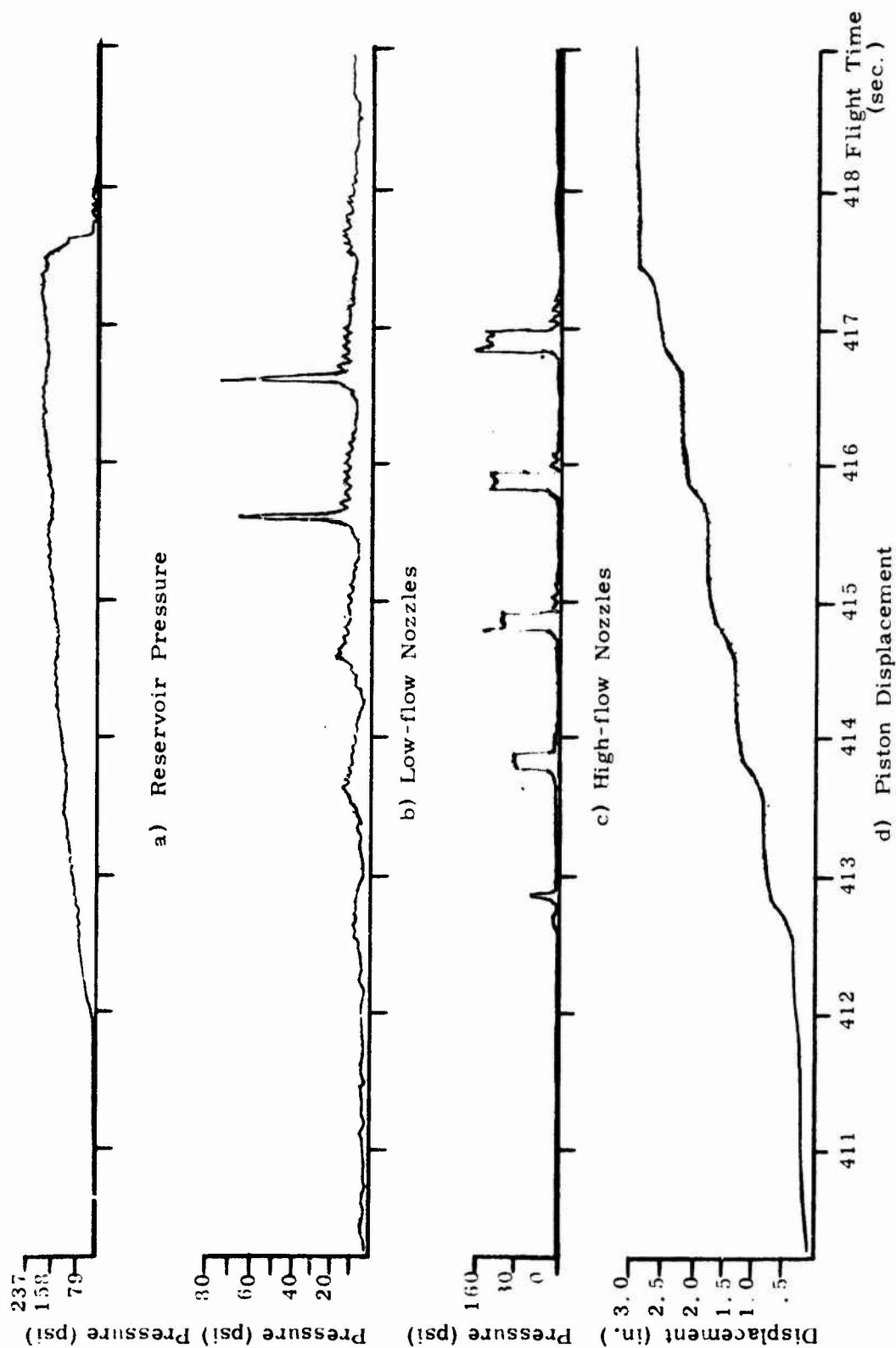


Fig. 48 INJECTION PRESSURE AND PISTON MOTION

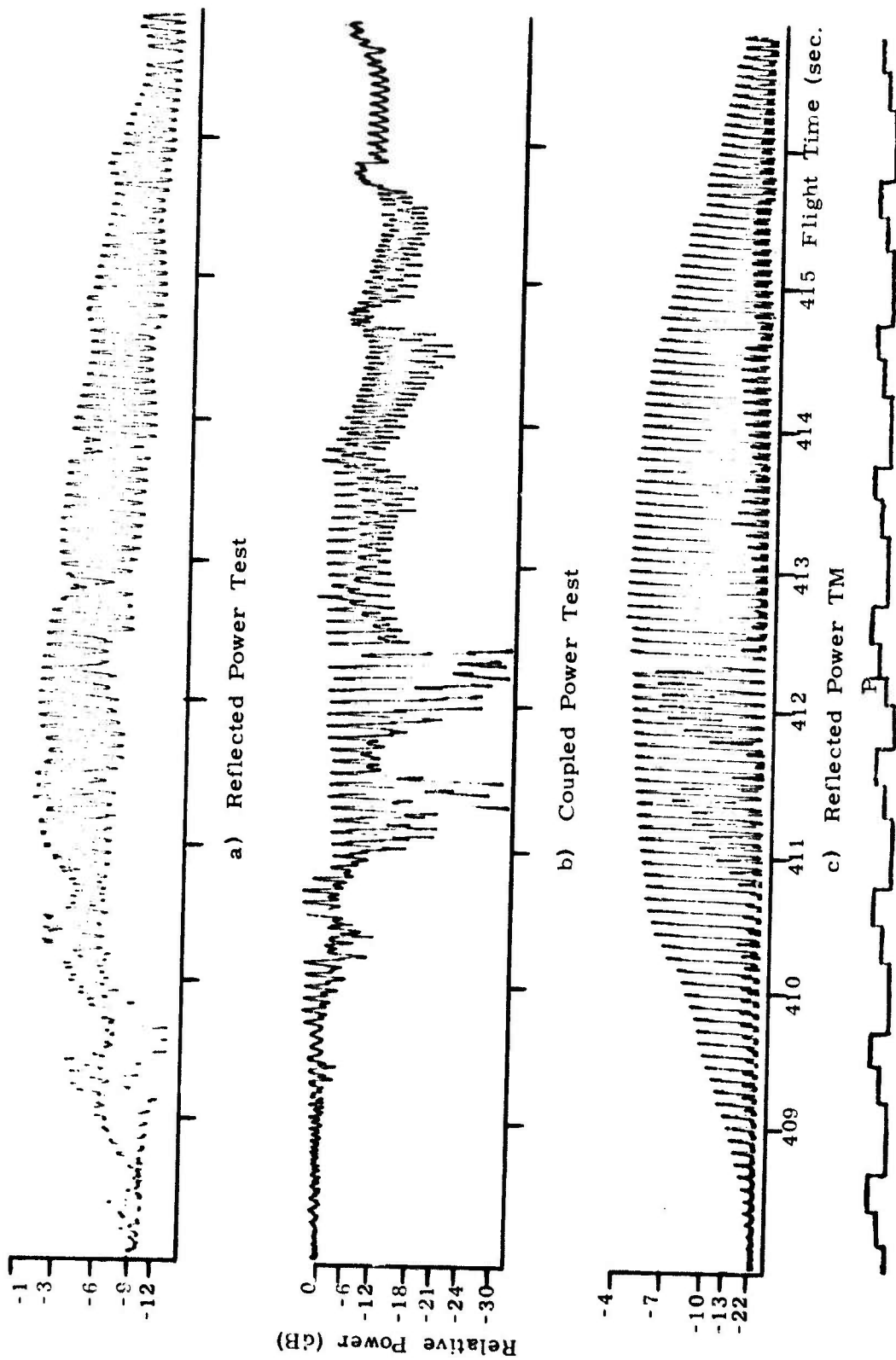


Fig. 49 TEST AND TM SIGNAL DATA. A21.011-1

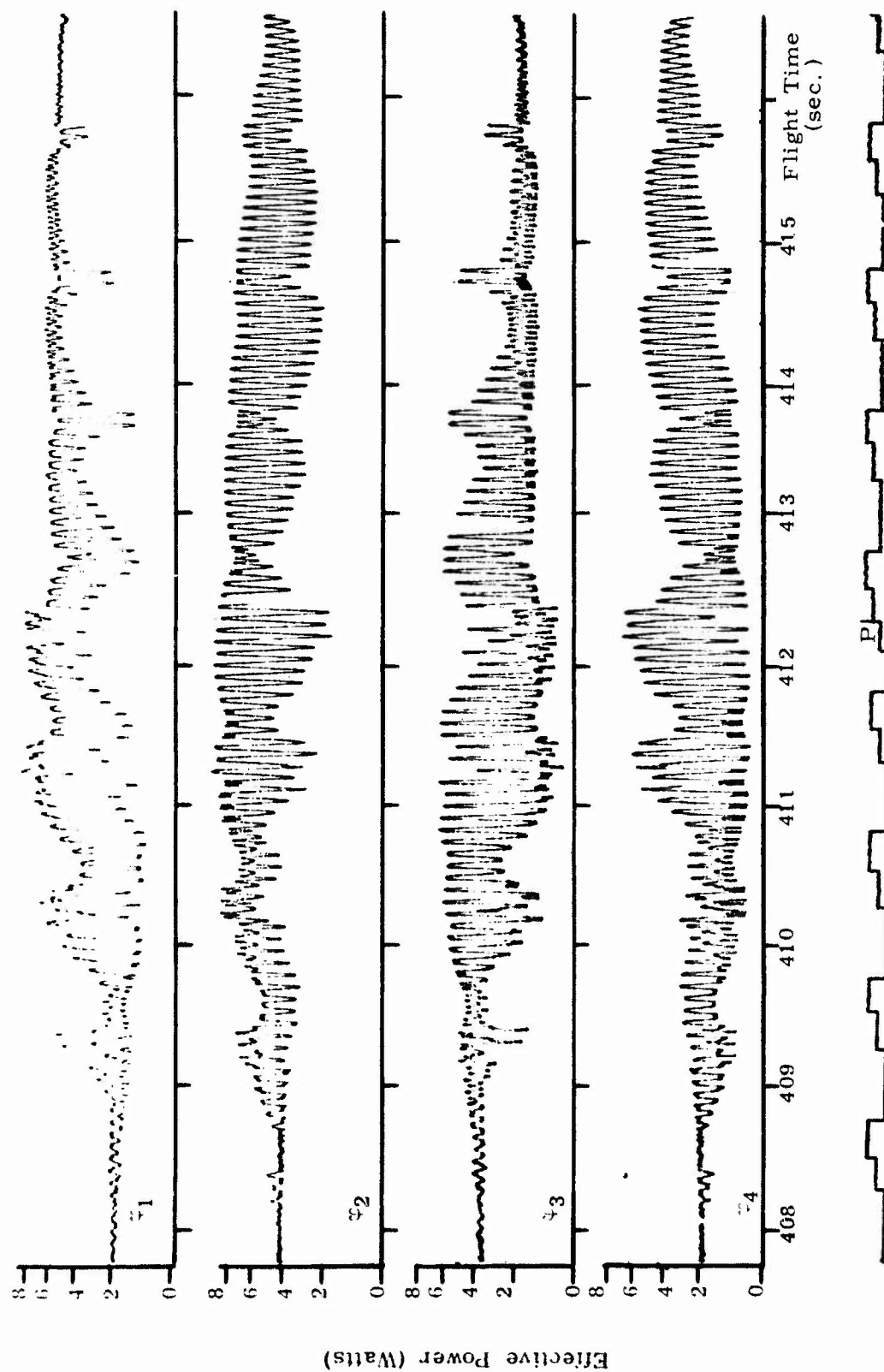


Fig. 50 FOUR PROBE FIELD METER DATA

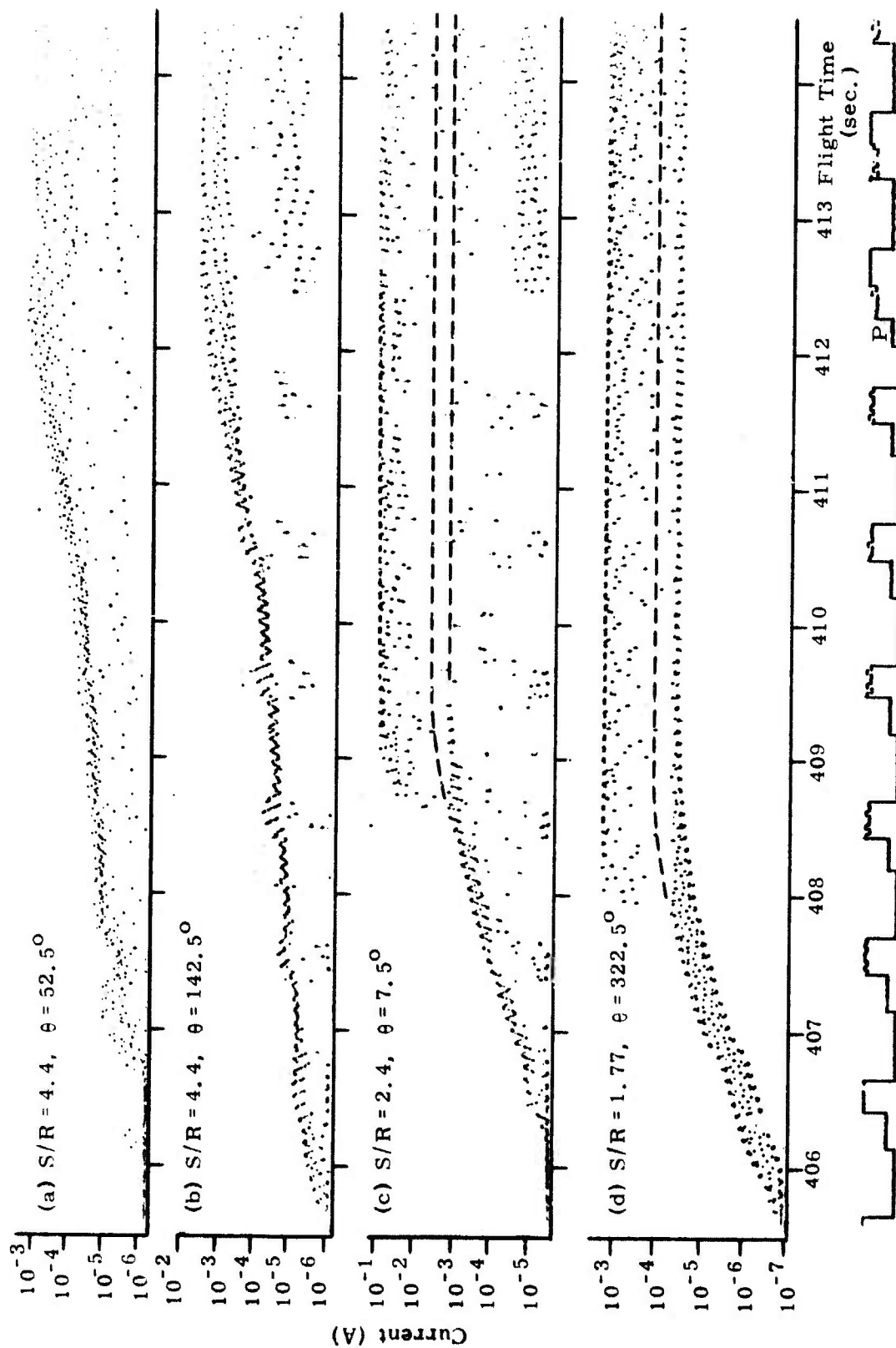


Fig. 51 ELECTROSTATIC PROBES - FIXED BIAS DATA. A21.011-1

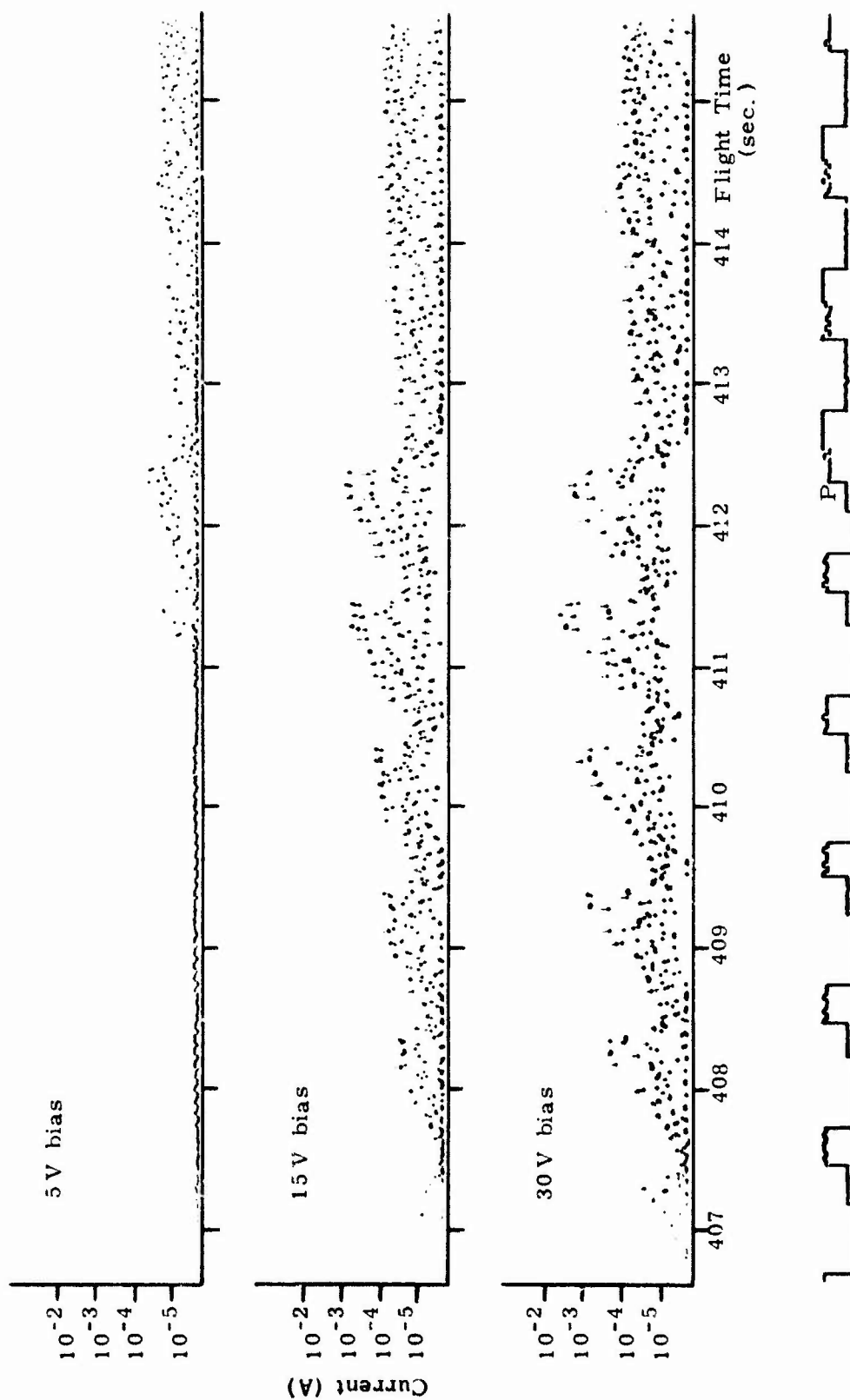


Fig. 52 ELECTROSTATIC PROBE DATA S/R = 2.4, $\theta = 48.0^\circ$. A21.011-1

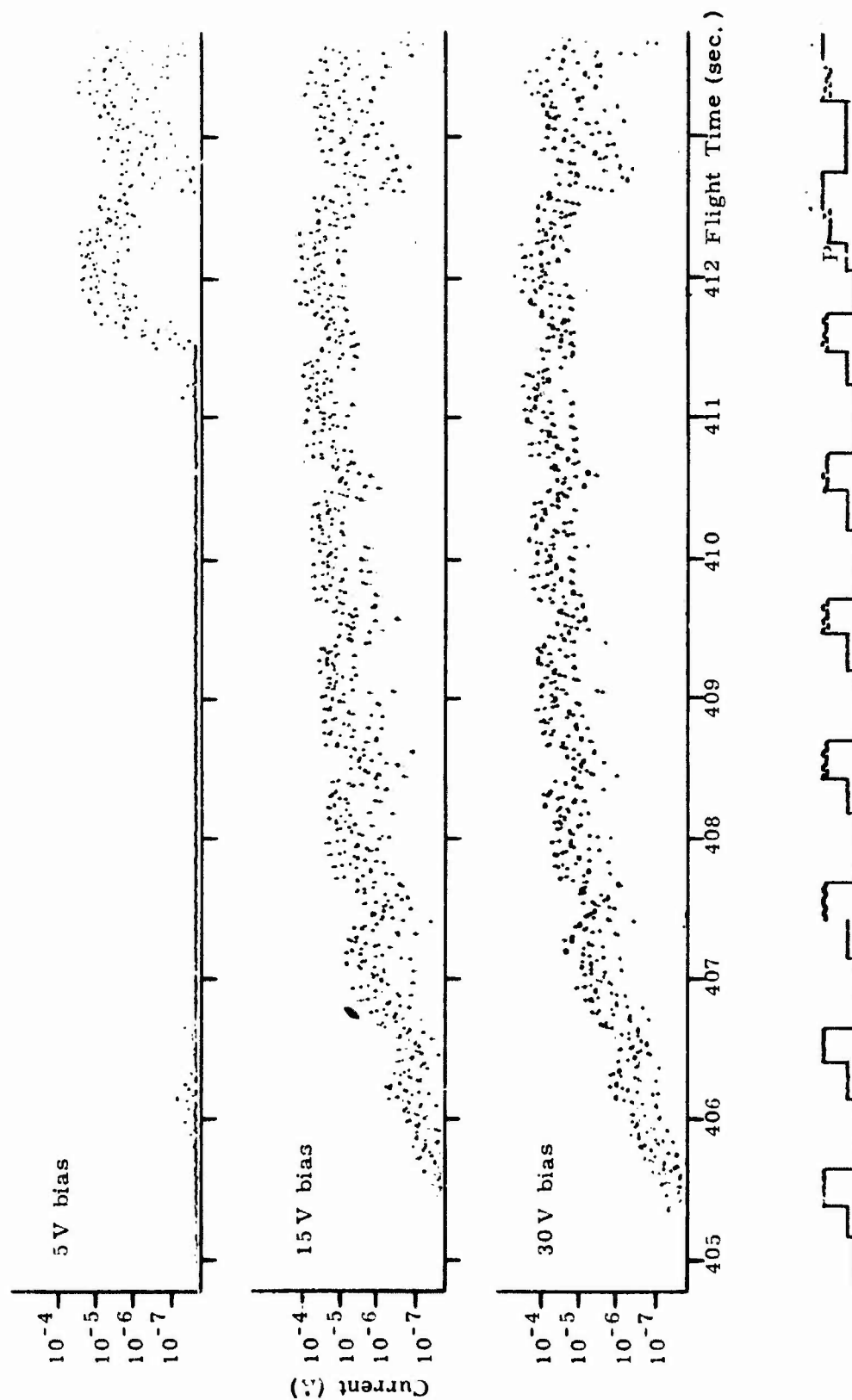


Fig. 53 ELECTROSTATIC PROBE DATA $S/R = 2.4$, $\theta = 57.0^\circ$, A21.011-1

Unclassified

Security Classification

DOCUMENT CONTROL DATA - R & D		
Security classification of title, body of abstract and indexing annotation must be entered when the overall report is classified		
1. ORIGINATING ACTIVITY (Corporate author) Northeastern University Boston, Massachusetts 02115		2a. REPORT SECURITY CLASSIFICATION Unclassified
		2b. GROUP
3. REPORT TITLE INSTRUMENTATION AND FLIGHT RESULTS OF REENTRY PLASMA DIAGNOSTIC AND ALLEVIATION EXPERIMENTS ON TRAILBLAZER II ROCKETS		
4. DESCRIPTIVE NOTES (Type of report and inclusive dates) Scientific Final. 1 March 1965 through 31 August 1972 12 December 72		Approved
5. AUTHOR(S) (First name, middle initial, last name) J. Spencer Rochefort Raimundas Sukys Ronald Symmes		
6. REPORT DATE 31 October 1972	7a. TOTAL NO. OF PAGES 84	7b. NO. OF REFS 20
8a. CONTRACT OR GRANT NO. F19628-69-C-0150		9a. ORIGINATOR'S REPORT NUMBER(S)
b. PROJECT NO., Task, Work Unit Nos. 4642-01-01		
c. DoD Element: 62101F		9b. OTHER REPORT NO(S) (Any other numbers that may be assigned this report)
d. DoD Subelement: 684642		AFCRL-72-0695
10. DISTRIBUTION STATEMENT B-Distribution limited to U.S. Government agencies only; Test and Evaluation, 30 November 1972. Other requests for this document must be referred to AFCRL (LZP), L.G. Hanscom Field, Bedford, Massachusetts 01730.		
11. SUPPLEMENTARY NOTES TECH, OTHER		12. SPONSORING MILITARY ACTIVITY Air Force Cambridge Research Laboratories (LZ), L. G. Hanscom Field Bedford, Massachusetts 01730
13. ABSTRACT Two Trailblazer II rockets were launched on 24 November 1970 and 28 July 1972 from NASA rocket test facility at Wallops Island, Virginia, to study the properties of the shock-ionized flow field and its effects on microwave radiation. Description of the apparatus carried by the two vehicles is presented in this report. The instrumentation to measure the flow field during reentry included such diagnostic sensors as electrostatic probes, stripline probe and a conductivity probe. S-band microwave systems were employed to determine plasma effects on antennas. The measurements included phase and magnitude of the reflection coefficient, variations in mutual coupling between two on board antennas and transmitted signal attenuation. A pulsed liquid injection apparatus was used to perform a plasma alleviation experiment. Performance of the instrumentation and general results obtained from unprocessed data are discussed.		

DD FORM 1473 (PAGE 1)

1 NOV 65

Unclassified

Security Classification

Unclassified
Security Classification

14. KEY WORDS	LINK A		LINK B		LINK C	
	ROLE	WT	ROLE	WT	ROLE	WT
Reentry Communications Plasma Diagnostics Electrostatic Probes Microwave Reflectometer Stripline Probe						